

PREPARATION OF PLZT THIN FILMS BY CHEMICAL SOLUTION
DEPOSITION AND THEIR CHARACTERIZATION

A THESIS SUBMITTED TO
THE GRADUATE SCHOOL OF NATURAL AND APPLIED SCIENCES
OF
MIDDLE EAST TECHNICAL UNIVERSITY

BY

BURKAN KAPLAN

IN PARTIAL FULFILLMENT OF THE REQUIREMENTS
FOR
THE DEGREE OF MASTER OF SCIENCE
IN
METALLURGICAL AND MATERIALS ENGINEERING

NOVEMBER 2005

Approval of the Graduate School of Natural and Applied Sciences

Prof. Dr. Canan ÖZGEN
Director

I certify that this thesis satisfies all the requirements as a thesis for the degree of Master of Science.

Prof. Dr. Tayfur ÖZTÜRK
Head of Department

This is to certify that we have read this thesis and that in our opinion it is fully adequate, in scope and quality, as a thesis for the degree of Master of Science.

Prof. Dr. Macit ÖZENBAŞ
Supervisor

Examining Committee Members

Prof. Dr. Muharrem TİMUÇİN	(METU,METE)	_____
Prof. Dr. Macit ÖZENBAŞ	(METU,METE)	_____
Prof. Dr. Mehmet PARLAK	(METU, PHYS)	_____
Asst. Prof. Dr. Caner DURUCAN	(METU,METE)	_____
Asst. Prof. Dr. Arcan DERİCİOĞLU	(METU,METE)	_____

I hereby declare that all information in this document has been obtained and presented in accordance with academic rules and ethical conduct. I also declare that, as required by these rules and conduct, I have fully cited and referenced all material and results that are not original to this work.

Name, Last name :

Signature :

ABSTRACT

PREPARATION OF PLZT THIN FILMS BY CHEMICAL SOLUTION DEPOSITION AND THEIR CHARACTERIZATION

Kaplan, Burkan

M.S., Department of Metallurgical and Materials Engineering

Supervisor: Prof. Dr. Macit Özenbaş

November 2005, 125 pages

In this study, La^{3+} was substituted into lead zirconate titanate (PZT) system by $\text{Pb}_{1-x}\text{La}_x(\text{Zr}_y\text{Ti}_{1-y})_{1-x/4}\text{O}_3$ nominal stoichiometry and it was processed via chemical solution deposition on (111)-Pt/Ti/SiO₂/Si-(100) substrate. PLZT solutions were prepared by mixing two solutions, one of which was obtained by dissolving lead acetate and lanthanum acetate hydrate in 2 methoxyethanol at high temperature. This solution was then mixed with the second solution containing zirconium propoxide and titanium isopropoxide. 40ml/0.4M solution was prepared and spin coated on Pt/Ti/SiO₂/Si substrates at 3000 rpm for 30 seconds. After 4 coating cycles, film thickness was reached to 600 nm.

A systematic study was carried out in different regions of PLZT phase diagram tetragonal, rhombohedral and on the morphotropic phase boundary (MPB) to obtain optimized results of ferroelectric, dielectric and optical properties of the material.

During the period of the work, effect of parameters on these properties such as heat treatment conditions, chemical composition of the film, microstructure and thickness of the film was investigated.

The films were characterized structurally and electrically. For structural properties, X-ray diffraction technique (XRD), energy dispersive spectrometry (EDS) and Scanning Electron Microscope (SEM) were used to observe phases and surface characterization. For electrical measurements, ferroelectric tester was used to obtain dielectric constant, loss tangent and hysteresis curves. Optical transmittance of the films was also investigated by UV-VIS Spectrophotometer and optical film constants were calculated by modified envelope method.

It was observed that the optimum heat treatment conditions were achieved at 750⁰C for 3 hours. The highest ferroelectric and dielectric properties such as remanent polarization and dielectric constant were obtained using that temperature.

The dielectric constant of the films was measured in the frequency range of 1kHz-1MHz and remained almost constant in this region. The change of dielectric constant and ferroelectric hysteresis loops were obtained as a function of Zr/Ti ratio and La content.

The grain size as a function of sintering temperature and La content was investigated. It was seen that as the sintering temperature was increased, the grain size of the films increased. The same tendency was also observed when the La content was increased.

Fatigue behavior of PLZT thin films was also investigated by Radiant Ferroelectric Tester at 50 kHz and $\pm 15V$. Change of remanent polarization (P_r) as a function of cumulative switching cycles (N) was drawn with the log scale of x-axis. Furthermore, leakage current characteristics of the films were also obtained by the ferroelectric tester at $\pm 15V$. It has been observed that as the La content of the film was increased, leakage current of the PLZT films decreased.

Keywords: PLZT, (111)-Pt/Ti/SiO₂/Si-(100) substrate, Chemical Solution Deposition.

ÖZ

PLZT İNCE FİLMLEİN KİMYASAL ÇÖZELTİDEN BİRİKTİRME YÖNTEMİYLE HAZIRLANIŞI VE KARAKTERİZASYONU

Kaplan, Burkan

M.S., Metalurji ve Malzeme Mühendisliği Bölümü

Tez Yöneticisi: Prof. Dr. Macit Özenbaş

Kasım, 2005, 125 sayfa

Bu çalışmada, La elementi $Pb_{1-x}La_x(Zr_yTi_{1-y})_{1-x/4}O_3$ kimyasal formülü göz önünde tutularak kurşun zirkonat titanat (PZT) sistemi içine ilave edilmiş ve kimyasal çözeltiden biriktirme yöntemiyle ve (111)-Pt/Ti/SiO₂/Si-(100) altlıklar üzerine kaplanmışlardır. PLZT çözeltileri iki ayrı çözeltinin karıştırılmasıyla hazırlanmışlardır ve bunlardan ilki kurşun asetat ile lantan asetat hidrat'ın 2 metoksi etanol içinde yüksek sıcaklıkta çözündürülmesiyle elde edilmiştir. Bu çözelti daha sonra içinde zirkonyum propoksit ve titanyum izopropoksit bulunduran ikinci çözelti ile karıştırılmıştır. 0.4M/40ml olarak hazırlanan çözelti Pt/Ti/SiO₂/Si altlıklar üzerine dakikada 3000 devirde 30 saniye süreyle kaplanmışlardır. 4 kaplama döngüsü sonucunda 600 nm kalınlığa ulaşılmıştır.

Ferroelektrik, dielektrik ve optik özellikleri optimize etmede sistematik bir yaklaşım benimsenmiş olup PLZT faz diyagramının tetragonal, rombohedral alanları ile morfotropik faz sınırı kompozisyonunda olmak üzere üç farklı bölgesinde çalışılmıştır.

Bu çalışma süresince ısıtım işlem koşulları, filmlerin kimyasal kompozisyonları, filmlerin içyapısı ve kalınlıkları gibi parametrelerin ferroelektrik ve dielektrik özelliklere olan etkisi incelenmiştir.

İnce filmler yapısal ve elektriksel olarak incelenmişlerdir. Yapısal özellikler için, X-ışınları tekniği (XRD), Enerji Dispersiv Analiz Ünitesi (EDS) ve Tarama Elektron Mikroskopu (SEM) faz ve yüzey karakterizasyonunda kullanılmışlardır. Dielektrik sabiti, kayıpları ve ferroelektrik polarizasyon döngüsü ferroelektrik test cihazı tarafından ölçülmüştür. Filmlerin optik geçirgenliği UV-VIS Spektrofotometre yardımıyla incelenmiş ve modifiye edilmiş zarf metodu ile optik film sabitleri hesaplanmıştır.

Optimum ısıtım işlem koşullarına 750 °C de 3 saat sinterlenerek ulaşılmıştır. En yüksek dielektrik sabiti (K) ve kalıcı polarizasyon (P_r) değeri bu ısıtım işlem sıcaklığı kullanılarak elde edilmiştir.

Filmlerin dielektrik sabitleri 1kHz ile 1MHz frekans aralığında ölçülmüştür ve bu aralıkta ölçülen değerler hemen hemen sabit kalmıştır. Dielektrik sabiti değerleri ve ferroelektrik polarizasyon döngüleri Zr/Ti oranına ve La miktarına bağlı olarak elde edilmişlerdir.

Tane büyüklüğü sinterleme sıcaklığına ve La miktarına bağlı olarak incelenmiştir. Sinterleme sıcaklığının artmasıyla birlikte buna bağlı olarak tane büyüklüğünün arttığı gözlemlenmiştir. Aynı eğilim La miktarının artmasına bağlı olarak da görülmüştür.

PLZT ince filmlerin yorulma dayançları Radiant-Ferroelektrik Test Cihazı ile 50 kHz de ve $\pm 15V$ da incelenmiştir. Kalıcı polarizasyonun toplam uygulanan döngü sayısına bağlı grafiği x dalarının logaritmik ölçeğinde çizilmiştir. Filmlerin kaçak akım karakterizasyonu da Ferroelektrik Test Cihazı ile $\pm 15V$ da elde edilmiştir. La miktarının artmasıyla kaçak akımda azalma saptanmıştır.

Anahtar Sözcükler: PLZT, (111)-Pt/Ti/SiO₂/Si-(100) altlık, Kimyasal Çözeltilen Biriktirme.

To my family,

ACKNOWLEDGEMENTS

First of all, I would like to thank to my supervisor, Prof. Dr. Macit Özenbaş, who shared his experience and opinions with me during this study. I am grateful for his advices that he has given to me in this period of work.

I am very grateful to all the staff of the Department of Metallurgical and Materials Engineering for their help. I want to thank specially to technician Necmi Avcı for X-Ray analysis and Cengiz Tan for SEM investigations. For the electrical measurements, I am thankful to assistant Barış Okatan and Dr. İbrahim Çam for their help and suggestions. I want to send special thanks to the Department of Chemistry and Physics for their help in the measurement of electrical and optical properties.

Finally, I would like to express that I am so grateful to my family for their endless love, support and patience during my life.

TABLE OF CONTENTS

ABSTRACT	iv
ÖZ	vi
DEDICATION	viii
ACKNOWLEDGEMENTS	ix
TABLE OF CONTENTS	x
LIST OF TABLES	xii
LIST OF FIGURES	xiv

CHAPTER

1. INTRODUCTION	1
2. LITERATURE SURVEY	4
2.1. Electronic Materials	4
2.1.1. PLZT Thin Films	4
2.2. Dielectric and Ferroelectric Properties of Materials	5
2.2.1. Dielectric Properties	5
2.2.2. Polarization	8
2.2.3. Hysteresis Loops	9
2.2.4. Polarization Fatigue in Ferroelectric Thin Films	10
2.3. Ferroelectric Materials	14
2.3.1. Ferroelectric Domains and Poling	15
2.3.2. Ferroelectric Thin Films	16
2.3.3. The Perovskite Structure and PLZT System	19
2.4. Chemical Solution Deposition Technique (CSD)	23
2.4.1. Process Chemistry of Sol-Gel Processing	25
2.4.2. Spin Coating Process	29
2.4.3. Drying, Firing and Annealing of PLZT Thin Films	31

3. EXPERIMENTAL PROCEDURE	33
3.1. Solution Preparation	33
3.1.1. Starting Materials	33
3.1.2. Solution Preparation	33
3.2. Coating of PLZT Thin Films	36
3.2.1. Preparation of Substrates	36
3.2.2. Spin Coating	36
3.2.3. Heat Treatment of PLZT Films	37
3.3. Characterization of PLZT Thin Films	39
3.3.1. Structural and Morphological Analysis	40
3.3.2. Dielectric and Ferroelectric Measurements	39
3.3.3. Ferroelectric Fatigue Analysis.....	40
3.3.4. Leakage Current Analysis	40
3.3.5. Differential Thermal Analysis (DTA/TD)	40
3.3.6. Optical Analysis	40
4. RESULTS AND DISCUSSION	41
4.1. Thin Films Preparation	42
4.2. Crystalline Film Formation	46
4.3. Thermal Analysis of the PLZT Thin Films	57
4.4. Composition and Morphology of the PLZT Thin Films	59
4.5. Dielectric Properties of the PLZT Thin Films	67
4.6. Ferroelectric Properties of the PLZT Thin Films	82
4.7. Optical Properties of the PLZT Thin Films	93
4.8. Ferroelectric Fatigue Analysis of PLZT Thin Films	101
4.9. Leakage Current Analysis of PLZT Thin Films	102
5. CONCLUSIONS AND FURTHER SUGGESTIONS	105
REFERENCES	109
APPENDIX	114

LIST OF TABLES

TABLE

2.1. Some studies on PLZT thin films from the literature	18
2.2. Literature review of precursors and solvents that were used for the production of PLZT thin films	28
3.1. Compositions and solvents that were used in this study	35
4.1. Compositions of $Pb_{1-x}La_x(Zr_yTi_{1-y})_{1-x/4}O_3$ thin films produced in this study and their crystal systems with electrical properties	42
4.2. EDS Analysis of PLZT thin films with different compositions from different regions of PLZT phase diagram	60
4.3. The grain sizes of PLZT thin films sintered at different temperatures	66
4.4. The grain sizes of PLZT thin films having different compositions sintered at the same temperature	67
4.5. Dielectric properties of $Pb_{1-x}La_x(Zr_yTi_{1-y})_{1-x/4}O_3$ thin films	71
4.6. Ferroelectric properties of PLZT film of composition $Pb_{0.96}La_{0.04}(Zr_{0.4}Ti_{0.6})_{0.99}O_3$ annealed at different temperatures and times	83

4.7. Ferroelectric properties of $\text{Pb}_{1-x}\text{La}_x(\text{Zr}_y\text{Ti}_{1-y})_{1-x/4}\text{O}_3$ PLZT thin films87

4.8. Optical properties of 9/65/35 PLZT thin film sintered at 750°C for 3 hours..99

LIST OF FIGURES

FIGURE

Fig 2.1. Equivalent circuit diagrams: (a) charging and loss current (b) loss tangent for a typical dielectric	7
Fig. 2.2. Ferroelectric (P-E) hysteresis loop [6]	9
Fig. 2.3. Atomic structure and polarization of PbTiO ₃ containing different oxygen vacancies [9]	12
Fig. 2.4. Schematic diagrams of the potential relief for oxygen vacancies in the states V^U and V^S . Potential energy barriers for vacancy transitions from V^U to V^S (ϵ_{us}) and back (ϵ_{su}), $\epsilon_{su} > \epsilon_{us}$ ◦—oxygen vacancy [9]	13
Fig 2.5. Illustration of changes in a ferroelectric material which transforms from a paraelectric cubic into ferroelectric tetragonal phase with temperature...14	
Fig. 2.6. The perovskite structure shown here for PbTiO ₃ which has a cubic structure in the paraelectric phase and tetragonal structure in the ferroelectric phase [7]	15
Fig. 2.7. The perovskite crystal structure ABO ₃ – A:Pb B:Zr,Ti	19
Fig. 2.8. Perovskite ABO ₃ crystal structure of PLZT [10]	20
Fig. 2.9. Room temperature phase diagram of PZT and PLZT diagram [10]	22
Fig. 2.10. The chart of sol-gel process	25
Fig. 2.11. Stages of the spin coating process [17]	30
Fig. 3.1. The flow diagram of solution preparation of PLZT thin films	34
Fig. 3.2. The flow chart for the production of PLZT thin films.....	38
Fig. 4.1. Micrograph of 450 nm PLZT thin film with composition of Pb _{0.98} La _{0.02} (Zr _{0.4} Ti _{0.6}) _{0.995} O ₃ sintered at 750 ⁰ C for 30 min	43
Fig. 4.2. Micrograph of 300 nm PLZT thin film with composition of Pb _{0.98} La _{0.02} (Zr _{0.4} Ti _{0.6}) _{0.995} O ₃ sintered at 700 ⁰ C for 1 hr	44

Fig. 4.3. Micrograph of 300 nm PLZT thin film with composition of $\text{Pb}_{0.98}\text{La}_{0.02}(\text{Zr}_{0.4}\text{Ti}_{0.6})_{0.995}\text{O}_3$ sintered at 800 ⁰ C for 1 hr	44
Fig. 4.4. Micrograph of 1.15 μm PLZT thin film with composition of $\text{Pb}_{0.96}\text{La}_{0.04}(\text{Zr}_{0.4}\text{Ti}_{0.6})_{0.99}\text{O}_3$ sintered at 750 ⁰ C for 1 hr	45
Fig. 4.5.(a) X-ray spectra of $\text{Pb}_{0.96}\text{La}_{0.04}(\text{Zr}_{0.4}\text{Ti}_{0.6})_{0.99}\text{O}_3$ thin film with thickness 600 nm and sintered at 600 ⁰ C for 1 hour. [sample no:44-1]	47
Fig. 4.5.(b) X-ray spectra of $\text{Pb}_{0.96}\text{La}_{0.04}(\text{Zr}_{0.4}\text{Ti}_{0.6})_{0.99}\text{O}_3$ thin film with thickness 600 nm and sintered at 600 ⁰ C for 2 hours. [sample no:44-2]	48
Fig. 4.5.(c) X-ray spectra of $\text{Pb}_{0.96}\text{La}_{0.04}(\text{Zr}_{0.4}\text{Ti}_{0.6})_{0.99}\text{O}_3$ thin film with thickness 600 nm and sintered at 600 ⁰ C for 3 hours. [sample no:44-3]	48
Fig. 4.5.(d) X-ray spectra of $\text{Pb}_{0.96}\text{La}_{0.04}(\text{Zr}_{0.4}\text{Ti}_{0.6})_{0.99}\text{O}_3$ thin film with thickness 600 nm and sintered at 600 ⁰ C for 1-2-3 hours	49
Fig. 4.6.(a) X-ray spectra of $\text{Pb}_{0.96}\text{La}_{0.04}(\text{Zr}_{0.4}\text{Ti}_{0.6})_{0.99}\text{O}_3$ thin film with thickness 600 nm and sintered at 700 ⁰ C for 1 hour. [sample no:46-1]	49
Fig. 4.6.(b) X-ray spectra of $\text{Pb}_{0.96}\text{La}_{0.04}(\text{Zr}_{0.4}\text{Ti}_{0.6})_{0.99}\text{O}_3$ thin film with thickness 600 nm and sintered at 700 ⁰ C for 2 hours. [sample no:46-2]	50
Fig. 4.6.(c) X-ray spectra of $\text{Pb}_{0.96}\text{La}_{0.04}(\text{Zr}_{0.4}\text{Ti}_{0.6})_{0.99}\text{O}_3$ thin film with thickness 600 nm and sintered at 700 ⁰ C for 3 hours. [sample no:46-3]	50
Fig. 4.6.(d) X-ray spectra of $\text{Pb}_{0.96}\text{La}_{0.04}(\text{Zr}_{0.4}\text{Ti}_{0.6})_{0.99}\text{O}_3$ thin film with thickness 600 nm and sintered at 700 ⁰ C for 1-2-3 hours	51
Fig. 4.7.(a) X-ray spectra of $\text{Pb}_{0.95}\text{La}_{0.05}(\text{Zr}_{0.52}\text{Ti}_{0.48})_{0.9875}\text{O}_3$ thin film with thickness 600 nm and sintered at 600 ⁰ C for 3 hours. [sample no:63-3] ...	53
Fig. 4.7.(b) X-ray spectra of $\text{Pb}_{0.95}\text{La}_{0.05}(\text{Zr}_{0.52}\text{Ti}_{0.48})_{0.9875}\text{O}_3$ thin film with thickness 600 nm and sintered at 700 ⁰ C for 3 hours. [sample no:62-3] ...	53
Fig. 4.7.(c) X-ray spectra of $\text{Pb}_{0.95}\text{La}_{0.05}(\text{Zr}_{0.52}\text{Ti}_{0.48})_{0.9875}\text{O}_3$ thin film with thickness 600 nm and sintered at 750 ⁰ C for 3 hours. [sample no:49-3] ...	54
Fig. 4.7.(d) X-ray spectra of $\text{Pb}_{0.95}\text{La}_{0.05}(\text{Zr}_{0.52}\text{Ti}_{0.48})_{0.9875}\text{O}_3$ thin film with thickness 600 nm and sintered at 600 ⁰ C-700 ⁰ C-750 ⁰ C for 3 hours.....	54
Fig. 4.8. X-ray spectra of $\text{Pb}(\text{Zr}_{0.65}\text{Ti}_{0.35})\text{O}_3$ thin film with thickness 700 nm and sintered at 750 ⁰ C for 3 hours. [sample no:50-3]	55
Fig. 4.9. X-ray spectra of $\text{Pb}_{0.94}\text{La}_{0.06}(\text{Zr}_{0.65}\text{Ti}_{0.35})_{0.985}\text{O}_3$ thin film with thickness 700 nm and sintered at 750 ⁰ C for 3 hours. [sample no:51-3]	55

Fig. 4.10. X-ray spectra of $\text{Pb}_{0.91}\text{La}_{0.09}(\text{Zr}_{0.65}\text{Ti}_{0.35})_{0.9775}\text{O}_3$ thin film with thickness 700 nm and sintered at 750°C for 3 hours. [sample no:52-3]	56
Fig. 4.11. Differential thermal analysis (DTA) curve of PLZT gel with composition of $\text{Pb}_{0.92}\text{La}_{0.08}(\text{Zr}_{0.65}\text{Ti}_{0.35})_{0.98}\text{O}_3$	58
Fig. 4.12. Thermogravimetry (TG) curve of PLZT gel with composition of $\text{Pb}_{0.92}\text{La}_{0.08}(\text{Zr}_{0.65}\text{Ti}_{0.35})_{0.98}\text{O}_3$	58
Fig. 4.13. The cross-section of PLZT film with a thickness 20 μm and composition $\text{Pb}_{0.96}\text{La}_{0.04}(\text{Zr}_{0.4}\text{Ti}_{0.6})_{0.99}\text{O}_3$, annealed at 700°C for 1 hr produced only for EDS analysis	61
Fig. 4.14. EDS analysis of the film shown on Fig. 4.13	61
Fig. 4.15. EDS spectra of $\text{Pb}_{0.91}\text{La}_{0.09}(\text{Zr}_{0.65}\text{Ti}_{0.35})_{0.9975}\text{O}_3$ powder.....	62
Fig. 4.16. EDS spectra of $\text{Pb}_{0.9}\text{La}_{0.1}(\text{Zr}_{0.4}\text{Ti}_{0.6})_{0.975}\text{O}_3$ powder.....	62
Fig. 4.17. EDS spectra of $\text{Pb}_{0.95}\text{La}_{0.05}(\text{Zr}_{0.52}\text{Ti}_{0.48})_{0.9875}\text{O}_3$ powder.....	63
Fig. 4.18. Cross sectional view of $\text{Pb}_{0.94}\text{La}_{0.06}(\text{Zr}_{0.65}\text{Ti}_{0.35})_{0.985}\text{O}_3$ -700 nm thick ...	63
PLZT film annealed at 750°C for 3 hours.....	63
Fig. 4.19a-b. Surface view of $\text{Pb}_{0.96}\text{La}_{0.04}(\text{Zr}_{0.4}\text{Ti}_{0.6})_{0.99}\text{O}_3$ -700 nm thick PLZT film annealed at 750°C for 3 hours.....	64
Fig. 4.20. Cross sectional image of 1.14 μm thick PLZT film on Pt/Ti/SiO ₂ /Si substrate with composition of $\text{Pb}_{0.96}\text{La}_{0.04}(\text{Zr}_{0.4}\text{Ti}_{0.6})_{0.99}\text{O}_3$, annealed at 700°C for 1 hr	65
Fig 4.21. Change of capacitance values of thin films with changing frequencies with respect to different sintering temperatures	68
Fig. 4.22. Change of dielectric constant values of thin films with changing frequencies with respect to different sintering temperatures	69
Fig. 4.23. Change of tangent loss values of $\text{Pb}_{0.96}\text{La}_{0.04}(\text{Zr}_{0.4}\text{Ti}_{0.6})_{0.99}\text{O}_3$ thin films (600 nm) with changing frequencies with respect to different sintering temperatures.....	70
Fig. 4.24. Change of dielectric constant of $\text{Pb}(\text{Zr}_{0.52}\text{Ti}_{0.48})\text{O}_3$ thin film with frequency	72
Fig. 4.25. Change of dielectric constant of $\text{Pb}_{0.95}\text{La}_{0.05}(\text{Zr}_{0.52}\text{Ti}_{0.48})_{0.9875}\text{O}_3$ thin film with frequency	73

Fig. 4.26. Dielectric constants of $\text{Pb}(\text{Zr}_{0.52}\text{Ti}_{0.48})\text{O}_3$ - $\text{Pb}_{0.95}\text{La}_{0.05}(\text{Zr}_{0.52}\text{Ti}_{0.48})_{0.9875}\text{O}_3$ thin films changing frequency.....	73
Fig. 4.27. Change of dielectric constant of $\text{Pb}(\text{Zr}_{0.65}\text{Ti}_{0.35})\text{O}_3$ thin film with frequency.....	74
Fig. 4.28. Dielectric constant-frequency curve of $\text{Pb}_{0.94}\text{La}_{0.06}(\text{Zr}_{0.65}\text{Ti}_{0.35})_{0.985}\text{O}_3$ thin film.....	75
Fig. 4.29. Dielectric constant –frequency curve of $\text{Pb}_{0.94}\text{La}_{0.09}(\text{Zr}_{0.65}\text{Ti}_{0.35})_{0.9775}\text{O}_3$ thin film.....	75
Fig. 4.30. Dielectric constant –frequency curves of $\text{Pb}_{0.94}\text{La}_{0.09}(\text{Zr}_{0.65}\text{Ti}_{0.35})_{0.9775}\text{O}_3$, $\text{Pb}_{0.94}\text{La}_{0.06}(\text{Zr}_{0.65}\text{Ti}_{0.35})_{0.985}\text{O}_3$, $\text{Pb}(\text{Zr}_{0.65}\text{Ti}_{0.35})\text{O}_3$ films sintered at 750°C for 3 hrs.....	76
Fig. 4.31. Change of dielectric constant of $\text{Pb}(\text{Zr}_{0.4}\text{Ti}_{0.6})\text{O}_3$ thin film with frequency.....	77
Fig. 4.32. Dielectric constant–frequency curve of $\text{Pb}_{0.96}\text{La}_{0.04}(\text{Zr}_{0.4}\text{Ti}_{0.6})_{0.99}\text{O}_3$ thin film.....	77
Fig. 4.33. Dielectric constant- frequency curve of $\text{Pb}_{0.94}\text{La}_{0.06}(\text{Zr}_{0.4}\text{Ti}_{0.6})_{0.985}\text{O}_3$ thin film.....	78
Fig. 4.34. Dielectric constant- frequency curve of $\text{Pb}_{0.9}\text{La}_{0.1}(\text{Zr}_{0.4}\text{Ti}_{0.6})_{0.975}\text{O}_3$ thin film.....	78
Fig. 4.35. Dielectric constant – frequency of $\text{Pb}_{0.86}\text{La}_{0.14}(\text{Zr}_{0.4}\text{Ti}_{0.6})_{0.965}\text{O}_3$ thin film.....	79
Fig. 4.36. Change of dielectric constant of $\text{Pb}_{0.76}\text{La}_{0.24}(\text{Zr}_{0.4}\text{Ti}_{0.6})_{0.94}\text{O}_3$ thin film with frequency.....	79
Fig. 4.37. Change of dielectric constant as a function of La content of x/65/35 thin film	80
Fig. 4.38. Change of dielectric constant as a function of La content of x/40/60 thin film	80
Fig. 4.39. The C-V curve for 600 nm thick PLZT film. (butterfly shaped curve indicating ferroelectric nature of the film)	84
Fig. 4.40. Change of remanent polarization of 600 nm $\text{Pb}_{0.96}\text{La}_{0.04}(\text{Zr}_{0.4}\text{Ti}_{0.6})_{0.99}\text{O}_3$ thin film as a function of sintering temperature	85

Fig. 4.41. Change of hysteresis behavior of 600 nm $\text{Pb}_{0.96}\text{La}_{0.04}(\text{Zr}_{0.4}\text{Ti}_{0.6})_{0.99}\text{O}_3$ thin film as a function of sintering temperature	85
Fig. 4.42. Ferroelectric hysteresis loop of $\text{Pb}(\text{Zr}_{0.65}\text{Ti}_{0.35})\text{O}_3$ thin film	88
Fig. 4.43. Ferroelectric hysteresis loop of $\text{Pb}_{0.94}\text{La}_{0.06}(\text{Zr}_{0.65}\text{Ti}_{0.35})_{0.985}\text{O}_3$ thin film	88
Fig. 4.44. Ferroelectric hysteresis loop of $\text{Pb}_{0.91}\text{La}_{0.09}(\text{Zr}_{0.65}\text{Ti}_{0.35})_{0.9775}\text{O}_3$ thin film	89
Fig. 4.45. Ferroelectric hysteresis loops of (x/65/35) PLZT thin films with 0%La and 9%La obtained 15V	89
Fig. 4.46. Ferroelectric hysteresis loops of (x/52/48) PLZT thin films with 0%La and 5%La obtained 15V.....	90
Fig. 4.47. Ferroelectric hysteresis loop of $\text{Pb}(\text{Zr}_{0.4}\text{Ti}_{0.6})\text{O}_3$ thin film	91
Fig. 4.48. Ferroelectric hysteresis loop of $\text{Pb}_{0.96}\text{La}_{0.04}(\text{Zr}_{0.4}\text{Ti}_{0.6})_{0.99}\text{O}_3$ thin film	91
Fig. 4.49. Ferroelectric hysteresis loop of $\text{Pb}_{0.94}\text{La}_{0.06}(\text{Zr}_{0.4}\text{Ti}_{0.6})_{0.985}\text{O}_3$ thin film	92
Fig. 4.50. Ferroelectric hysteresis loop of $\text{Pb}_{0.9}\text{La}_{0.1}(\text{Zr}_{0.4}\text{Ti}_{0.6})_{0.975}\text{O}_3$ thin film ..	92
Fig. 4.51. Ferroelectric hysteresis loop of $\text{Pb}_{0.86}\text{La}_{0.14}(\text{Zr}_{0.4}\text{Ti}_{0.6})_{0.965}\text{O}_3$ thin film ..	93
Fig. 4.52. Ferroelectric hysteresis loop of $\text{Pb}_{0.76}\text{La}_{0.24}(\text{Zr}_{0.4}\text{Ti}_{0.6})_{0.94}\text{O}_3$ thin film ..	93
Fig. 4.53. Schematic diagram of the modified envelope method: a weakly absorbing thin film on a completely transparent finite substrate	95
Fig. 4.54. Optical transmission spectra of PLZT thin film on quartz	98
Fig. 4.55. Refractive index-wavelength curve of the quartz substrate	100
Fig. 4.56. Plot of $(\alpha h\nu)^2$ versus photon energy	101
Fig. 4.57. Fatigue Curve of 600 nm thick $\text{Pb}_{0.96}\text{La}_{0.04}(\text{Zr}_{0.4}\text{Ti}_{0.6})_{0.99}\text{O}_3$ thin film sintered at 750°C for 3 hours	102
Fig. 4.58. Leakage Current Curve (J-E) for 600 nm thick La:Zr:Ti=6/40/60 thin film sintered at 750°C for 3 hours	103
Fig. 4.59. Leakage Current Curve (J-E) for 600 nm thick La:Zr:Ti=10/40/60 thin film sintered at 750°C for 3 hours	104

CHAPTER 1

INTRODUCTION

Thin film ferroelectrics are emerging as an important class of electronic materials. A key feature of the new technology is the relative ease with which miniature thin film ferroelectric devices may be integrated within semiconductor and hybrid monolithic packages. The flexibility of the technology has spawned imaginative engineering solutions to previously unrealisable designs. Until very recently, ferroelectrics have been used in the form of bulk ceramics and, where available, single crystals. Whilst these materials have proved a robust and reliable solution, producing thin layers (less than 10 mm) or dimensional tolerances better than a few microns has proved impractical [1].

Since the 1980s, methods have been developed to fabricate ferroelectrics in the form of thin films. The availability of thin-film ferroelectrics has encouraged the re-examination of previously unrealisable designs, resulting in the integration of ferroelectrics with semiconductor circuits, and the architectures combining the excellent properties of ferroelectrics with micromachined silicon structures. The future appears promising for the development of a new generation of ferroelectric devices, some of which will profoundly affect the evolution of the electronics industry over the next 50 years [1].

Thin films of ferroelectric devices are being considered for applications in numerous electronic and electro-optic devices ranging from non-volatile semiconductor memories, optical waveguide devices, spatial light modulators, switching capacitors for integrated circuitry, SAW devices, pyroelectric devices, and imaging sensors [2].

There are many techniques for deposition of ferroelectric thin films such as physical vapor deposition (PVD), sputtering, metal organic chemical vapor deposition (MOCVD) and sol-gel processing. Among these techniques, chemical solution deposition (CSD), a type of sol-gel, is a relatively new method for the production of ferroelectric thin films. The sol-gel processing has many advantages over the other processes in that it provides ease of chemical control, good homogeneity and low cost.

Sol-gel film processing involves the synthesis of a gel-precursor solution, or sol, which is applied to a substrate using spin-on or dip-coating techniques; the resulting gel layer is then heat treated to form a ceramic film. Generally, such treatments are carried out in two stages, by employing a hot plate firing step at a temperature such as 400°C, followed by a final firing treatment at temperatures between 600°C and 900°C [3].

For thin film ferroelectric applications, lead-based perovskite oxides such as lead zirconate titanate (PZT) and lead lanthanum zirconate titanate (PLZT) have been the major materials of interest because of their excellent ferroelectric, dielectric and electro-optic properties.

Thin films of lead lanthanum zirconate titanate (PLZT) $\text{Pb}_{1-x}\text{La}_x(\text{Zr}_{1-y}\text{Ti}_y)_{1-x/4}\text{O}_3$ have been investigated extensively over the last decade to exploit their high permittivities, large remanent polarization, electro-optic coefficients and optical transmittance for a wide variety of applications including decoupling capacitors, ferroelectric memories, optical modulators, displays, shutters and memories. Much of the interest in PLZT has been for optical applications. Some of the advantages of PLZT thin films integrated on semiconductors would be high bit density, non-volatile low voltage operation over a wide temperature range, short access and cycle times and retention of charge over long periods of time. PLZT thin films usually consist of a mixture of the perovskite and pyrochlore phases. Only the perovskite phase possesses desirable ferroelectric properties, because the crystal structure of pyrochlore phase is centro-symmetric.

The requirements for the integration of these films into devices are low processing temperature, high relative permittivity, large remanent polarization, small coercive field and leakage current and low fatigue [4].

The aim of this thesis study was to investigate the effects of La^{3+} on the dielectric, ferroelectric and electro-optic properties of the sol-gel processed PZT with the composition of $\text{La:Zr:Ti}=\text{x}/52/48$, $\text{La:Zr:Ti}=\text{x}/40/60$ and $\text{La:Zr:Ti}=\text{x}/65/35$ where x is the La content of the material. These compositions were chosen in different regions of PLZT phase diagram which are on the morphotropic phase boundary (MPB-x/52/48), in the tetragonal region (x/40/60) and in the rhombohedral region (x/65/35).

This report begins with a literature survey of PLZT thin films. First, a general description of ferroelectric and dielectric properties of materials were given to explain the terms that were used during the electrical measurements. Then ferroelectricity and perovskite structure were covered in correspondence with the PLZT system. In the last part of the chapter 2, production of PLZT thin films by chemical solution deposition was explained with details of the process. Third chapter includes the experimental procedure consisting of solution preparation, coating of samples and characterization of the films. In the fourth chapter, presentation and discussion of the experimental results on solution preparation, film deposition, sintering procedure, x-ray diffraction (XRD), film microstructure and morphology by SEM and electrical characterization of PLZT thin films were explained. Finally, the last chapter includes the conclusions and further suggestions related to the present work.

CHAPTER 2

LITERATURE SURVEY

2.1. Electronic Materials

Electronic materials provide essential functions (as capacitors, actuators, sensors, etc.) to a wide range of electrical and microelectronic devices and applications. This use has paralleled the dynamic growth in integrated circuit devices for telecommunications, computers, consumer electronics, and military and industrial applications [5].

2.1.1. PLZT Materials

With the versatility in being able to produce specific characteristics, PLZT materials continue to find increase use in electro-optic applications. These applications include optical shutters, modulators, displays, color filters, image storage devices and linear gate arrays for optical data processing. Factors for their success include high transparency, high electro-optic coefficients, fast response time, high electrical resistivity, direct current operation, low power consumption, memory capability, good property uniformity over large areas, moisture insensitivity, and low cost. Recently the use of PLZT materials has expanded to thin and thick film application. The reasons for this increase are their smaller sizes, less weight, lower operating voltage, higher speed, and easier fabrication than bulk PLZT materials [6].

2.2 Dielectric and Ferroelectric Properties of Materials

2.2.1. Dielectric Properties

Dielectric materials are known as insulators that do not conduct electricity and they have a large energy gap between the valence and conduction bands. Although they do not conduct electric current, they are polarizable under an electric field. The electric field shifts the charge balance in the material causing formation of electric dipole.

Dielectric materials can be used as an electrical insulator or as a capacitor. The dielectric constant of a material shows the ability of a material to store charge relative to vacuum. In literature, dielectric constant is known as relative dielectric constant or dielectric permittivity. In this report, it is always referred as dielectric constant.

The polarization P (coulomb/m²) that is induced in an insulating, polarizable material (a dielectric) by an applied electric field E (volt/meter) is given by:

$$P = \chi * E \quad \text{Eq. [2.1]}$$

where χ (farad/meter) is the dielectric susceptibility of the material. Equation [2.1] is valid only for linear materials or in a linear limit for nonlinear materials and, in general, P depends on higher-order terms of the field. The total surface charge density that is induced in the material by the applied field is given by the dielectric displacement D (coulomb/m²):

$$D = \varepsilon_0 E + P \quad \text{Eq. [2.2]}$$

where $\varepsilon_0 = 8.854 * 10^{-12}$ farad/meter is known as the dielectric permittivity of vacuum.

It follows from eq. [2.1] and eq. [2.2] that

$$D = \varepsilon_0 E + \chi E = \varepsilon_0 \delta E + \chi E = (\varepsilon_0 \delta + \chi) E = \varepsilon E \quad \text{Eq. [2.3]}$$

where $\varepsilon = \varepsilon_0 * \delta + \chi$ is the dielectric permittivity of the material and δ is Kronecker's symbol. For the most ferroelectric materials $\varepsilon_0 * \delta \ll \chi$ and $\varepsilon \approx \chi$. In practice, the relative dielectric permittivity, $K = \varepsilon / \varepsilon_0$, also known as the dielectric constant of the material, is often more used than the dielectric permittivity [7].

Therefore, we can get an equation:

$$D = \varepsilon_0 * K * E \quad \text{Eq.[2.4]}$$

Dielectric constant of the material can be written in terms of capacitance which is defined as charge stored in the material per unit voltage applied :

$$K = \frac{D}{\varepsilon_0 * E} = \frac{Q/A}{\varepsilon_0 * V/d} \quad \text{Eq. [2.5]}$$

Therefore,

$$Q = \varepsilon_0 * K * A/d * V = CV \quad \text{Eq. [2.6]}$$

where

$$C = \varepsilon_0 * K * \frac{A}{d} \quad \text{Eq. [2.7]}$$

$$C_0 = \varepsilon_0 * \frac{A}{d} \quad \text{Eq. [2.8]}$$

and

$$K = \frac{C}{C_0} = \frac{\varepsilon}{\varepsilon_0} \quad \text{Eq. [2.9]}$$

In the expressions above, A represents the area of the capacitive cell, d its thickness, C_0 and C the respective air and material capacitance, V the voltage impressed across the cell, and ϵ the material permittivity (F/m). Thus K represents the ratio of the permittivities or the charge stored in the capacitive cell relative to air or vacuum as dielectric [5].

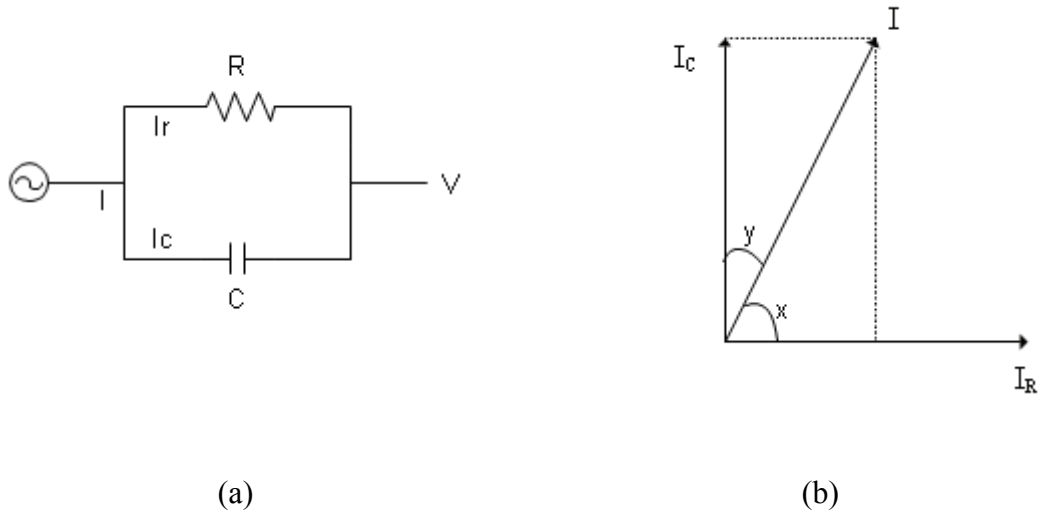


Fig 2.1. Equivalent circuit diagrams: (a) charging and loss current (b) loss tangent for a typical dielectric. (δ referred as y and ϕ referred as x)

For the case of V being sinusoidal, Eq. [2.6] may be written as

$$Q = CV_0 \exp(i\omega t)$$

Therefore,

$$I = \frac{dQ}{dt} = i\omega CV = i\omega C_0 \epsilon_0 KV \quad \text{Eq. [2.10]}$$

where I represents the current flow on discharge of the capacitive unit cell in time t [5].

As it can be seen from the Figure 2.1 above , the real dielectric current I has vector components I_C and I_R . I_R is represented by the circuit analog of a resistance in parallel with a capacitor and it gives the energy loss or power dissipated in material. I_C represents a capacitive current proportional to the charge stored in the material. This condition can be represented by a complex permittivity or dielectric constant as follows:

$$I = i\omega C_0 \varepsilon_0 (K - iK')V \quad \text{Eq. [2.11]}$$

$$= i\omega C_0 \varepsilon_0 KV + \omega C_0 \varepsilon_0 K'V \quad \text{Eq. [2.12]}$$

$$= I_C + I_R \quad \text{Eq. [2.13]}$$

Dissipation factor ($\tan\delta$) then can be defined as

$$\tan \delta = \frac{I_R}{I_C} = \frac{\omega C_0 \varepsilon_0 K'V}{\omega C_0 \varepsilon_0 KV} = \frac{K'}{K} \quad \text{Eq. [2.14]}$$

2.2.2. Polarization

Matter, electrically speaking, consists of positive atomic nuclei surrounded by negative electron clouds. Upon the application of an external electric field the electrons are displaced slightly with respect to the nuclei; induced dipole moments result and cause the so-called electronic polarization of the materials. When atoms of different types form molecules, they will normally not share their electrons symmetrically, as the electron clouds will be displaced toward the stronger binding atoms. Thus atoms acquire charges of opposite polarity, and an external field acting on these net charges will tend to change the equilibrium positions of atoms themselves. By this displacements of charged atoms or groups of atoms with respect to each other, a second type of induced dipole moment is created; it represents the atomic polarization of the dielectric. The asymmetric charge distribution between the unlike partners of a molecule gives rise, in addition to, to permanent dipole moments which exist also in the absence of an external field. Such moments experience a torque in an applied electric field that tends to orient

them in the field direction. Consequently, an orientation (dipole) polarization can arise [8]. These three mechanisms of polarization, characterized by an electronic polarizability α_e , an atomic polarizability α_a , and orientation or dipole polarizability α_d , are due to charges that are locally bound in atoms, in molecules, or in the structures of solids and liquids. In addition, charge carriers usually exist that can migrate for some distance through the dielectric. When such carriers are impeded in their motion, either because they become trapped in the material or on interfaces, or because they cannot be freely discharged or replaced at the electrodes, space charges and a macroscopic field distortion result. Such a distortion appears to an outside observer as an increase in the capacitance of the sample and may be distinguishable from a real rise of the dielectric permittivity. Thus we have to add to our polarization mechanisms a fourth one, a space charge polarization α_s . Assuming that these polarization mechanisms act independently so we may write total polarizability α of a dielectric material as the sum of the four terms indicated above [8].

2.2.3. Hysteresis Loops

The most important characteristic of ferroelectric materials is polarization reversal (or switching) by an electric field. At small values of the AC electric field, the polarization increases linearly with the field amplitude. This corresponds to segment AB in Figure 2.2. In this region, the field is not strong enough to switch domains with the unfavourable direction of polarization.

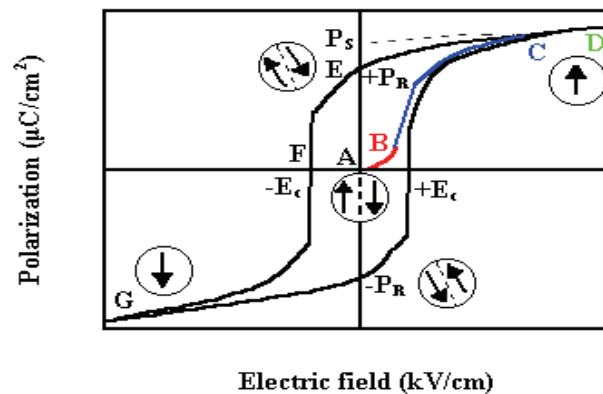


Fig. 2.2. Ferroelectric (P-E) hysteresis loop [6].

As the field is increased the polarization of domains with an unfavourable direction of polarization will start to switch in the direction of the field, rapidly increasing the measured charge density (segment BC). The polarization in this region is strongly non linear. Once all domains are aligned (point C) the ferroelectricity again behaves linearly (segment CD). If the field strength starts to decrease, some domains will back-switch, but at zero field the polarization is nonzero (point E). To reach a zero polarization state the field must be reversed (point F). Further increase of the field in the negative direction will cause a new alignment of dipoles and saturation (point G). The field strength is then reduced to zero and reversed to complete the cycle. The value of polarization at zero field (point E) is called the remanent polarization, P_r . The field necessary to bring the polarization to zero is called coercive field, E_c . The spontaneous polarization P_s is usually taken as the intercept of the polarization axis with the extrapolated linear segment CD [7].

2.2.4. Polarization Fatigue in Ferroelectric Thin Films

The reduction in switchable polarization of ferroelectric thin films due to electrical stress (polarization fatigue) is a major problem in ferroelectric nonvolatile memories.

The ferroelectric fatigue is defined as the loss of the switchable remanent polarization in a ferroelectric material as a function of the number of bipolar switching cycles. The mechanisms of the ferroelectric fatigue are presently not well understood. Both bulk and thin-film materials are susceptible to ferroelectric fatigue; in addition, suppression of the switchable polarization may be induced by treatments other than or in addition to field cycling.

Fatigue mechanisms in the ferroelectric films include : (i) formation of a surface layer; (ii) pinning of domain walls by defects segregated in the wall region; (iii) clamping of polarization reversal by volume defects; (iv) suppression of nucleation of oppositely oriented domains at the surface; (v) damage of

electrode/film interface. The role of oxygen vacancies in the fatigue process of ferroelectric thin films has been considered in several models. Several mechanisms may play a role in the fatiguing process:

2.2.4.1. Possible role of oxygen vacancies

Several models of the polarization fatigue in ferroelectric thin films are based on the observation that oxygen vacancies accumulate at the film/electrode interface during field cycling. Scoot et al suggested that oxygen-deficient regions grow into the bulk, effectively screening part of the film from the applied field and leading to polarization loss. Another model proposed that the polarization loss is due to structural damage at the film/electrode interface due to entrapped oxygen vacancies.

It has been further suggested that creation of an oxygen-vacancy-rich region at the film/metal electrode interface may lead to the formation of an n-type layer near the interface. The presence of this layer increases the electron injection rate in the film during field cycling. Injected electronic carriers may get trapped at the domain walls leading to domain-wall pinning and polarization suppression.

2.2.4.2. Electronic charge trapping and domain-wall pinning

The model is based on the idea that free electronic charge carriers pin domain walls by being trapped in the domain-wall region. The free electronic charge carriers may be attracted to the domain-wall regions where there is a discontinuity in polarization, and thus decrease the energy of the walls. If the charges become trapped at these positions, the movement of the walls will be restricted. The charge carriers may be injected into films from the electrodes, created in the material during the field cycling or can be produced by illumination of the films by UV light. The polarization fatigue process is interpreted as a dynamic competition between domain-wall pinning due to electronic charge trapping and field-assisted unpinning of the domain walls [7].

It is known that the oxygen vacancies are the main source of charge carriers in ABO_3 type materials. It has been suggested a model for polarization changes in PLZT ceramics. The model shows that there are two types of oxygen vacancies (V^U and V^S) in the Ti-O-Ti (or Zr-O-Zr) chains of the PLZT structure, which significantly influence the polarization ;

(a) the atoms in the crystal lattice are displaced near the V^U vacancies in such a manner, that the dipole moments in the direction of the c -axis of the next crystal cells “above” and “below” the vacancy have opposite directions (so-called “tail-to-tail” configuration). Thus the mean polarization near such a vacancy is approximately zero (Fig. 2-3b, d).

(b) the V^S vacancy does not affect the polarization itself (Fig. 2-3a, c) [9].

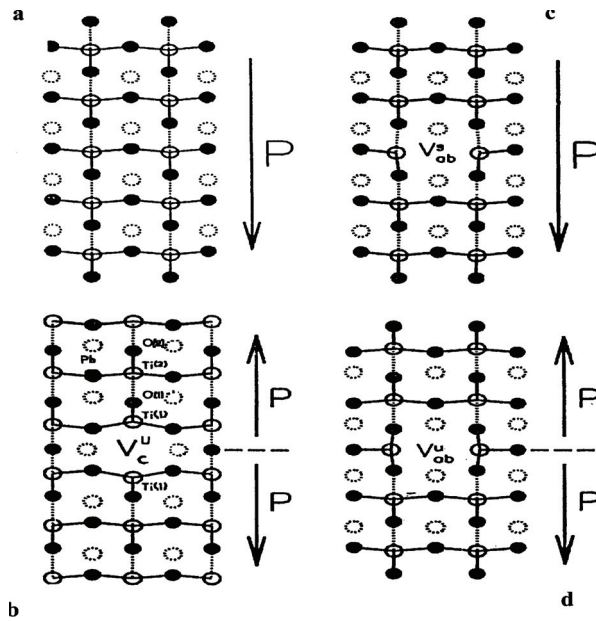


Fig. 2.3. Atomic structure and polarization of $PbTiO_3$ containing different oxygen vacancies [9].

It was assumed that the energy minimum of the V^S vacancy lies below that of the V^U vacancy. The potential barriers for vacancies to transit from one state (V^U) to another (V^S) and back, $\epsilon_{us} < \epsilon_{su}$ (see Fig. 2.4) [9].

It was accounted that a change in La content, which influences the material structure, can also influence the properties of vacancy transitions. It was showed that a phase transition takes place in the region of La concentration between 6% and 8%, where the initial micron-sized domains in the material vanish and so-called nanodomains appear with a size of about 5 nm. La content influences vacancy transitions from different states. At a higher La content, where small nanodomains exist, the energy barriers for vacancy transitions from a state V^U to state V^S and back is supposed to be smaller than in samples with lower La concentration. This may be connected to easier polarization changes (taking place vacancy transitions from one state to another) in small nanodomains compared to micro-domains because it happens in a small area and the interaction with other domains is weak [9]. Easier polarization changes means that longer fatigue life of the films can be obtained.

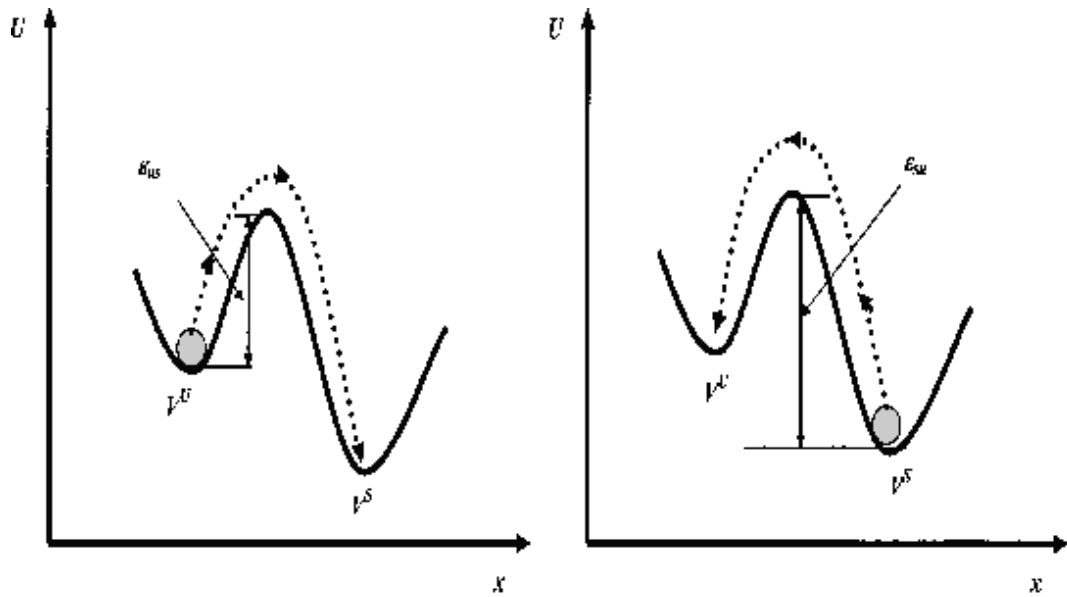


Fig. 2.4. Schematic diagrams of the potential relief for oxygen vacancies in the states V^U and V^S . Potential energy barriers for vacancy transitions from V^U to V^S (ϵ_{us}) and back (ϵ_{su}), $\epsilon_{su} > \epsilon_{us}$ ◯—oxygen vacancy [9].

2.3. Ferroelectric Materials

A material is ferroelectric if it has a spontaneous polarization P_s which can be reversed in sense or reoriented by the application of an electric field larger than the coercive field. Most ferroelectric materials undergo a structural phase transition from a high temperature nonferroelectric (or paraelectric) phase into a low temperature ferroelectric phase.

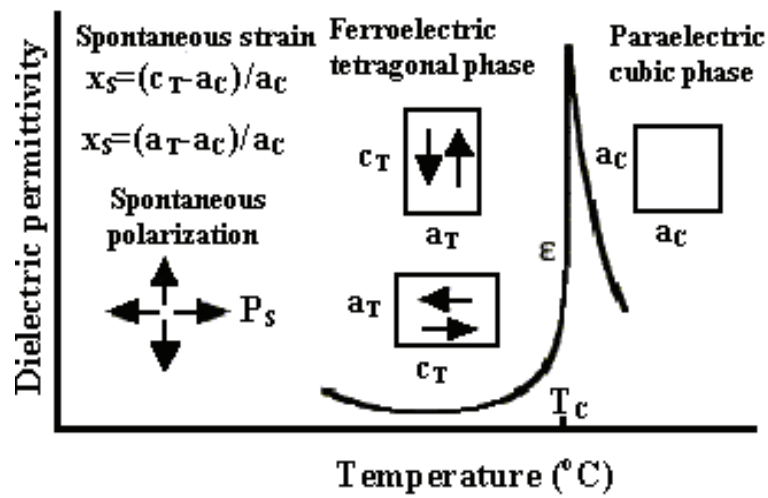


Fig 2.5. Illustration of changes in a ferroelectric material which transforms from a paraelectric cubic into ferroelectric tetragonal phase with temperature [7].

The symmetry of the ferroelectric phase is always lower than the symmetry of the paraelectric phase. The temperature of the phase transition is called the Curie point, T_c . Above the Curie point the dielectric permittivity falls off with temperature according to the Curie-Weiss law

$$\epsilon = \epsilon_0 + \frac{C}{T - T_0} \approx \frac{C}{T - T_0} \quad \text{Eq. [2.15]}$$

where C is the Curie constant, T_0 ($T_0 \leq T_c$) is the Curie-Weiss temperature.

2.3.1. Ferroelectric Domains and Poling

Perovskite crystals, explained after this section, have the general formula ABO_3 where the valance of A cations is from +1 to +3 and of B cations from +3 to +6. As shown in figure 2.6, the structure may be viewed as consisting of BO_6 octahedra surrounded by A cations. Most of the ferroelectric materials that are of practical interest have perovskite structure and many form a solid solution with $PbTiO_3$. The spontaneous polarization in $PbTiO_3$ lies along the c_T -axis of the tetragonal unit cell and crystal distortion is usually described in terms of shift of O and Ti ions relative to Pb. In the ferroelectric phase the crystal is spontaneously strained with $a_T \leq a_C \leq c_T$ where a_T and a_C are the a -axes of the tetragonal and cubic unit cell.

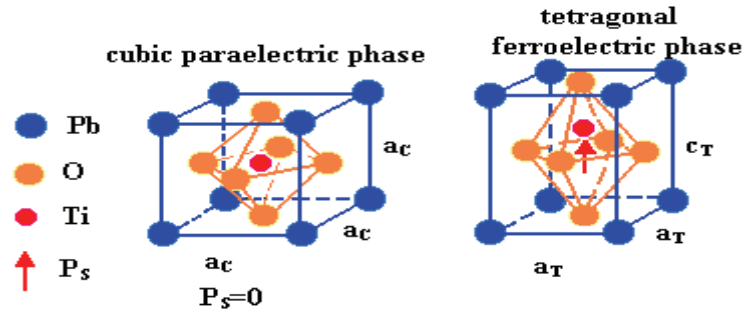


Fig. 2.6. The perovskite structure shown here for $PbTiO_3$ which has a cubic structure in the paraelectric phase and tetragonal structure in the ferroelectric phase [7].

The directions along which the polarization will develop depends on the electrical and mechanical boundary conditions imposed on the sample. The regions of the crystal with uniformly oriented spontaneous polarization are called ferroelectric domains. The region between two domains is called the domain wall. The walls which separate domains with oppositely oriented polarization are called 180° walls and those which separate regions with mutually perpendicular polarization are called 90° walls.

Ferroelectric domains form to minimize the electrostatic energy of depolarizing fields and the elastic energy associated with mechanical constraints to which the ferroelectric material is subjected as it is cooled through paraelectric-ferroelectric phase transition.

Due to complex set of elastic and electric boundary conditions at each grain, ferroelectric grains in ceramics and polycrystalline films are always split into many domains. If the direction of the spontaneous polarization through the material is random or distributed in such a way as to lead to zero net polarization, the pyroelectric and piezoelectric effects of individual domains will cancel and such material is neither pyroelectric nor piezoelectric. Polycrystalline ferroelectric materials may be brought into a polar state by applying a strong electric field. This process, called poling, cannot orient grains, but can reorient domains within individual grains in the direction of the field.

2.3.2. Ferroelectric Thin Films

Current trends in the electronics and optoelectronics industries involving computing, data processing, sensing and communications all point toward a continuing need for improved materials and new multifunctional structures in such application areas as memories, modulators, switches, shutters, mixers, sensors, imagers and displays. This was brought on by the demand for higher speed, smaller size and more integration in present-day devices, and is being sustained by the promise of even greater levels of miniaturization and integration in the future.

This continuing and unabated drive toward higher density and greater integration has led many of the new technologies away from bulk materials and to their thin film counterparts. Aside from the obvious advantages already stated, ferroelectric (FE) thin films offer additional benefits including (1) lower operating voltage, (2) more economical processing, (3) greater design flexibility and (4) the ability to fabricate unique nano-level composite structures. Equally important, but not so obvious, is the fact that many materials which are difficult, if not impossible, to fabricate into dense form as a bulk material are relatively easy to

produce as thin films. Furthermore, the sintering temperatures of films are usually hundreds of degrees centigrade lower than that of the bulk, and this can often be the deciding factor in favor of films.

Most popular ferroelectric compositions are PZT, PLZT, LiNbO₃, KNbO₃, Bi₄Ti₃O₁₂, etc. Among them, PLZT thin films are desirable candidates for ferroelectric and electro-optic applications.

The dielectric and ferroelectric properties of PLZT thin films studied in the literature are listed in Table 2.1.

Table 2.1. Some studies on PLZT thin films from the literature.

Substrate	Materials used for solution	Composition (La/Zr/Ti)	Solvent	Dielectric constant(K)	Loss tangent(tanδ)	Remanent polarization Pr ($\mu\text{C}/\text{cm}^2$)	Coercive field (Ec) (kV/cm)	Sintering temp ($^{\circ}\text{C}$)	Ref.
Pt/Ti/Si	Lead Acetate trihydrate-Zr propoxide-Tiisopropoxide-La acetate hydrate	8/65/35	2-Methoxy ethanol, nitric acid, acetic acid	440 (at 10kHz)	0.038	6	47	750	[19]
Si/SiO ₂ /Ti/Pt	Lead Acetate trihydrate-Zr (n) propoxide-tetrabutyl titanate-La nitrate hydrate	9/65/35	2-Methoxy ethanol, acetic acid	700 (at 100kHz)	0.021	10.30	36.3 kV/cm	600	[22]
Glass	Lead Acetate trihydrate-Zr (n) propoxide-titanium isopropoxide -La acetate	9/65/35	n propanol, acetic acid	1750 (1kHz) (1.7 μm thickness)	0.022	9.57	14.71 kV/cm	750 (5 min)	[26]
Platinized silicon	Lead Acetate trihydrate-Zr propoxide-Tiisopropoxide-La acetate hydrate	10/50/50	-	1330	-	3	-	750 (5 min-RTA)	[34]
Si/SiO ₂ /Ti/Pt	Lead Acetate trihydrate, tetrapropyl zirconate-tetra iso propylorthotitanate -La nitrate hexahydrate	5/52/48	Acetic acid, acetyl acetone (stabilization), 2 methoxyethanol (dilution)	741 \pm 59	-	1.9	20.60	650 (10min)	[23]
P/Ti/SiO ₂ /Si	Lead Acetate trihydrate-Zr (n) propoxide-titanium diisopropoxide-La acetate hydrate	5/53/47	propanediol, acetylacetone	700 (1kHz)	0.04	14	66	700 (15 min)	[33]
P/Ti/SiO ₂ /Si	Lead Acetate trihydrate, tetrapropyl zirconate-tetra iso propylorthotitanate -La nitrate hexahydrate	5/53/47	propanediol, acetylacetone	1630 (0.5 kHz)	-	6	46	750 (40 min)	[21]
Si	Lead acetate trihydrate, tetrabutyl titanate, lanthanum nitrate, zirconium oxide nitrate	5/60/40	Ethylene glycol monomethyl ether, acetylacetone, formamide (drying control chemical additive (DCCA), acetylacetone (chelating agent)	455 \pm 2	0.07 \pm 0.01	14 \pm 1	50 \pm 2	700	[3]
Platinum and quartz	Lead acetate trihydrate, zirconium acetylacetonate, titanium isopropoxide, lanthanum acetate hydrate	8/65/35	2-methoxyethanol, acetic acid (as catalyst)	250	0.016	25	30	650	[4]
Pt/SiO ₂ /Si	Lead tetra-acetate or lead acetyl acetone, titanium isopropoxide, zirconium isopropoxide, different lanthanum precursors	10/40/60	pyridine, toluene	590 \pm 11	0.039 \pm 0.014	4.9 \pm 0.39	3.22 \pm 0.12	650	[35]

2.3.3. The Perovskite Structure and PLZT System

PZT has perovskite crystal structure which has a general chemical formula ABO_3 , where O is oxygen, A represents a cation (Pb) with a larger ionic radius, and B (Zr,Ti) a cation with a smaller ionic radius. As shown in Fig.2.7, six oxygen atoms form the octahedral cage where the smaller ion (B) resides. This is called the B site. A network of these oxygen octahedra corner-links together creating the interstices, called A sites, where the larger ions (A) are located. Because of the difference of valency between the A and B atoms, some of these A and B sites are vacant in order to maintain electrical neutrality in the structure. Although the perovskite structure seems to have a center of symmetry at the center of the octahedron, the unit cell of PLZT is nonsymmetrical. Thus it falls into the category as noncentrosymmetric.

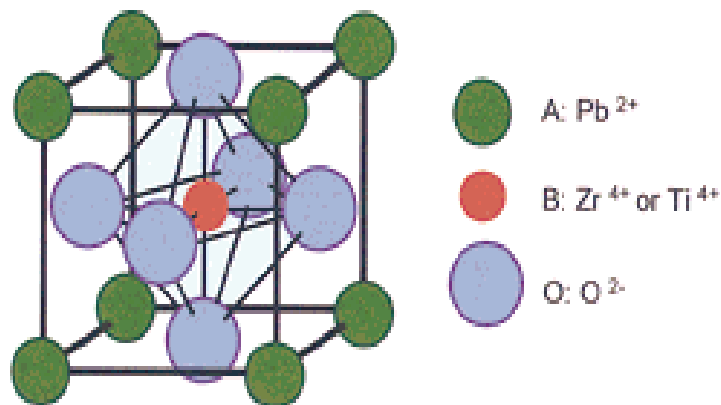


Fig. 2.7. The perovskite crystal structure ABO_3 – A:Pb B:Zr,Ti

For a unit cell of PLZT materials, the perovskite structure has either Zr^{4+} or Ti^{4+} ions occupying the B sites, and the Pb^{2+} and La^{3+} ions at the A sites [8]. La^{3+} substitutes for Pb^{2+} , acting as donor (see Fig. 2.8). For every two atoms of La^{3+} introduced into the lattice, one lead vacancy occurs.

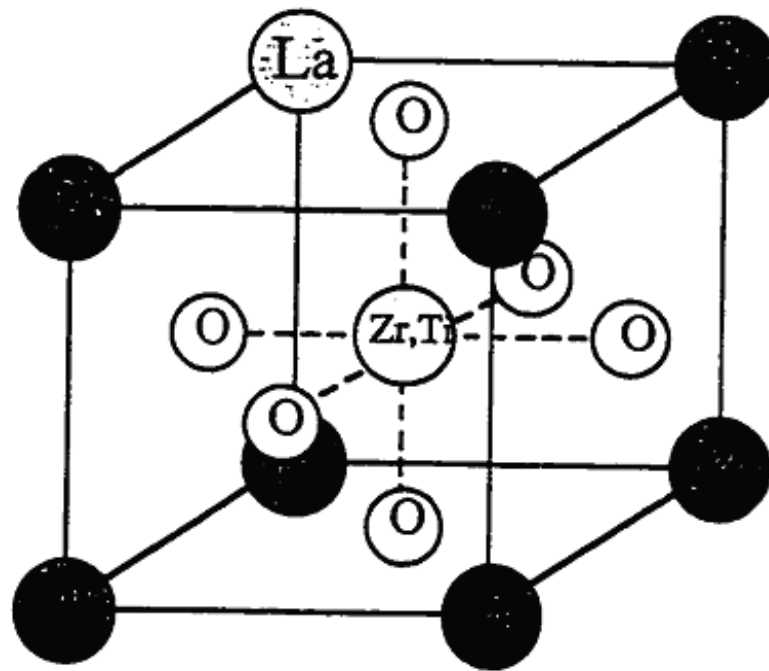
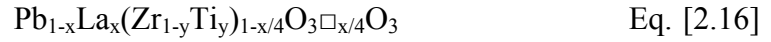
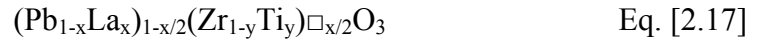


Fig. 2.8. Perovskite ABO_3 crystal structure of PLZT [10].

A general formula for the PLZT system can be given as



Since La^{3+} substitutes for Pb^{2+} , charge balance is maintained by the creation of lattice site vacancies as stated above. The formula assumes B-site vacancies but it has been shown that both A-site and B-site vacancies coexist and this would provide excess Pb^{2+} ions which would be expelled from the lattice as PbO vapor. Excess PbO , however, is useful in densification process by forming a liquid-phase at the grain boundaries, eliminating porosity and inhibiting grain growth in early stages of densification. Alternately used A-site formula,



assumes electrical neutrality is maintained by Pb vacancies, one Pb vacancy for every two atoms of La present [10].

The phase diagram of PLZT system at room temperature is shown in Fig.2.9. There are some interesting features of this phase diagram which is limited to 30%La with all the range for end members PbZrO_3 to PbTiO_3 : (1) complete solid solution exists between the end members (PbZrO_3 to PbTiO_3) and La in small concentrations, (2) small variations in La content produce rather large changes in areas of phase stability, (3) the solubility of La in the PZT structure is limited to less than 35%, (4) increasing La decreases the stability of the ferroelectric phases (FE) (rhombohedral and tetragonal) in favor of the nonferroelectric cubic and antiferroelectric, AFE, (a nonpolar phase possessing adjacent, oppositely aligned polar unit cells) orthorombic phases.

The slanted-loop area which is connected from $\text{PbZr}_{0.94}\text{Ti}_{0.06}\text{O}_3$ up to La additions 27at% existing along the ferroelectric-paraelectric phase boundary represents a region of diffuse, metastable ferroelectric phases that can be electrically induced with a sufficiently high electric field. This phenomenon is commonly described as relaxor behavior, and materials within this region exhibit a

quadratic electro-optic effect. In this phase area, the PLZT compositions are transparent. On the other hand, compositions in the mixed-phase region are opaque in contrast to single phase, cubic materials [10].

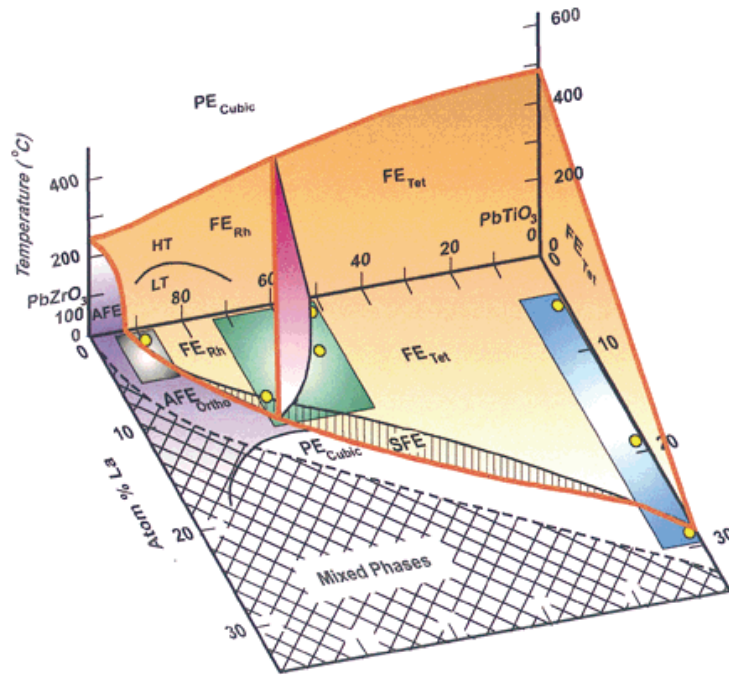


Fig. 2.9. Room temperature phase diagram of PZT and PLZT diagram [10].

2.4. Chemical Solution Deposition Technique (CSD)

Many techniques have been used for the preparation of polycrystalline films of ferroelectrics. Sol-gel processing is a relatively new method and appears to be very promising because of the apparent ease of control of chemical uniformity at the molecular level providing that the proper precursors are used and the heat treatment is carefully carried out. The entire sol-gel process begins with the preparation of the liquid solution having the most ideal structural groups corresponding to that in the crystalline ferroelectric, maintaining proper liquidity just prior to the deposition onto the substrate, dipping or spin-coating in a controlled atmosphere and then heat treatment also under controlled atmospheres [11].

There are many advantages of sol-gel processing. It not only allows for materials to have any oxide composition, but it also permits the production of new hybrid organic-inorganic materials which do not exist naturally. Sol-gel processing also has many other advantages. Very pure products are obtained by simply purifying the precursors either by distillation, crystallization or electrolysis.

There are other more fundamental advantages related to sol-gel processing. For instance, the kinetics of the various chemical reactions can easily be controlled by the low processing temperatures and by the often dilute conditions. The nucleation and growth of the primary colloidal particles can also be controlled in order to give particles with a given shape, size and size distribution.

Sol-gel processing offers the most outstanding advantages for mixed oxide systems in which the chemical homogeneity of the various elements can be controlled down to the atomic level. This is the case of the Lead Lanthanum Zirconium Titanates (PLZT). This condition is, however, virtually impossible to achieve when solid powders are mechanically mixed such as in the conventional process; and hence the optical transparencies obtained are, in this case, not as high as those obtained by sol-gel processing.

The greatest limitation to the synthesis of ceramics by sol-gel processing is still the cost of the precursors and especially that of alkoxides. Most of these alkoxides are nonetheless quite easy to make; especially if they do not tend to polymerize. Moreover, alkoxides can also be mixed with much cheaper metal salts provided that a purification step is included in the procedure.

Precipitation and co-precipitation techniques are also used and are sometimes even considered as a side branch of sol-gel processing. The chemical reactions concerned in this case are the same as those occurring in sol-gel synthesis; they lead to the production of colloidal particles, but can also be dispersed into a stable sol [11].

Many variations can be brought to the sol-gel synthesis of ceramics. In fact, sol-gel processing does not only designate a unique technique, but a very broad type of procedures that centralizes around a single scheme as presented in Fig.2.10. The first step of any sol-gel process always consists in selecting the precursors of the wanted materials. It is the precursor that, by its chemistry, lead the reaction towards the formation of either colloidal particles or polymeric gels. When the future material is composed of several components (i.e., when several oxides are mixed together), then the use of a combination of different precursors and procedures enhances different chemical synthesis and hence different products. The colloidal particles obtained can then be precipitated and treated according to one of the conventional processing techniques, such as cold pressing, hot-pressing and sintering, in order to produce the desired ceramic. Sols and gels can also be spun into fibers or transformed through one of other various techniques into a coating material. If a gel powder for melting purposes is required, than the gel may be dried and no special cares need to be given to fracturation. On the other hand, controlled gelation and drying leads to the formation of monosized droplets which can reach several hundred micrometers in diameter. It is also possible to synthesize small ceramic parts by using, after a simple sintering, an all monolithic process that avoids fracturation. Furthermore, the size of pores can also be controlled by supercritical drying or by the use of surfactants [11].

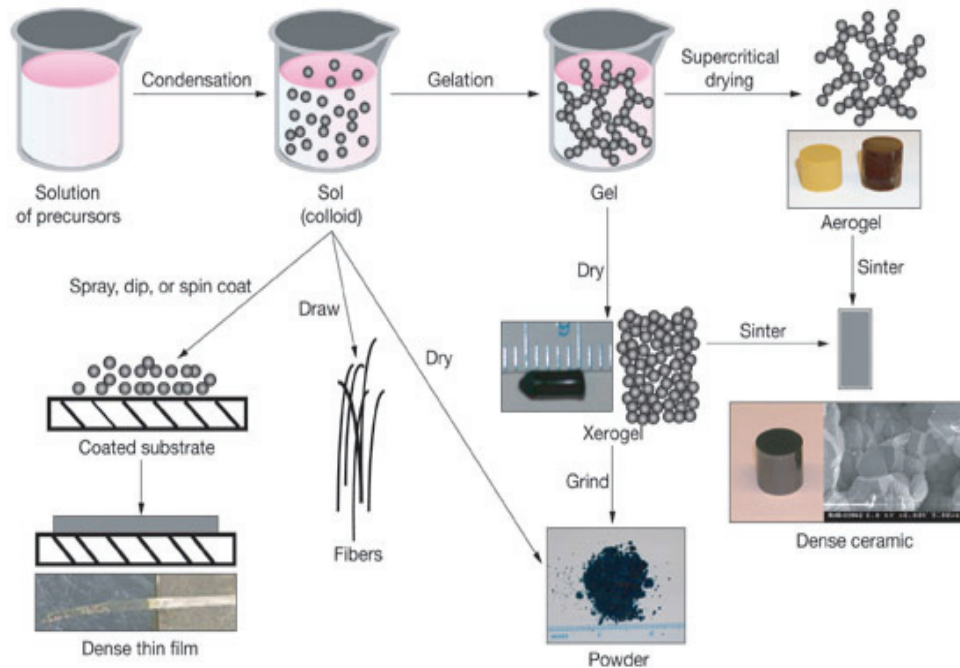


Fig. 2.10. The chart of sol-gel process.

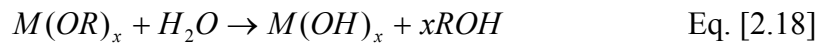
2.4.1. Process Chemistry of Sol-Gel Processing

As it can be seen from the Fig. 2.10 that the sol-gel process can be categorized into three routes. The first one called “colloidal” method involves the dispersion of colloidal particles in a liquid to form a sol and then the destabilization of the sol to produce a gel which is subsequently dried, to form a porous ceramic, and fired to crystallize and/or densify the material [12]. The second method involves the production of powders precipitated from the sol. The resulting powders are then dried and processed using traditional ceramic processing techniques. The third approach is the polymerization of organometallic compounds such as alkoxides to produce a gel with a continuous network [13].

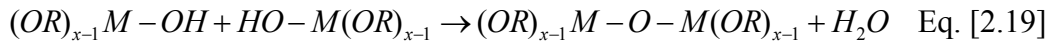
A “colloid” is a suspension in which the dispersed phase is so small that gravitational forces are negligible and interactions are dominated by short-range forces, such as van der Waals attractions and surface charges. The inertia of

dispersed phase is so small enough that it exhibits Brownian motion, a random walk driven by momentum imported by molecules of the suspending medium. A “sol” is a colloidal suspension of solid particles in a liquid [14].

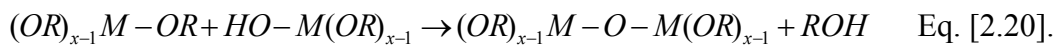
Metal oxides are members of the family of metallorganic compounds, which have an organic ligand attached to a metal or metalloid atom. Organometallic compounds are defined as having direct metal-carbon bonds, not metal-oxygen-carbon linkages as in metal alkoxides; thus alkoxides are not organometallic compounds, although that usage turns up frequently in the literature. Metal oxides; are popular precursors because they react with water. The reaction is called hydrolysis, because a hydroxyl ion becomes attached to the metal atom



Two partially hydrolyzed molecules can link together in a condensation, such as



or



These reactions causes the formation of a metal-oxygen-metal bridge, which constitutes the backbone of any oxide ceramic structure. Continued condensation leads to an increase in the density of metal-oxygen-metal crosslinks until eventually gelation or precipitation occurs [15].

The basic principle of the sol-gel process is to form a solution of the elements of the desired compounds in an organic solvent, polymerize the solution to form a gel, and dry and fire this gel to displace the organic components and form a final inorganic oxide.

Important and typical precursors for making sol-gel solutions are alkoxides of the general composition $M(O-R)_n$, where R is an alkyl radical (CH_3, C_2H_5 , etc.). Their properties and reactions affect the preparation process and determine the product features. Inorganic and organic salts can also be used for introducing some oxides into multicomponent systems. The precursors are dissolved in a suitable organic solvent to form the solution. In order to get the solution with a high concentration of necessary components and proper viscosity, surface tension and boiling point, the solvent must be carefully selected. Table 2.2 summarizes the precursors and solvents used in the literature.

In order to obtain a suitable solution for making films, various properties of solution are adjusted. Different alkoxides of different elements show a wide range of reactivity toward H_2O which makes the preparation of multicomponent homogeneous systems difficult and also presents difficulties with premature gelation during film processing. This can be overcome by adding a chelating organic ligand into the solution to control the hydrolysis rates of highly reactive alkoxide. The gelation of a solution means the formation of a network in the solution. The hydrolysis and polycondensation of organometallic compounds such as alkoxides leads gelation. During the drying stage the wet coating is converted to a relatively dry, harder coating and considerable shrinkage of the coating occurs. It is at this stage that problems related to film cracking and surface smoothness in the final film become most acute.

Table 2.2. Literature review of precursors and solvents that were used for the production of PLZT thin films.

Precursors	Solvents	Substrate	Reference
Lead Acetate trihydrate-Zr propoxide-Ti isopropoxide-La acetate hydrate	2-Methoxy ethanol, nitric acid, acetic acid	Pt/Ti/Si	[19]
Lead Acetate trihydrate-Zr (n) propoxide-tetrabutyl titanate-La nitrate hydrate	2-Methoxy ethanol , acetic acid	Pt/Ti/SiO ₂ /Si	[22]
Lead Acetate trihydrate-Zr (n) propoxide-titanium iso propoxide -La acetate	acetic acid, n propanol (to insure homogeneity), ethylene glycol (to improve the surface flatness)	ITO-coated glass	[26]
Lead acetate trihydrate, Ti isopropoxide, Zr n-butoxide, La 2-methoxyethoxide	ethanol, acetylacetone (chelating agent)	Pt/Ti/SiO ₂ /Si	[32]
Lead Acetate trihydrate-Zr (n) propoxide-titanium diisopropoxide bisacetylacetonate-La acetate hydrate	propanediol, acetylacetone	Pt/Ti/SiO ₂ /Si	[33]
Lead Acetate trihydrate, tetrapropyl zirconate-tetra iso propylorthotitanate -La nitrate hexahydrate	Acetic acid, acetyl acetone (stabilization), 2 methoxyethanol (dilution)	Pt/Ti/SiO ₂ /Si	[21]
Lead Acetate trihydrate, tetrapropyl zirconate-tetra iso propylorthotitanate -La nitrate hexahydrate	Acetic acid, acetyl acetone (stabilization), 2 methoxyethanol (dilution)	Pt/Ti/SiO ₂ /Si	[23]
Lead acetate trihydrate, lanthanum nitrate hexahydrate, zirconium tetrabutoxide, titanium-tetra-isopropoxide	2-methoxyethanol	Pt (111)/Ti/SiO ₂ /Si	[31]
Lead acetate trihydrate, zirconium acetylacetonate, titanium isopropoxide, lanthanum acetate hydrate	2-methoxyethanol, acetic acid (as catalyst)	Platinum and quartz	[4]
Lead acetate trihydrate, tetrabutyl titanate, lanthanum nitrate, zirconium oxide nitrate	Ethylene glycol monomethyl ether, acetylacetone, formamide (drying control chemical additive (DCCA), acetylacetone (chelating agent)	-	[3]

The firing step converts the gel coating into a densified complex oxide film. This process includes the removal of residual –OH or –OR groups by polycondensation reactions, pyrolysis of the organic compounds or groups left in the film into carbon, oxidation of the carbon, and gradual densification of the film [16].

2.4.2. Spin Coating Process

Sol-gel is one of the simplest and most common technique of applying thin films onto wafers. The material to be made into the coating must be dissolved or dispersed into a solvent of some kind, and this coating solution is then deposited onto the surface and spun-off to leave a uniform layer for subsequent processing stages and ultimate use.

Bornside et. al. [17] states that there are four distinct stages to the spin coating process shown on Fig 2.11. Stage 3 (flow controlled) and stage 4 (evaporation controlled) are the two stages that have the most impact on final coating thickness.

The first stage is the deposition of the coating fluid onto the wafer or substrate. It can be done using a nozzle that pours the solution out, or it could be sprayed onto the surface, etc. Usually this dispense stage provides a substantial excess of coating solution compared to the amount that will ultimately be required in the final coating thickness. For many solutions it is often beneficial to dispense through a sub-micron sized filter to eliminate particles that could lead to flaws. Another potentially important issue is whether the solution wets the surface completely during the dispense stage. If not, then incomplete coverage can result.

The second stage is when the substrate is accelerated up to its final, desired, rotation speed. This stage is usually characterized by aggressive fluid expulsion from the wafer surface by the rotational motion. Because of initial depth of fluid on the wafer surface, spiral vortices may briefly be present during this stage; these would form as a result of the twisting motion caused by the inertia that the top of

the fluid layer exerts while the wafer below rotates faster and faster. Eventually, the fluid is thin enough to be completely co-rotating with the wafer and any evidence of fluid thickness differences is gone. Ultimately, the wafer reaches its desired speed, and the fluid is thin enough that the viscous shear drag exactly balances the rotational accelerations.

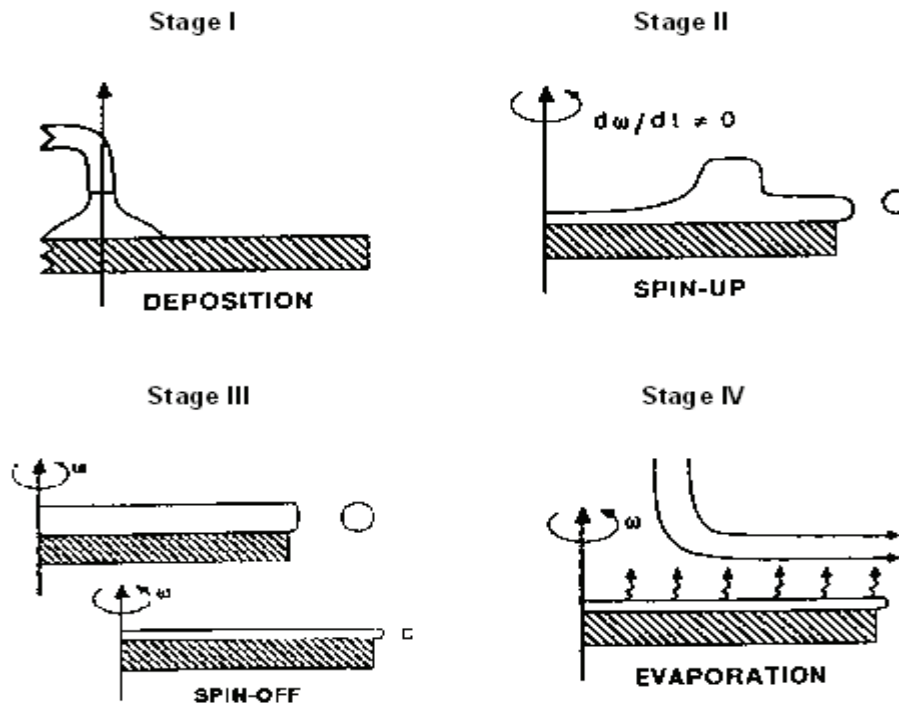


Fig. 2.11. Stages of the spin coating process [17].

The third stage is when the substrate is spinning at a constant rate and fluid viscous forces dominate fluid thinning behavior. This stage is characterized by gradual fluid thinning. Fluid thinning is generally quite uniform, though with solutions containing volatile solvents, it is often possible to see interference colors “spinning off”, and doing so progressively more slowly as the coating thickness is reduced. Edge effects are often seen because the fluid flows uniformly outward, but must form droplets at the edge to be flung off. Thus, depending on the surface tension, viscosity, rotation rate, etc., there may be a small bead of coating thickness difference around the rim of the final wafer.

The fourth stage is when the substrate is spinning at a constant rate and solvent evaporation dominates the coating thinning behavior. As the prior stage advances, the fluid thickness reaches a point where the viscosity effects yield only rather minor net fluid flow. At this point, the evaporation of any volatile solvent species will become the dominant process occurring in the coating. In fact, at this point the coating effectively “gels” because as these solvents are removed the viscosity of the remaining solution will likely rise.

The prediction of Mayerhofer about factors affecting the film thickness includes the spin rate (f), the initial viscosity (η_i), and the evaporation rate (e):

$$h \propto f^{2/3} \eta_i^{1/3} e^{1/3} \quad \text{Eq. [2.21]}$$

2.4.3. Drying, Firing and Annealing of PLZT Thin Films

After preparation of the sol-gel solution, heating treatment of the deposited film is the final step for the formation of PLZT thin films.

First stage for the ceramic film from the sol-gel solution is the drying step by which water and solvent in the solution are removed. There are some stages occurring during drying process. In the first stage called constant rate period, liquid flows to the surface to replace that which is lost to evaporation. This is the stage where the most shrinkage and warping occurs as a result of capillary pressure differentials within the film. The gel matrix reaches a point called critical point where it can no longer shrink to release the solvent necessary to reduce the capillary pressure. At this point the liquid meniscus enters the matrix and drying from within the film begins. This is when a crack is the most likely to appear in the material. In the first falling rate period, the last layers of solvent are removed by flow along the pores walls to the surface. During second falling rate period, the volatilized solvent is removed by the diffusion of vapor to the surface.

The timing of these stages is intimately linked to the structure of the film. Cracking is the most important subject that should be considered during the drying. The gel consists of two phases, the network solid phase and connected

pores filled with liquid phase. Initially the surface of the gel is covered with liquid phase. The liquid phase evaporates so that the solid phase is exposed. Since the solid network is wetted by the liquid phase, the liquid phase tends to cover all the solid surface capillary force will be imposed on the solid network. Since the gel network is compliant, the gel shrinks under capillary force as the liquid evaporates [16].

Firing treatment of the dried films is carried out at temperatures between 350-500⁰C for the removal of organics in the film.

The firing process changes the organic precursor film into an inorganic ceramic film by the pyrolysis of organometallic compounds. During this process, the lead acetate dehydrates, melts and decomposes. In this stage, the dried film becomes wet again and the organic compounds begin to decompose. The internal stress is relaxed and the volume change of the film continues. At the end of this stage, the organic film changes to a fine mixture of oxides of lead, zirconium, titanium and free carbon. At higher temperatures, the free carbon oxides and the mixture of oxides transforms to an amorphous PLZT film [18].

CHAPTER 3

EXPERIMENTAL PROCEDURE

In this study, PLZT thin films were produced on (111)-Pt/Ti/SiO₂/Si-(100) substrates with the compositions selected from the PLZT phase diagram. To obtain the best properties of the films in terms of their electrical and structural investigations, solution preparation, coating and heat treatment processes were carried out carefully.

3.1. Solution Preparation

3.1.1. Starting Materials

For the selection of the starting compounds, high metal content, high solubility in the selected solvent, thermal decomposition without evaporation and chemical compability should be considered carefully. Lead acetate trihydrate Pb(CH₃COO)₂.3H₂O (Aldrich Co., purity 99+%), zirconium (IV) propoxide Zr(C₃H₇O)₄ (Aldrich Co., 70wt.% solution in 1-propanol), titanium (IV) isopropoxide Ti[(CH₃)₂CHO]₄ (Aldrich Co., purity 97%) and lanthanum acetate hydrate La(CH₃COO)₃.xH₂O (Aldrich Co., purity 99.9%) were used as starting materials. 2-Methoxyethanol C₃H₈O₂ (Aldrich Co., purity 99%) was used as the solvent and deionized water was used as the diluting solvent.

3.1.2. Solution Preparation

In this study, all the solutions with different compositions was set to 0.4M/40ml. The preparation of these solutions was started with mixing lead

acetate and the solvent 2-methoxyethanol. This solution was then heated to a temperature of 90°C until all lead acetate dissolved in the solvent. At that temperature calculated amount of lanthanum was added to that solution. After addition of lanthanum, solution was stirred about 30 minutes until a clear solution was obtained. The second solution based on Ti and Zr was then prepared at room temperature. Zr propoxide and Ti isopropoxide are mixed together with 2-methoxyethanol. This solution was stirred at room temperature for 25-30 minutes. When both solutions were clear meaning that all the solid particles dissolved in the system, they were refluxed at 75°C for 2 hours and stirred gently. At the end of this period, this solution was cooled to room temperature. To adjust that solution to 40ml, additional 2-methoxyethanol and water were added to get its final form. Finally, it was stirred for 24 hours for homogenization. This solution was kept as a stock and clear for a few months. The flow diagram of the PLZT solution preparation is shown on Fig. 3.1.

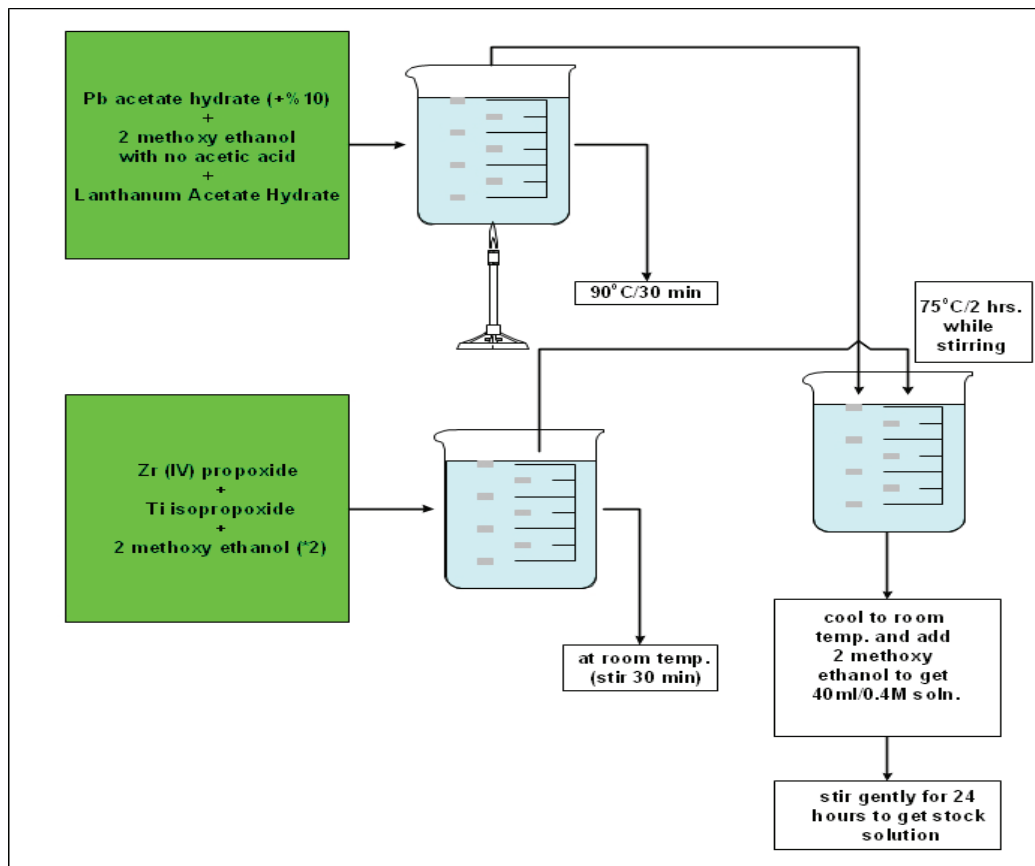


Fig. 3.1. The flow diagram of solution preparation of PLZT thin films.

In this study, 11 solutions with different compositions, selected on the phase diagram of PLZT system, were prepared. Selected compositions and the solvents used are listed in the Table 3.1.

Table 3.1. Table of compositions and solvents that were used in this study.

Chemical Formula	La:Zr:Ti	Solvent used
$Pb(Zr_{0.52}Ti_{0.48})O_3$	0/52/48	2-Methoxyethanol
$Pb_{0.95}La_{0.05}(Zr_{0.52}Ti_{0.48})_{0.9875}O_3$	5/52/48	2-Methoxyethanol
$Pb(Zr_{0.4}Ti_{0.6})O_3$	0/40/60	2-Methoxyethanol
$Pb_{0.96}La_{0.04}(Zr_{0.4}Ti_{0.6})_{0.99}O_3$	4/40/60	2-Methoxyethanol
$Pb_{0.94}La_{0.06}(Zr_{0.4}Ti_{0.6})_{0.985}O_3$	6/40/60	2-Methoxyethanol
$Pb_{0.9}La_{0.1}(Zr_{0.4}Ti_{0.6})_{0.975}O_3$	10/40/60	2-Methoxyethanol
$Pb_{0.86}La_{0.14}(Zr_{0.4}Ti_{0.6})_{0.965}O_3$	14/40/60	2-Methoxyethanol+acetic acid
$Pb_{0.76}La_{0.24}(Zr_{0.4}Ti_{0.6})_{0.94}O_3$	24/40/60	2-Methoxyethanol+acetic acid
$Pb(Zr_{0.65}Ti_{0.35})O_3$	0/65/35	2-Methoxyethanol
$Pb_{0.94}La_{0.06}(Zr_{0.65}Ti_{0.35})_{0.985}O_3$	6/65/35	2-Methoxyethanol
$Pb_{0.91}La_{0.09}(Zr_{0.65}Ti_{0.35})_{0.9775}O_3$	9/65/35	2-Methoxyethanol

For the preparation of PLZT thin films with the chemical formula $Pb_{0.91}La_{0.09}(Zr_{0.65}Ti_{0.35})_{0.9775}O_3$ (La:Zr:Ti=9/65/35), 6.161 gr lead acetate trihydrate was dissolved in 7.5-8 gr 2-methoxyethanol and heated to 90°C. Lead acetate was taken 10% excess because that amount was lost during sintering process. After stirring about 5-10 min. at that temperature, 0.46 gr La acetate hydrate was added to that solution. They are mixed in each other for 30 minutes. For the second solution, 4.38 gr Zr propoxide was added firstly with 30% percent excess because of being a 70 wt.% solution. Then 1.73 gr Ti isopropoxide was mixed with

Zr propoxide. The quantity of Ti isopropoxide was taken 10% excess because some Ti was removed during preparation of the solution. 14-15 gr of 2-methoxyethanol was added to second solution and mixed with Ti and Zr compounds at room temperature. First and second solutions were mixed together at 75⁰C for 2 hours. After cooling to room temperature, distilled water and 2-methoxyethanol (2-3 ml) were added to adjust the solution to 40 ml.

In this study, La was introduced as lanthanum acetate hydrate; however, when a high lanthanum content was needed such as in solutions with the composition 24/40/60 (La:Zr:Ti), lanthanum acetate hydrate was so difficult to dissolve. Therefore in the present study 2-methoxyethanol/acetic acid mixture was used to ensure the complete dissolution of lanthanum acetate hydrate.

3.2. Coating of PLZT Thin Films

3.2.1. Preparation of Substrates

Surfaces of the substrates must be clean to have a good deposition and adhesion of films on substrates (111)-Pt/Ti/SiO₂/Si-(100). First of all, substrates were cut from the wafer with the dimension of 1cm to 1cm. Then they were rinsed in acetone by ultrasonic cleaner for 15 minutes.

3.2.2. Spin Coating

The spin coating process was performed by Chemat Technology Spin Coater. After cleaning of small pieces of substrates, they were stuck on the head of the spin coater with the help of double-sided tape. Excess amount of solution was added onto the substrate using pasteur pipette.

The film thickness can be adjusted by changing the spinning rate of the spin coater. In this study, films were coated at 3000 rpm for 30 seconds. For the production of crack free films, very thin films were obtained. In order to get required thickness of the films, individual layer coating steps were repeated.

Pyrolysis cycles were done between these layers. As the thickness of the films increases and reaches a critical value, films crack due to shrinkage during drying process.

3.2.3. Heat Treatment of PLZT Films

The heat treatment of the PLZT thin films was begun with the drying process at 150⁰C for 15 minutes. This process is important because of the shrinkage taking place during removal of water. For the removal of organics the thin film was fired at 450⁰C for 15 minutes in the preheated tube furnace. These steps were repeated until desired thickness obtained. Fig. 3.2. shows the route that was followed from the solution preparation to heat treatment of the films.

Final heat treatment of the films is sintering. This was carried out to change the crystal structure from amorphous to crystalline perovskite phase. Sintering process was done in the conventional furnace with the heating rate of 12⁰C/min and cooling rate of 8⁰C /min.

Sintering of the thin films in terms of its temperature and time plays an important role in the development of microstructure and resulting ferroelectric and dielectric properties.

In this work, temperature and time of sintering process were considered as two effective parameters on the electrical and structural properties of the films. In order to understand the effect of temperature, four distinct temperatures 600⁰C, 650⁰C, 700⁰C and 750⁰C were chosen. Duration of the sintering process was determined as 1 hour, 2 hours and 3 hours. These three sintering times were applied with all the temperatures to PLZT thin films in order to see optimized conditions.

The thickness of the films was kept constant while changing the sintering time and temperature. During the heat treatment optimization, thickness of all films was 600 nm (4 layers).

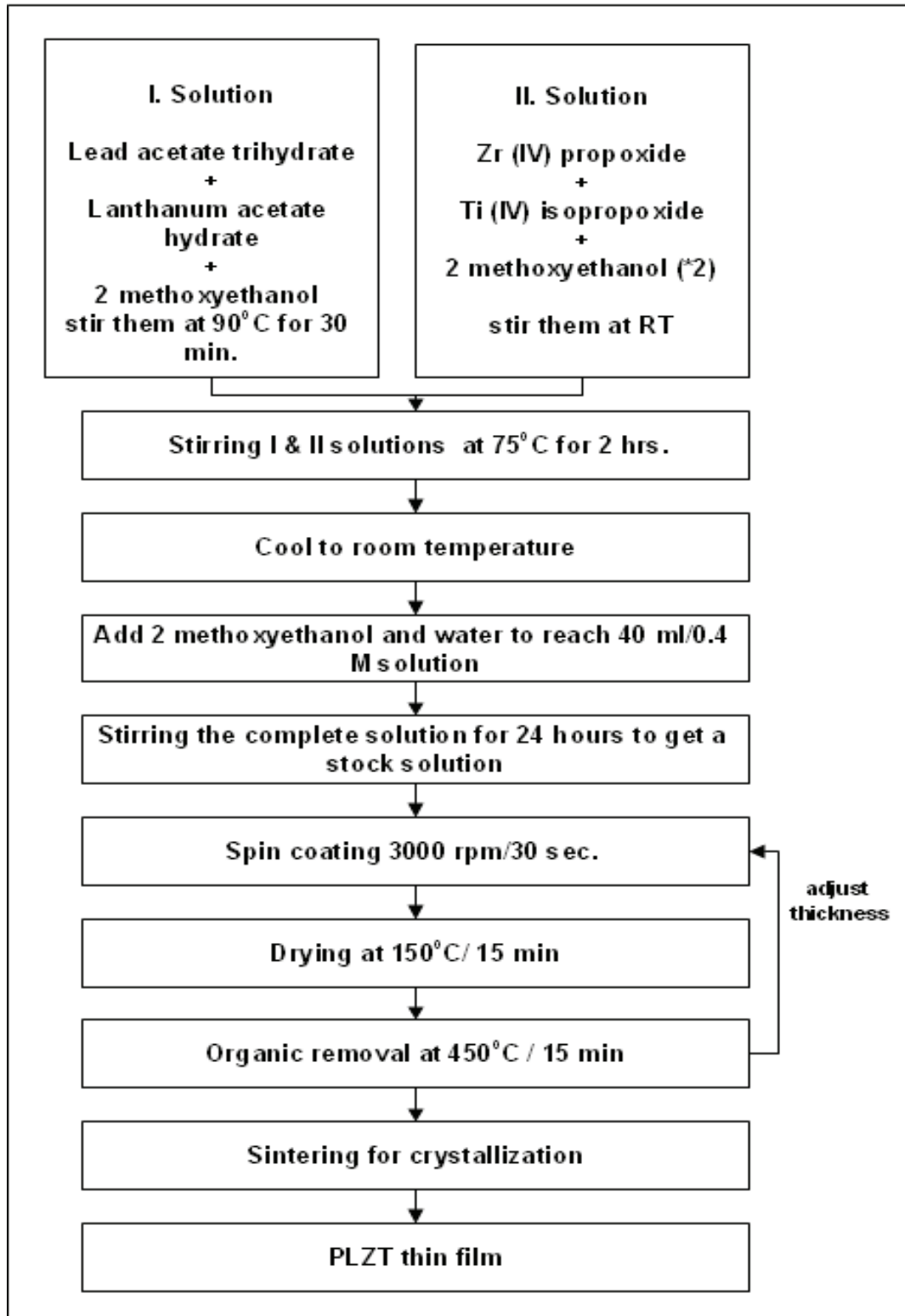


Fig. 3.2. The flow chart for the production of PLZT thin films

3.3. Characterization of PLZT Thin Films

3.3.1. Structural and Morphological Analysis

Chemical and microstructural analysis of the PLZT thin films were carried out by JEOL JSM-6400 Scanning Electron Microscope (SEM) equipped with an Energy Dispersive Spectrometer (EDS analyser). With the help of SEM, thickness and film surfaces were investigated. At the surface, composition analyses were carried out and thicknesses of the films were measured by the cross-section view. X-Ray diffraction analysis were performed by using Rigaku (Japan) Diffractometer between angles 20° - 60° (2θ) with $\text{Cu}(K_{\alpha})$ radiation. To investigate the surface cracks and Ag contact of the films, Nikon Type 104 Stereo Microscope was used. The photographs of the samples were taken by Nikon COOLPIX 4500 in order to measure diameter of the contacts on the films.

3.3.2. Dielectric and Ferroelectric Measurements

Dielectric measurements of the PLZT thin films were carried out by Hewlett-Packard 4194A impedance gain phase analyzer. Dielectric constant (K) and dielectric loss ($\tan\delta$) of the films were measured at frequencies in the range of 1kHz-1MHz with the oscillation level of 0.5V at room temperature. In addition to these properties, capacitance- bias voltage (C-V) curves between the voltage range of (-10V,10V) were also investigated. Ferroelectric measurements were performed by the Ferroelectric Tester (Radiant Technologies, Inc.). Hysteresis Curves (Polarization ($\mu\text{C}/\text{cm}^2$) – Electric field (kV/cm)) were obtained with the applied voltages in the range of 5V-15V.

3.3.3. Ferroelectric Fatigue Analysis

The data for the ferroelectric fatigue curves of the PLZT thin films were collected by Ferroelectric Tester. Change of remanent polarization as a function of fatigue cycles was obtained at 50 kHz-15V.

3.3.4. Leakage Current Analysis

Leakage current analysis was carried out by the Radiant Ferroelectric Tester at $\pm 15\text{V}$. Leakage current density (J) as a function of electric field (E) was obtained.

3.3.5. Differential Thermal Analysis (TG/DTA)

The differential thermal analysis (DTA) is a thermal technique in which the heat effects, associated with physical or chemical changes, are recorded as a function of temperature and time as the substance is heated at a uniform rate. Heat or enthalpic changes, either exothermic or endothermic, are caused by phase transitions, such as crystalline structure inversions, dehydration reactions, dissociation reactions or decomposition reactions and chemical reactions. Generally speaking, phase transitions, dehydration, reduction, and some decomposition reactions produce endothermic effects, whereas crystallization, oxidation, and some decomposition reactions produce exothermic effects [18].

TG (thermogravimetry) and DTA (differential thermal analysis) analysis were conducted by Simultaneous Thermogravimetric Analyser and Differential Thermal Analyser (SETARAM) in Central Lab at METU. For these analyses, a PLZT solution with a specific composition was chosen and dried at 100°C for 8 hours in the low temperature furnace to obtain a gel powder. TG/DTA analysis were done from room temperature up to 900°C with a heating rate of $3^{\circ}\text{C}/\text{min}$.

3.3.6. Optical Analysis

Optical transmittance of the films was measured by UV-VIS Spectrometer in the Department of Chemistry at METU. Transmittance(%)-Wavelength (nm) curve (optical transmission spectrum) was drawn in the range of 200 nm-800 nm and optical properties such as refractive index (n), absorption coefficient (α) and extinction coefficient (k) of the films were obtained by using that curve and modified envelope method.

CHAPTER 4

RESULTS AND DISCUSSION

In this study, aim was to investigate the effects of La^{+3} element on lead zirconate titanate (PZT) thin films in terms of their ferroelectric, dielectric and optical properties. To achieve this goal, La^{+3} was tried to be substituted into PZT system by chemical solution deposition. Preparation of homogeneous and stock solutions played a very important role in the production of crack free PLZT thin films. In order to get the optimum conditions of the films with respect to their electrical and optical features, process parameters such as crystallization temperature, crystallization time and thickness of the films were taken into account as primary parameters. After finding the optimum parameters, effect of composition on dielectric, ferroelectric and optical properties was investigated. Scanning electron microscopy (SEM), X-ray diffraction and EDS analysis were used to observe the surface morphology, phases in the system, composition and thicknesses of the PLZT films. Dielectric and ferroelectric properties were determined by ferroelectric tester. Dielectric constant and tangent loss values were measured with the changing frequency (1kHz-1MHz). Remanent polarization and coercive field values were also obtained with the change of electric field. For the optical properties, transmittance-wavelength curves were drawn and some constants such as refractive index (n), absorption coefficient (α) and extinction coefficient (k) of the films were calculated by modified envelope method.

In this study, there are 11 compositions selected from different regions of PLZT phase diagram. First compositions without any La content were chosen from tetragonal, rhombohedral regions and on the morphotropic phase boundary (MPB). Then La content was increased and its effects on the properties of films were investigated. Figure 4.1. shows the compositions of the films studied in this thesis.

Table 4.1. Compositions of $\text{Pb}_{1-x}\text{La}_x(\text{Zr}_y\text{Ti}_{1-y})_{1-x/4}\text{O}_3$ thin films produced in this study and their crystal systems with electrical properties.

Composition of the films	Crystal structure
$\text{Pb}(\text{Zr}_{0.52}\text{Ti}_{0.48})\text{O}_3$	Ferroelectric Tetragonal (on MPB)
$\text{Pb}_{0.95}\text{La}_{0.05}(\text{Zr}_{0.52}\text{Ti}_{0.48})_{0.9875}\text{O}_3$	Ferroelectric Tetragonal (on MPB)
$\text{Pb}(\text{Zr}_{0.4}\text{Ti}_{0.6})\text{O}_3$	Ferroelectric tetragonal
$\text{Pb}_{0.96}\text{La}_{0.04}(\text{Zr}_{0.4}\text{Ti}_{0.6})_{0.99}\text{O}_3$	Ferroelectric tetragonal
$\text{Pb}_{0.94}\text{La}_{0.06}(\text{Zr}_{0.4}\text{Ti}_{0.6})_{0.985}\text{O}_3$	Ferroelectric tetragonal
$\text{Pb}_{0.9}\text{La}_{0.1}(\text{Zr}_{0.4}\text{Ti}_{0.6})_{0.975}\text{O}_3$	Ferroelectric tetragonal
$\text{Pb}_{0.86}\text{La}_{0.14}(\text{Zr}_{0.4}\text{Ti}_{0.6})_{0.965}\text{O}_3$	Relaxor Ferroelectric Pseudocubic
$\text{Pb}_{0.76}\text{La}_{0.24}(\text{Zr}_{0.4}\text{Ti}_{0.6})_{0.94}\text{O}_3$	Paraelectric cubic
$\text{Pb}(\text{Zr}_{0.65}\text{Ti}_{0.35})\text{O}_3$	Ferroelectric rhombohedral
$\text{Pb}_{0.94}\text{La}_{0.06}(\text{Zr}_{0.65}\text{Ti}_{0.35})_{0.985}\text{O}_3$	Ferroelectric rhombohedral
$\text{Pb}_{0.91}\text{La}_{0.09}(\text{Zr}_{0.65}\text{Ti}_{0.35})_{0.9775}\text{O}_3$	Ferroelectric rhombohedral

4.1. Thin Film Preparation

As it is stated in the previous chapters that thin film production starts with preparation of a homogeneous and stock solution. This is a very important step for getting crack free and smooth surfaces. In order to reach these aims, solution must be prepared carefully.

There are many parameters affecting the quality of the solution such as atmospheric conditions, type of precursor, solvent used and heating temperature. In this study, experiments were done in the open atmosphere. Actually, it should be done in glove box conditions in order to prevent reactions between air and precursors. There are some critical points at which someone should be very careful. One of them is the addition of Ti-isopropoxide into Zr-propoxide with the solvent 2 methoxyethanol. During this stage, Ti-isopropoxide was immediately

reacted with the humidity in the air and precipitated in the solvent. Although the solution temperature was increased to solve the precipitated particles, it never came back to its clear form. Therefore, steam of Ti isopropoxide was removed while it was being poured into the solution with a pipette. This was a remedy for the precipitated solutions. This is the reason of adding 10% excess Ti containing precursor to the solution. Another problem that was encountered during this process is the precipitation of lead acetate trihydrate in 2-methoxyethanol. As it is mentioned in the third chapter, lead acetate trihydrate was dissolved in 2-methoxyethanol and heated to 90°C. Then, second solution containing Zr and Ti was mixed with this solution at that temperature. If the first solution is cooled to room temperature, it would immediately precipitate while cooling. Therefore, the mixing of the two solutions should be performed at the temperature of 90°C.

At the beginning of this study, the way that was followed in the solution preparation was different from the final route. Lead acetate trihydrate was dissolved in 2-methoxyethanol and heated to 120°C. At that temperature the solution was boiled and mixed with the other solution based on Ti and Zr. Figure 4.1. shows the microstructure of the thin film which was produced by this way.

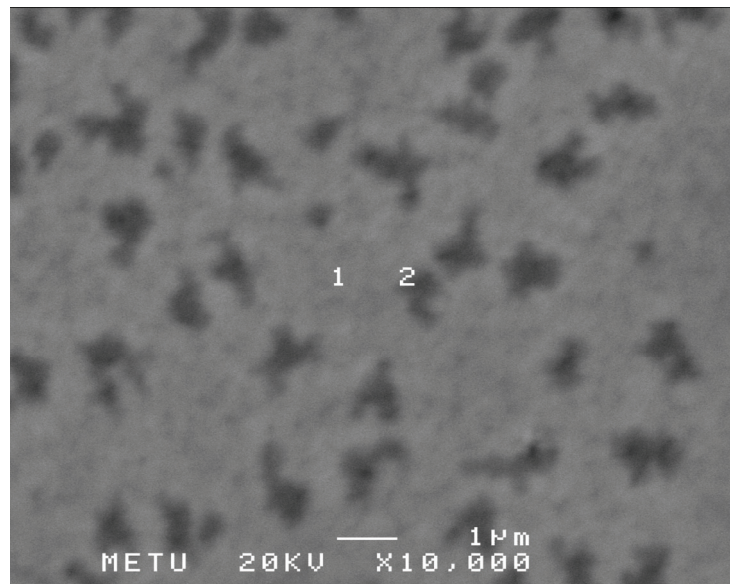


Fig.4.1. Micrograph of 450 nm PLZT thin film with composition of $\text{Pb}_{0.98}\text{La}_{0.02}(\text{Zr}_{0.4}\text{Ti}_{0.6})_{0.995}\text{O}_3$ sintered at 750°C for 30 min.

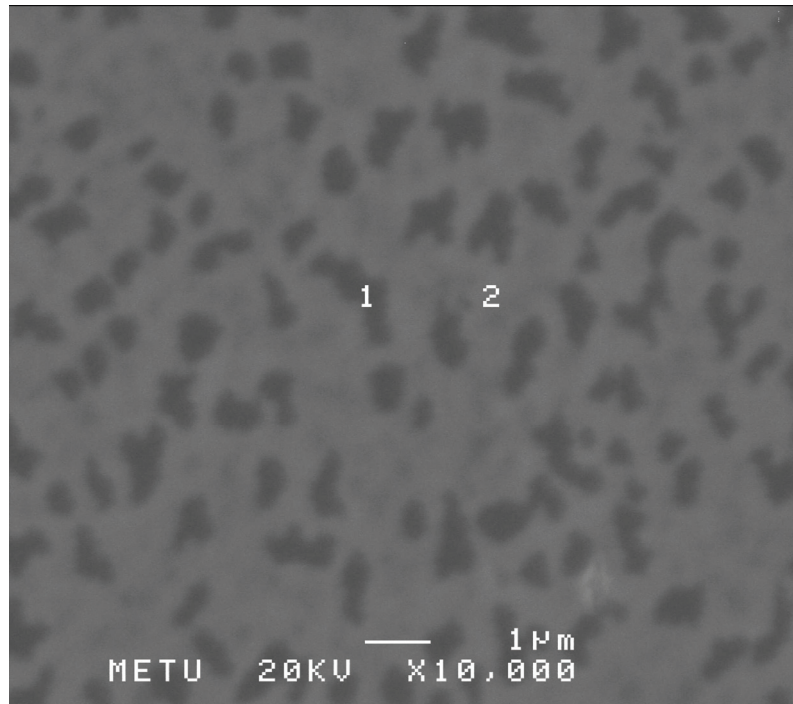


Fig. 4.2. Micrograph of 300 nm PLZT thin film with composition of $\text{Pb}_{0.98}\text{La}_{0.02}(\text{Zr}_{0.4}\text{Ti}_{0.6})_{0.995}\text{O}_3$ sintered at 700°C for 1 hr.

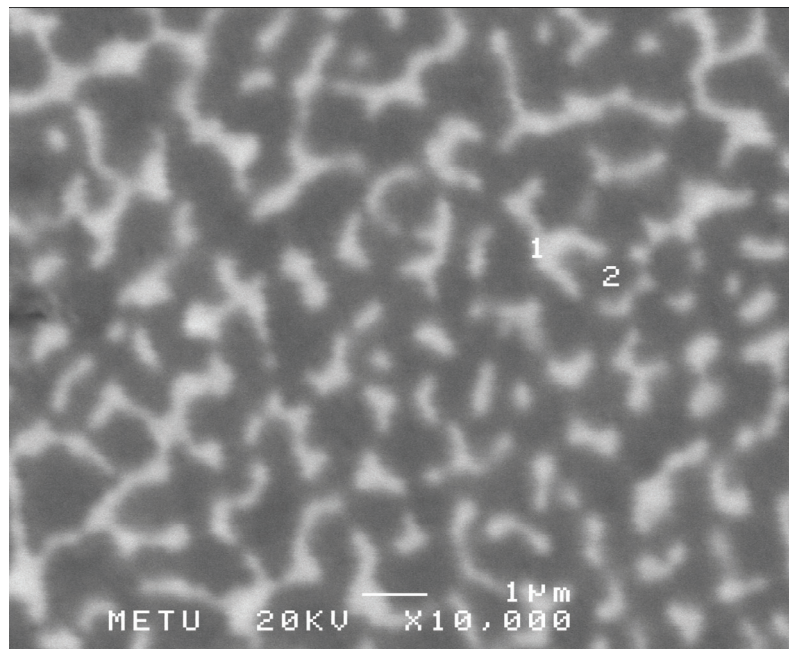


Fig. 4.3. Micrograph of 300 nm PLZT thin film with composition of $\text{Pb}_{0.98}\text{La}_{0.02}(\text{Zr}_{0.4}\text{Ti}_{0.6})_{0.995}\text{O}_3$ sintered at 800°C for 1 hr.

Figure 4.1, 4.2 and 4.3 show the microstructure generated by different heat treatments. It can be seen from the SEM pictures that there are mainly two phases present in the system. White background region, denoted by “1”, is the perovskite matrix and dark contrast region, denoted by “2”, is the second phase which are enriched in Pb. EDS investigations of the phase compositions show that dark regions separated by the grains are Pb-rich phases.

Dehydration of $\text{Pb}(\text{CH}_3\text{COO})_2 \cdot 3\text{H}_2\text{O}$ prior to mixing was not performed in this study to avoid the formation of multinuclear lead complexes [20]. The PLZT thin films having dark contrast Pb enriched regions showed very low capacitance values as well as low dielectric constants. Dehydration of lead acetate trihydrate was prevented by decreasing the heating temperature of the first solution to 90°C . Lead acetate trihydrate was dissolved in 2-methoxy ethanol at that temperature for 30 minutes. Then it was mixed with the second solution based on Ti and Zr. Both solutions were mixed for 30 minutes for refluxing. Figure 4.4 shows the final microstructure of the PLZT films without any dark regions.

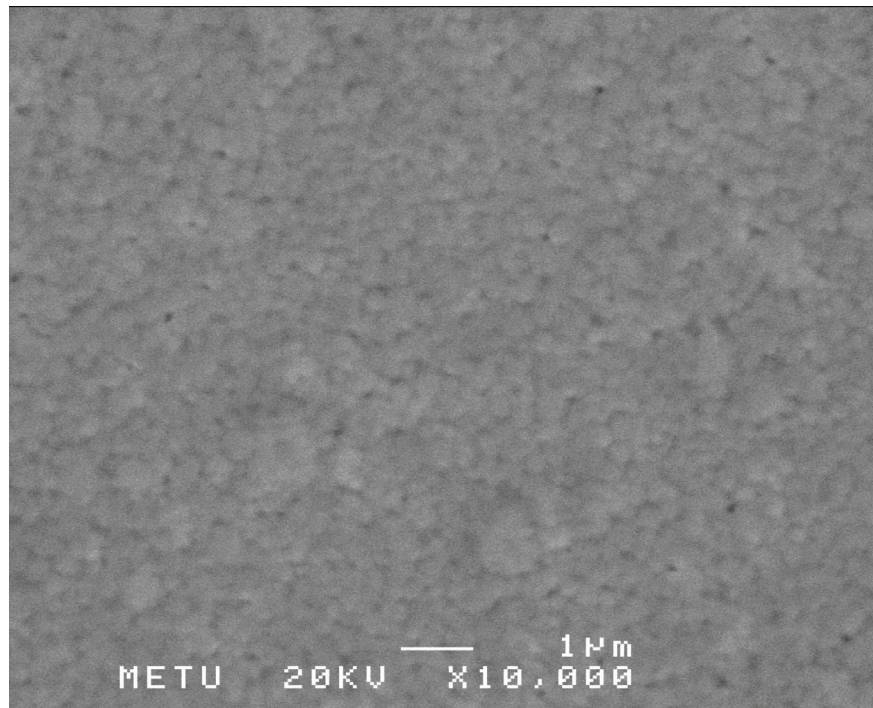


Fig. 4.4. Micrograph of 1.15 μm PLZT thin film with composition of $\text{Pb}_{0.96}\text{La}_{0.04}(\text{Zr}_{0.4}\text{Ti}_{0.6})_{0.99}\text{O}_3$ sintered at 750°C for 1 hr.

4.2. Crystalline Film Formation

X-ray diffraction studies were performed on the PLZT films deposited on Pt/Ti/SiO₂/Si substrates to optimize the perovskite crystallization temperature. The effect of temperature and annealing time on the perovskite formation have been investigated. Different type of annealing conditions were applied to PLZT thin films. In order to see the temperature effects, thin films were sintered at 600⁰C, 650⁰C, 700⁰C and 750⁰C. Furthermore, sintering time was considered as another parameter so that various sintering times 1 hour, 2 hours and 3 hours were applied to the samples. Combined effect of temperature and time on phases was investigated by using X-ray diffraction.

Figures 4.5a-b-c show the X-ray diffraction patterns of the PLZT annealed at 600⁰C for 1 hr, 2 hrs and 3 hrs. For the X-ray diffraction studies to optimize heat treatment process, the composition of Pb_{0.96}La_{0.04}(Zr_{0.4}Ti_{0.6})_{0.99}O₃ and Pb_{0.95}La_{0.05}(Zr_{0.52}Ti_{0.48})_{0.9875}O₃ were used and the same film thickness (four layers-600 nm) was obtained for all compositions. As it can be seen from the figures that the perovskite peaks emerged very clearly at 600⁰C. At that temperature, however, there was a small amount of pyrochlore phase TiO which was determined by according to the powder diffraction material ID card whose JCPDS file number was 12-754. The intensity of perovskite peaks increased as the sintering time was increased. Figures 4-5a-b-c shows the change in intensities of PLZT perovskite phases upon increase in sintering time. Figure 4-5d shows all these curves together in order to see effect of sintering time easily.

All the peaks corresponding to the perovskite phase at approximately $2\theta = 22^{\circ}$ (100), 31° (110), 38° (111), 45° (200) and 55° (211) emerged. The PLZT perovskite phase appeared at 600⁰C, and displayed a (111) peak, which was overlapped with a broad Pt(111) peak. Normally, PZT (0 %La) develops a 110 preferred texture [18].

The results of the X-ray diffraction presented above shows that both the lanthanum content and the bottom electrode type influence the

microstructure development of the PLZT thin films. The addition lanthanum appears to promote a polycrystalline structure with the predominance of (111) textures. These observations agree with the work of Es-Souni, et .al, where a 111 preferential texture of PLZT films deposited on (111)-Pt was reported [21].

A reaction between the Pt electrode and the thin film resulting at an interfacial layer of a Pb-Pt or Pt-Ti intermetallic phase has also been reported to influence film texture. Heterogeneous nucleation on highly oriented (111)-Pt electrodes has been investigated to favour (111) texture due to lattice matching [20]. Also, Tani et al, suggested that when the Ti adhesion layer formed Pt_3Ti at the interface, a (111) perovskite PLZT texture was obtained. Thus, PLZT crystallized in the (111) direction by heteroepitaxial nucleation and growth of Pt_3Ti crystallines with a cubic structure [22].

The results obtained in the present work suggest that first heterogeneous nucleation is expected to occur at the interface with (111)-Pt giving rise to preferential (111) orientation. Perovskite nuclei may form on discrete sites, e.g. inclusions, sites of compositional fluctuations, and grow consuming the amorphous phase giving rise to the rosette like morphology as given in Fig. 4.4.

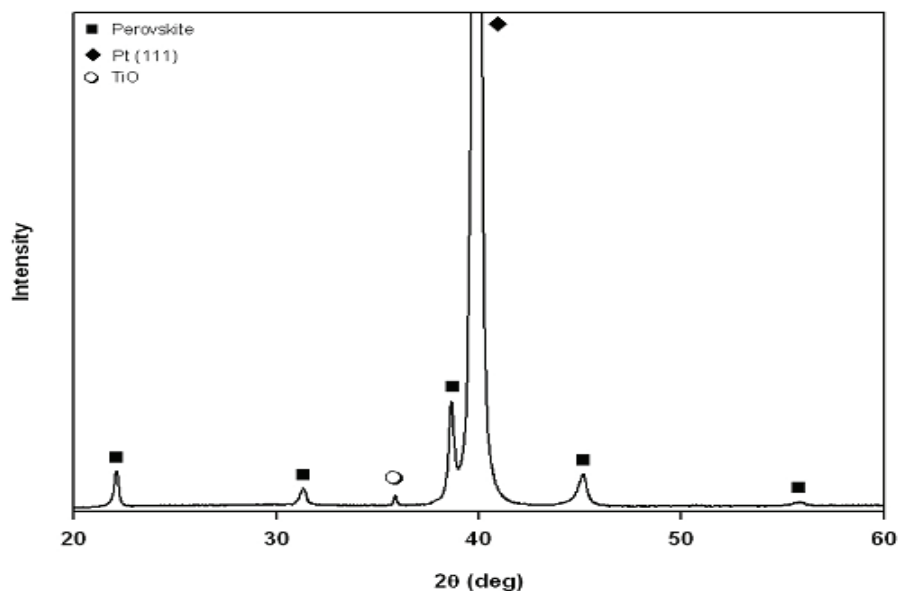


Fig. 4.5.(a) X-ray spectra of $Pb_{0.96}La_{0.04}(Zr_{0.4}Ti_{0.6})_{0.99}O_3$ thin film with thickness 600 nm and sintered at $600^{\circ}C$ for 1 hour. [sample no:44-1]

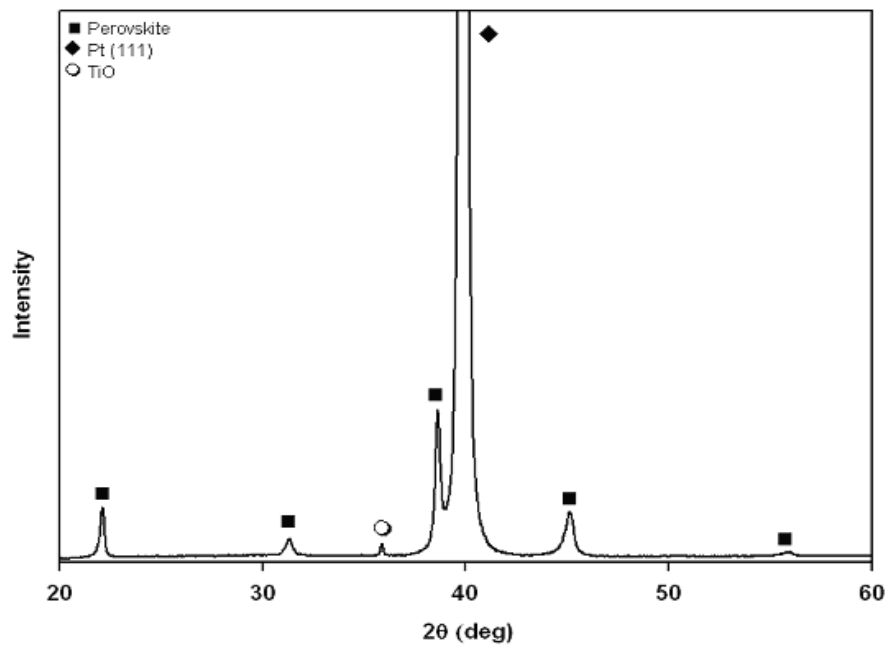


Fig. 4.5.(b) X-ray spectra of $\text{Pb}_{0.96}\text{La}_{0.04}(\text{Zr}_{0.4}\text{Ti}_{0.6})_{0.99}\text{O}_3$ thin film with thickness 600 nm and sintered at 600°C for 2 hours. [sample no:44-2]

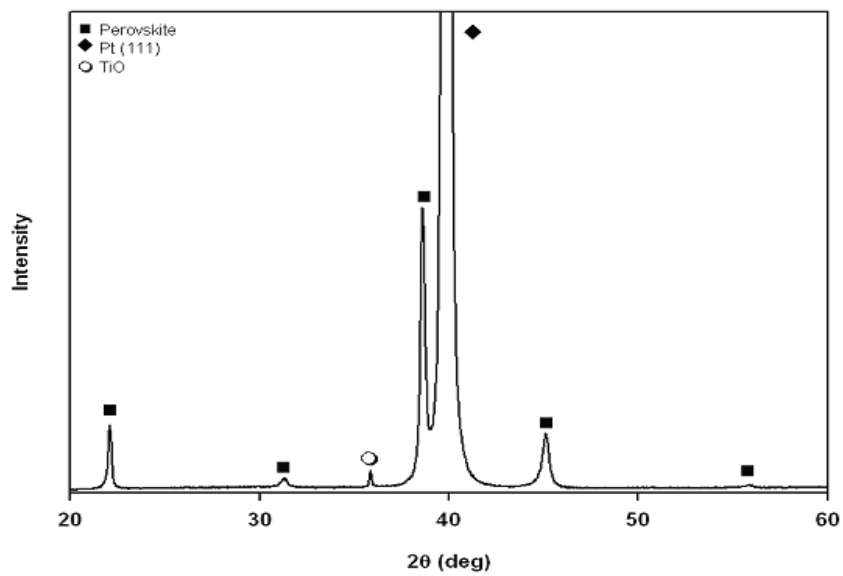


Fig. 4.5.(c) X-ray spectra of $\text{Pb}_{0.96}\text{La}_{0.04}(\text{Zr}_{0.4}\text{Ti}_{0.6})_{0.99}\text{O}_3$ thin film with thickness 600 nm and sintered at 600°C for 3 hours. [sample no:44-3]

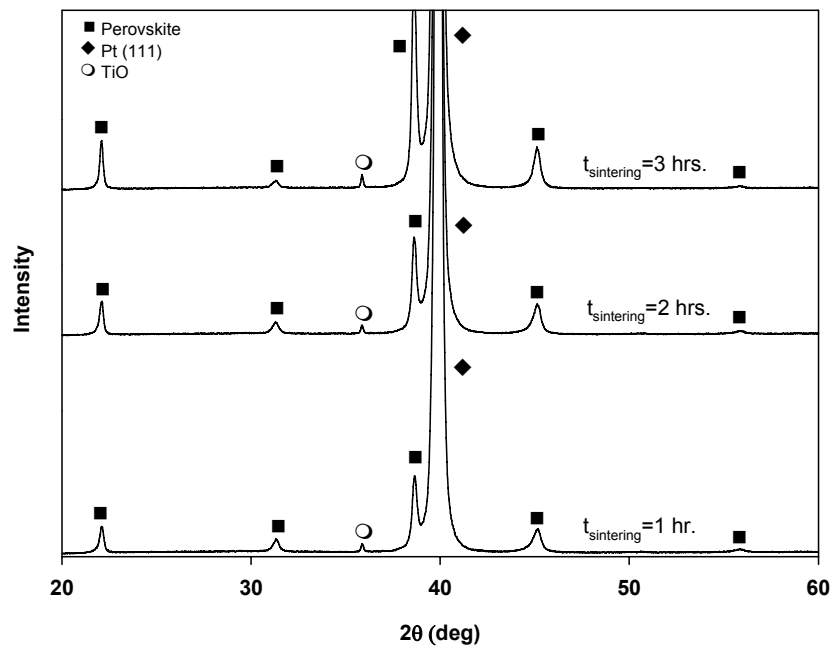


Fig. 4.5.(d) X-ray spectra of $\text{Pb}_{0.96}\text{La}_{0.04}(\text{Zr}_{0.4}\text{Ti}_{0.6})_{0.99}\text{O}_3$ thin film with thickness 600 nm and sintered at 600°C for 1-2-3 hours.

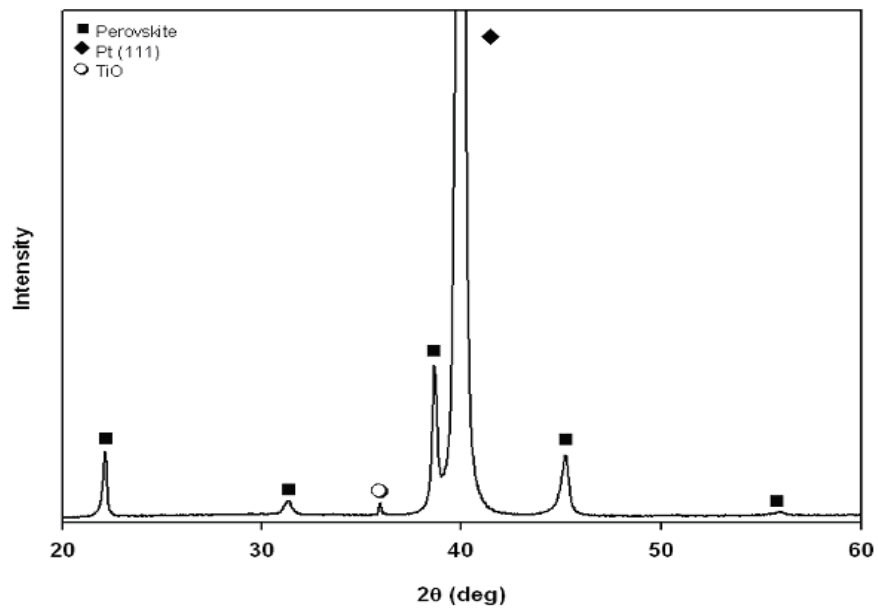


Fig. 4.6.(a) X-ray spectra of $\text{Pb}_{0.96}\text{La}_{0.04}(\text{Zr}_{0.4}\text{Ti}_{0.6})_{0.99}\text{O}_3$ thin film with thickness 600 nm and sintered at 700°C for 1 hour. [sample no:46-1]

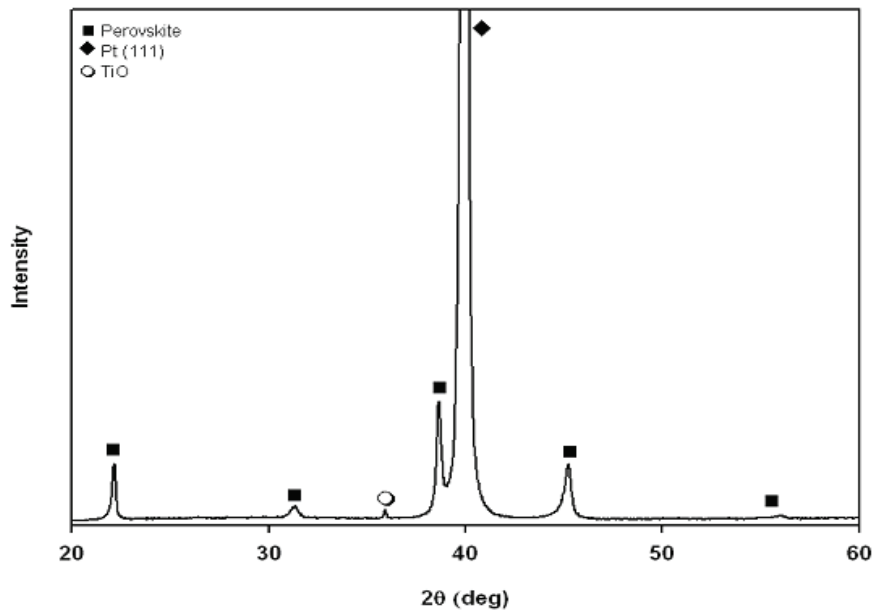


Fig. 4.6.(b) X-ray spectra of $\text{Pb}_{0.96}\text{La}_{0.04}(\text{Zr}_{0.4}\text{Ti}_{0.6})_{0.99}\text{O}_3$ thin film with thickness 600 nm and sintered at 700°C for 2 hours. [sample no:46-2]

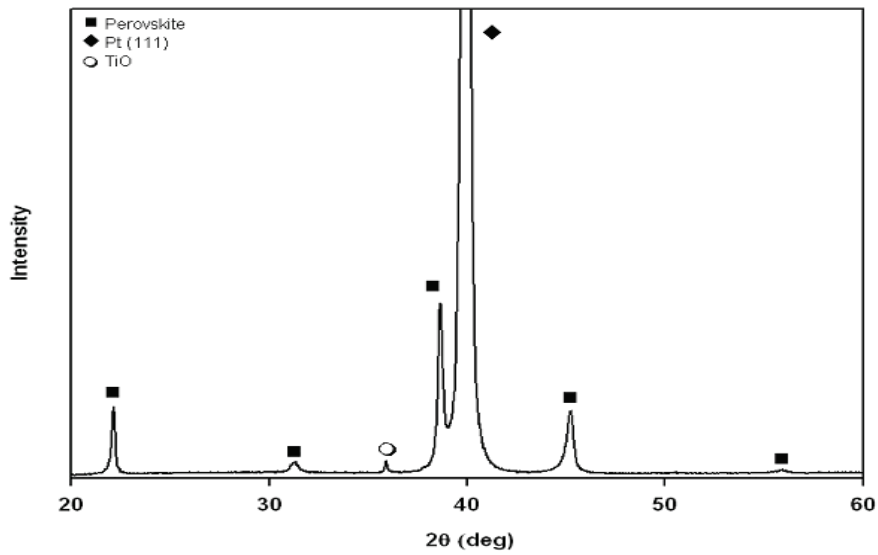


Fig. 4.6.(c) X-ray spectra of $\text{Pb}_{0.96}\text{La}_{0.04}(\text{Zr}_{0.4}\text{Ti}_{0.6})_{0.99}\text{O}_3$ thin film with thickness 600 nm and sintered at 700°C for 3 hours. [sample no:46-3]

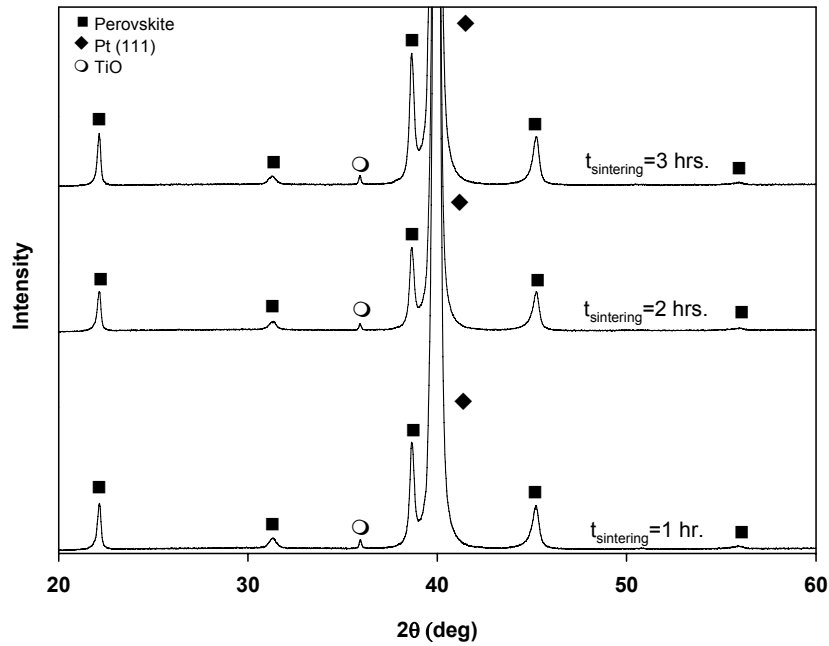


Fig. 4.6.(d) X-ray spectra of $\text{Pb}_{0.96}\text{La}_{0.04}(\text{Zr}_{0.4}\text{Ti}_{0.6})_{0.99}\text{O}_3$ thin film with thickness 600 nm and sintered at 700°C for 1-2-3 hours.

First heterogeneous nucleation is expected to occur at the interface with (111)-Pt giving rise to preferential (111) orientation. As crystallization proceeds, the amorphous/pyrochlore phase is expected to become progressively enriched with excess Pb which may lead to its destabilization and spontaneous crystallization of the perovskite with an orientation corresponding to the lowest nucleation barrier, i.e. (100) [21].

Figures 4.6a-b-c show that there is still pyrochlore remained in the system at 700°C for all sintering times. Increase of sintering times resulted only enhancement of perovskite intensity. Figure 4.6d shows all these curves together.

Heat treatments of the PLZT thin films with the composition $\text{Pb}_{0.95}\text{La}_{0.05}(\text{Zr}_{0.52}\text{Ti}_{0.48})_{0.9875}\text{O}_3$ were also performed to investigate the effects of temperature with a constant sintering time 3 hours. Figure 4.7a-b-c show the X-ray spectra of PLZT thin films sintered at different temperatures increasing from

600⁰C to 750⁰C for 3 hours. At 600⁰C there is a pyrochlore phase emerged at $2\theta = 31^{\circ}$, Ti₃O₅. The JCPDS file number of Ti₃O₅ is 9-309.

Figure 4.7d shows the X-Ray diffraction patterns of films sintered at 600⁰C, 700⁰C and 750⁰C for 3 hours together.

At the temperature of 600⁰C, intensities of perovskite phases are very small. Perovskite (111) phase starts emerging and overlappes with Pt(111) peak. As the temperature increased, the pyrochlore phase was disappeared and the system completely transformed into perovskite phase. All the films sintered at 750⁰C were perovskite phase with randomly oriented polycrystalline structure and no other intermediate phases such as pyrochlore were observed.

Effects of La element on X-ray results were also investigated. For this aim, Pb(Zr_{0.65}Ti_{0.35})O₃, Pb_{0.94}La_{0.06}(Zr_{0.65}Ti_{0.35})_{0.985}O₃ and Pb_{0.91}La_{0.09}(Zr_{0.65}Ti_{0.35})_{0.9775}O₃ compositions of thin films were prepared and their XRD spectra compared. Figures 4.8, 4.9 and 4.10 display the X-ray results of thin films with compositions Pb(Zr_{0.65}Ti_{0.35})O₃, Pb_{0.94}La_{0.06}(Zr_{0.65}Ti_{0.35})_{0.985}O₃ and Pb_{0.91}La_{0.09}(Zr_{0.65}Ti_{0.35})_{0.9775}O₃, respectively. As can be seen that intensity of the perovskite peaks (100), (110), (111) and (200) decreases while La content of the films increases. La substitution results in a substantial slow-down of the crystallization kinetics. It seems that La leads to the stabilization of the pyrochlore phase. In terms of chemical driving force, perovskite crystallization leads to Pb-depletion of the surrounding pyrochlore matrix. Due to the fact that the presence of La results in further Pb deficiency and since perovskite crystallization is controlled by the Pb stoichiometry, the chemical driving force for the perovskite crystallization is expected to be decreased thus leading to slower crystallization kinetics. Both diffusion impediment by the formation of cation vacancy-hole complexes and chemical stabilization of pyrochlore will shift the crystallization kinetics to higher temperatures and/or times [23].

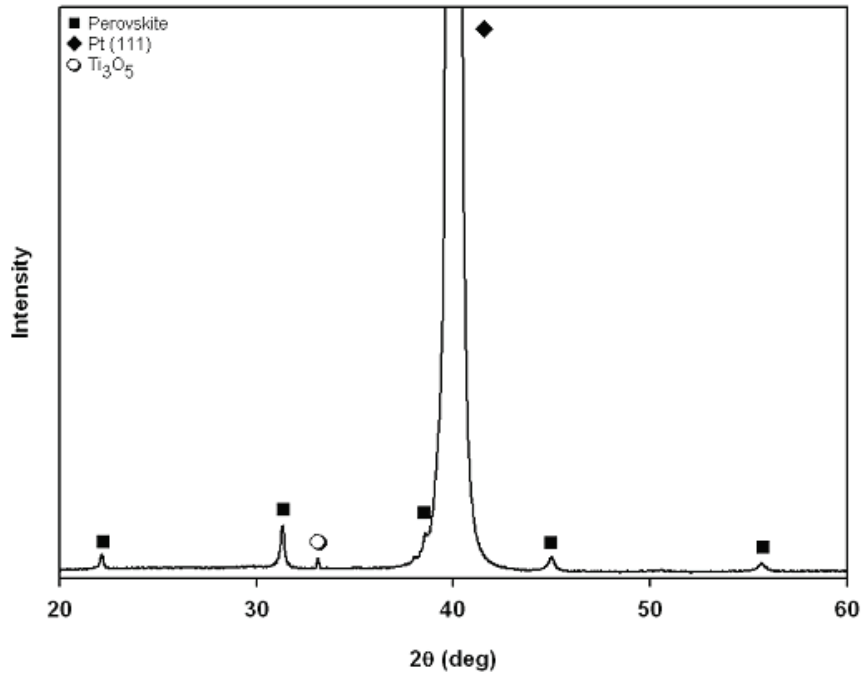


Fig. 4.7.(a) X-ray spectra of $Pb_{0.95}La_{0.05}(Zr_{0.52}Ti_{0.48})_{0.9875}O_3$ thin film with thickness 600 nm and sintered at $600^\circ C$ for 3 hours. [sample no:63-3]

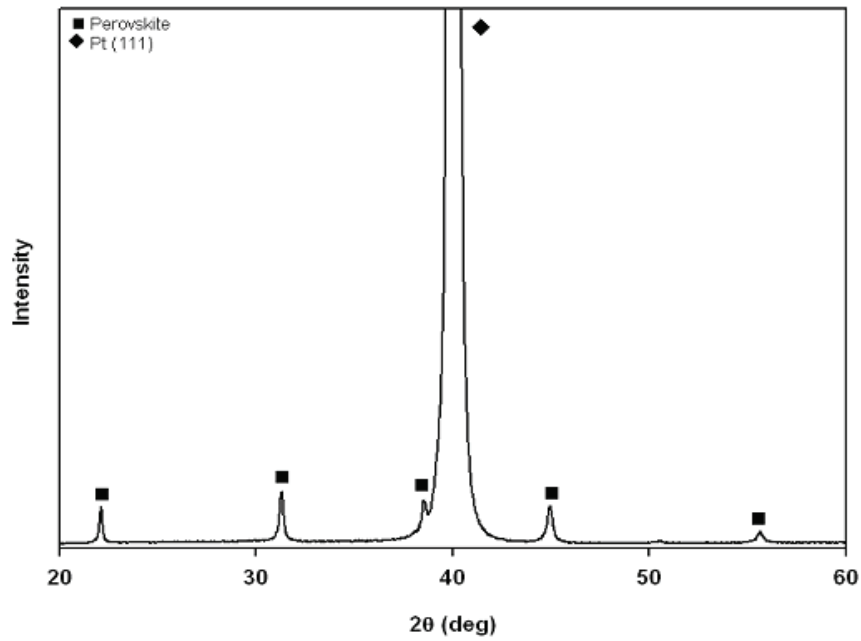


Fig. 4.7.(b) X-ray spectra of $Pb_{0.95}La_{0.05}(Zr_{0.52}Ti_{0.48})_{0.9875}O_3$ thin film with thickness 600 nm and sintered at $700^\circ C$ for 3 hours. [sample no:62-3]

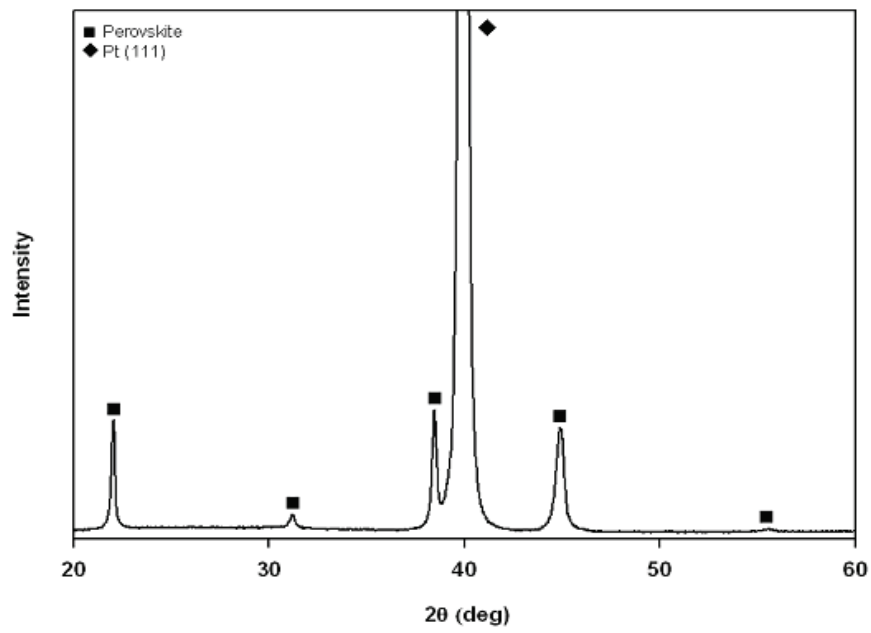


Fig. 4.7.(c) X-ray spectra of $\text{Pb}_{0.95}\text{La}_{0.05}(\text{Zr}_{0.52}\text{Ti}_{0.48})_{0.9875}\text{O}_3$ thin film with thickness 600 nm and sintered at 750°C for 3 hours. [sample no:49-3]

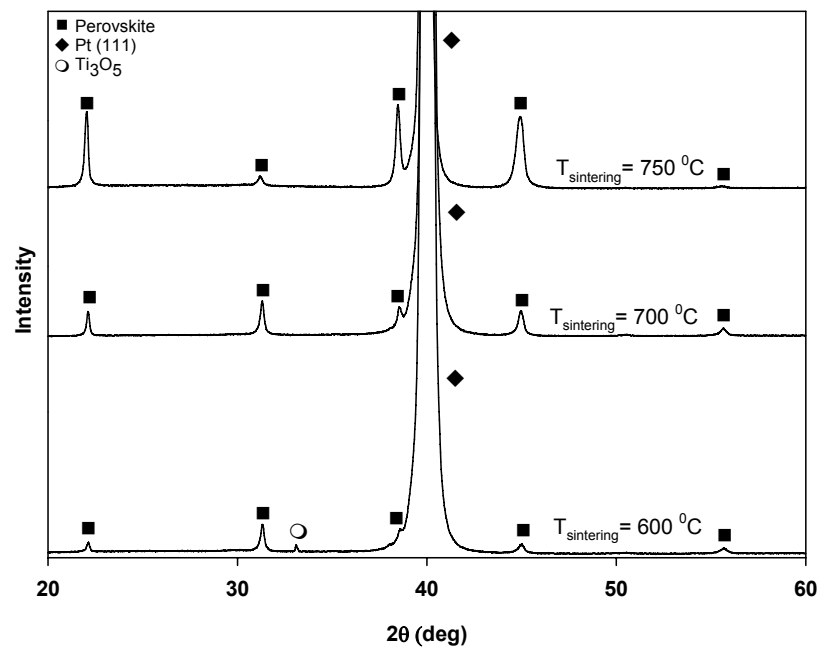


Fig. 4.7.(d) X-ray spectra of $\text{Pb}_{0.95}\text{La}_{0.05}(\text{Zr}_{0.52}\text{Ti}_{0.48})_{0.9875}\text{O}_3$ thin film with thickness 600 nm and sintered at 600°C - 700°C - 750°C for 3 hours.

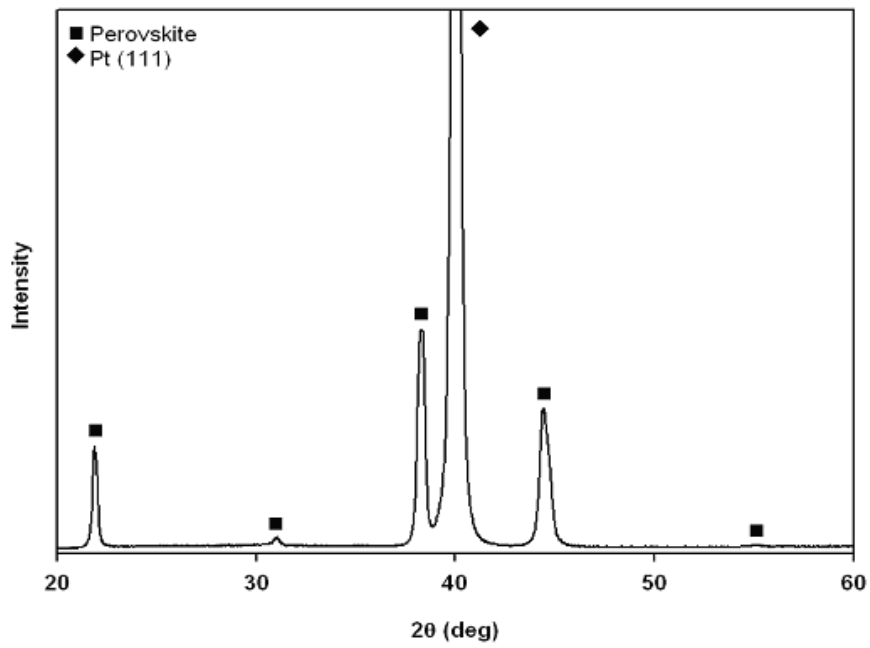


Fig. 4.8. X-ray spectra of $\text{Pb}(\text{Zr}_{0.65}\text{Ti}_{0.35})\text{O}_3$ thin film with thickness 700 nm and sintered at 750°C for 3 hours. [sample no:50-3]

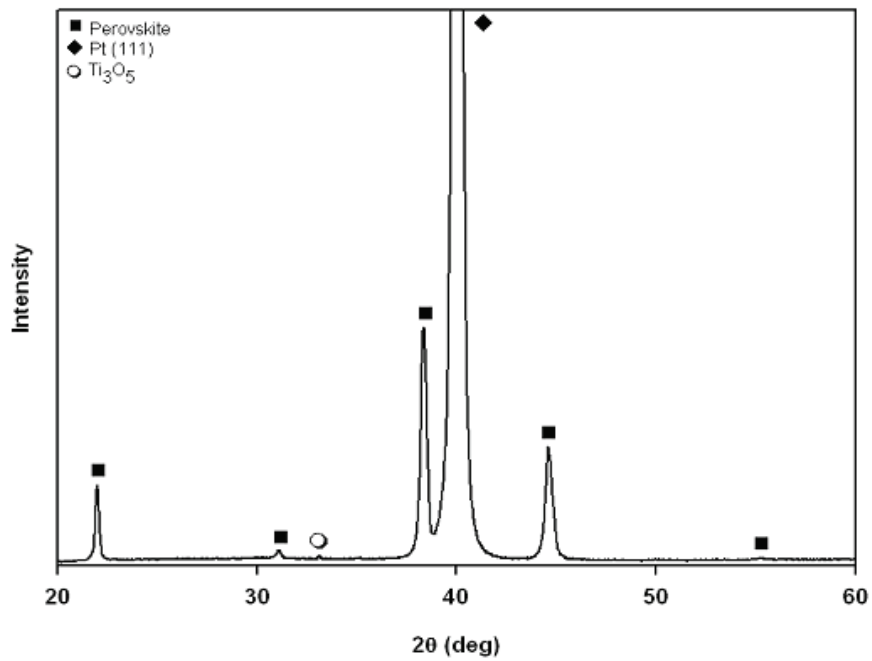


Fig. 4.9. X-ray spectra of $\text{Pb}_{0.94}\text{La}_{0.06}(\text{Zr}_{0.65}\text{Ti}_{0.35})_{0.985}\text{O}_3$ thin film with thickness 700 nm and sintered at 750°C for 3 hours. [sample no:51-3]

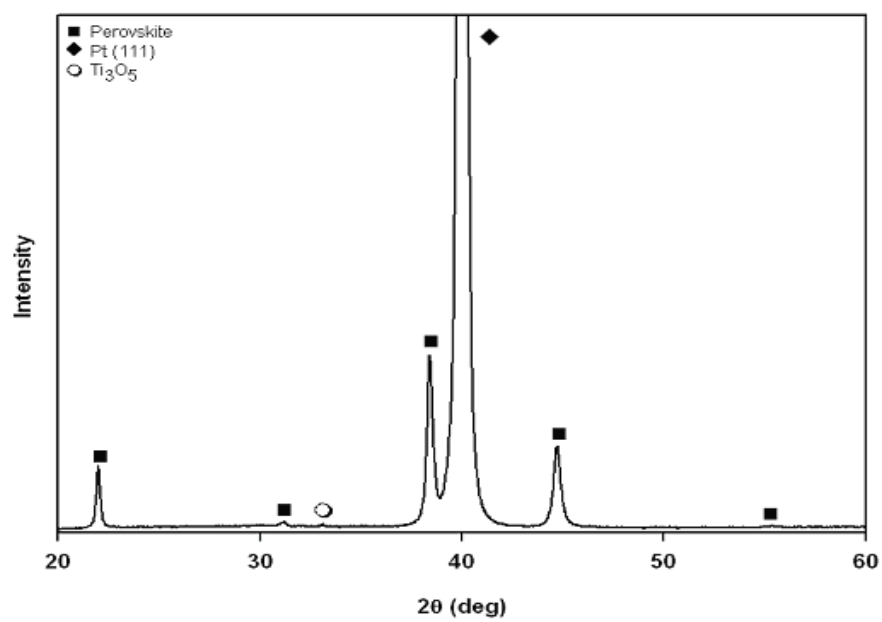


Fig. 4.10. X-ray spectra of $\text{Pb}_{0.91}\text{La}_{0.09}(\text{Zr}_{0.65}\text{Ti}_{0.35})_{0.9775}\text{O}_3$ thin film with thickness 700 nm and sintered at 750°C for 3 hours. [sample no:52-3]

4.3. Thermal Analysis of the PLZT Thin Films

In order to determine the best conditions for pyrolysis and annealing to obtain crack-free PLZT thin films, thermal analysis was performed.

The differential thermal analysis (DTA) was performed to investigate the exothermic thermodynamic reactions which occur during heating of the PLZT powders. Furthermore, thermogravimetry (TG) curves were drawn to see the weight losses upon increasing temperature.

Figure 4.11 and 4.12 show the DTA-TG curve of the PLZT gel, respectively, obtained from room temperature up to 900⁰C using a heating rate of 3⁰C/min. In order to get PLZT powder, solution was dried at 100⁰C for 8 hours. In the TGA curves, three different weight loss regions were observed. Initial loss of approximately 1.2% between 30 and 160⁰C corresponds to the removal of solvent and/or moisture present in the gel. The second weight loss region (19.3% wt. loss) was observed in the range 160-400⁰C and this may be due to the result of the decomposition of light organics and acetates. The exothermic peak at 310⁰C found in this range (DTA) supports this behavior. The last weight loss region (3.6% wt. loss) in the TGA was in the temperature range 400-600⁰C and is due to the decomposition of organic compounds and the formation of inorganic ceramic phase. The exothermic peak at 470⁰C in the DTA curve can be attributed to this behavior. And the small exothermic peak at 600⁰C can be correlated to the phase transition of PLZT, because not much weight loss could be observed in the TG curve. On the basis of this observation, it can be concluded that crystallization of PLZT powder starts at 600⁰C and the perovskite structure is established above 600⁰C. Further increase in the temperature or in the heating time will only promote the perovskite crystallization, as TGA did not show any weight loss after 600⁰C.

Because of these results obtained from DTA-TG curves, pyrolysis temperature was selected as 450⁰C and the annealing temperature was chosen at least 600⁰C for the perovskite formation.

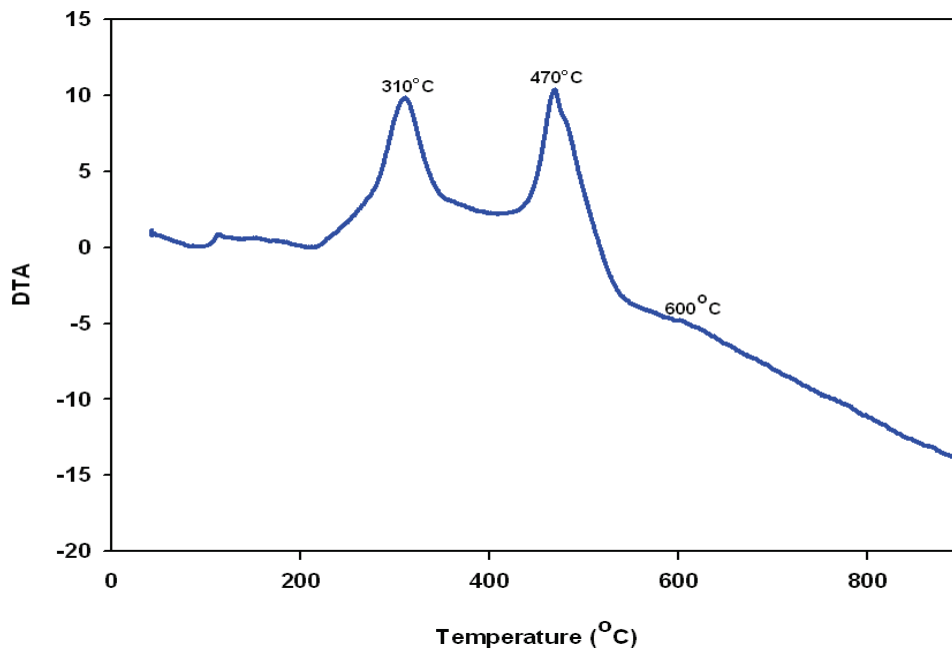


Fig. 4.11. Differential thermal analysis (DTA) curve of PLZT gel with composition of $\text{Pb}_{0.92}\text{La}_{0.08}(\text{Zr}_{0.65}\text{Ti}_{0.35})_{0.98}\text{O}_3$

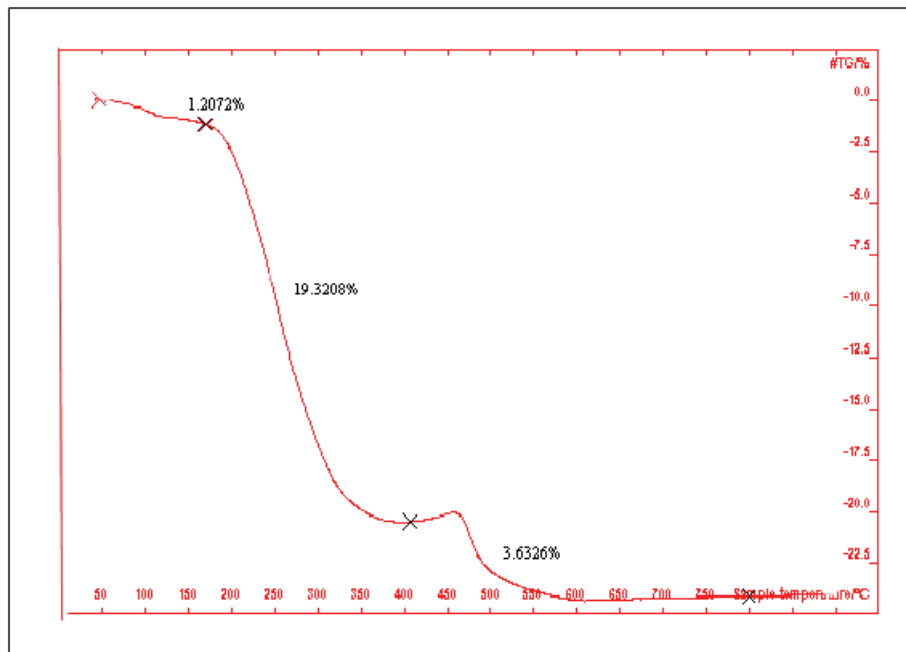


Fig. 4.12. Thermogravimetry (TG) curve of PLZT gel with composition of $\text{Pb}_{0.92}\text{La}_{0.08}(\text{Zr}_{0.65}\text{Ti}_{0.35})_{0.98}\text{O}_3$

4.4. Composition and Morphology of the PLZT Films

The composition and morphology of the PLZT thin films were investigated by Scanning Electron Microscope SEM/EDS analysis. The results of these analysis showed that PLZT films were smooth, uniform and crack-free. As stated in the previous chapters that there are 11 compositions worked in this study. Table 4.2 shows EDS analysis of PLZT thin film compositions :

- $\text{Pb}_{0.96}\text{La}_{0.04}(\text{Zr}_{0.4}\text{Ti}_{0.6})_{0.99}\text{O}_3$
- $\text{Pb}_{0.91}\text{La}_{0.09}(\text{Zr}_{0.65}\text{Ti}_{0.35})_{0.9975}\text{O}_3$
- $\text{Pb}_{0.9}\text{La}_{0.1}(\text{Zr}_{0.4}\text{Ti}_{0.6})_{0.975}\text{O}_3$
- $\text{Pb}_{0.95}\text{La}_{0.05}(\text{Zr}_{0.52}\text{Ti}_{0.48})_{0.9875}\text{O}_3$

SEM observations indicated that the PLZT films morphologies were smooth and free from cracks which may be produced by the stresses generated during the conversion of the gel coating to a dense ceramic, and because of thermal expansion mismatches between film and substrate.

The cross-section and surface of PLZT thin film were examined by SEM to measure the thickness and adhesion between film and Pt/Ti/SiO₂/Si substrate. Thickness of the films were measured in the range of 300 nm and approximately 1.1 μm. For 0.4M PLZT solution and one layer spin coating (3000 rpm-30 sec), it was reached 300 nm film thickness. 2 layer thickness was about 450 nm, 4 layers-600 nm, 6 layers-700 nm and 8 layers-1.14 μm.

EDS analysis was done by using PLZT powders which was produced by drying method at 100 °C for 8 hours. It shows the quantities of elements of Pb, Zr, Ti and La present in the film. EDS analysis of composition $\text{Pb}_{0.96}\text{La}_{0.04}(\text{Zr}_{0.4}\text{Ti}_{0.6})_{0.99}\text{O}_3$ was performed by preparing 20 μm thick film to eliminate the peaks of the substrate. Figure 4.13 shows the thick film which was produced to obtain EDS analysis. It can be seen that surface of the film has cracks which did not affect the EDS investigations.

Table 4.2. EDS analysis of PLZT thin films with different compositions from different regions of PLZT phase diagram.

Prepared Composition	Thickness	Heat Treatment	Pb (atom%)	Zr(atom%)	Ti(atom%)	La(atom%)	Pb/La/Zr/Ti by EDS Analysis
$\text{Pb}_{0.96}\text{La}_{0.04}(\text{Zr}_{0.4}\text{Ti}_{0.6})_{0.99}\text{O}_3$	20 μm	700 $^{\circ}\text{C}$	48.21	20.05	30.04	1.7	0.96/0.034/0.4/0.6
$\text{Pb}_{0.91}\text{La}_{0.09}(\text{Zr}_{0.65}\text{Ti}_{0.35})_{0.9975}\text{O}_3$	powder	Dried at 100 $^{\circ}\text{C}$	46.33	31.89	17.38	4.39	0.91/0.086/0.66/0.34
$\text{Pb}_{0.9}\text{La}_{0.1}(\text{Zr}_{0.4}\text{Ti}_{0.6})_{0.975}\text{O}_3$	powder	Dried at 100 $^{\circ}\text{C}$	47.21	20.38	27.43	4.98	0.9/0.094/0.388/0.52
$\text{Pb}_{0.95}\text{La}_{0.05}(\text{Zr}_{0.52}\text{Ti}_{0.48})_{0.9875}\text{O}_3$	powder	Dried at 100 $^{\circ}\text{C}$	48.65	26.24	22.48	2.63	0.95/0.05/0.51/0.438

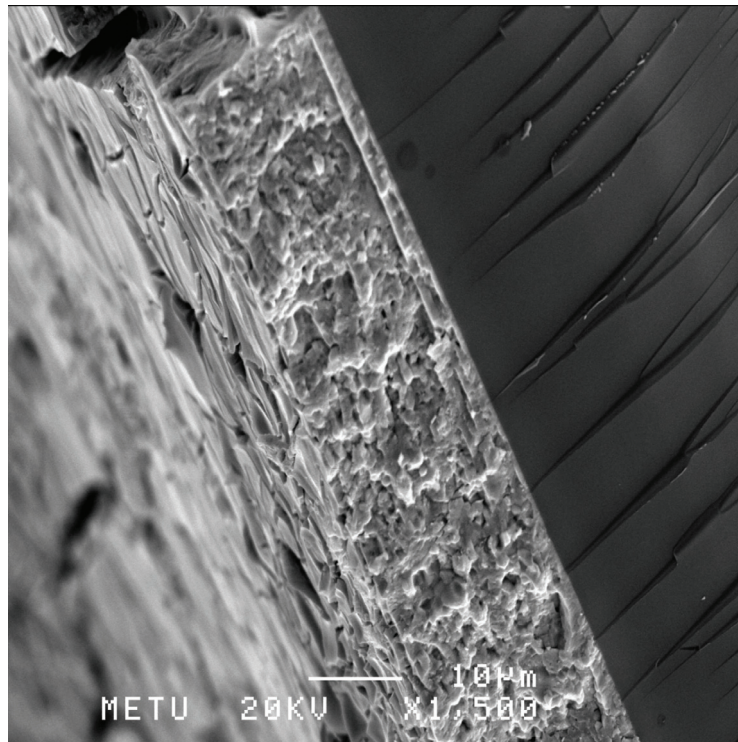


Fig. 4.13. The cross-section of PLZT film with a thickness 20 μm and composition $\text{Pb}_{0.96}\text{La}_{0.04}(\text{Zr}_{0.4}\text{Ti}_{0.6})_{0.99}\text{O}_3$, annealed at 700 °C for 1 hr produced only for EDS analysis.

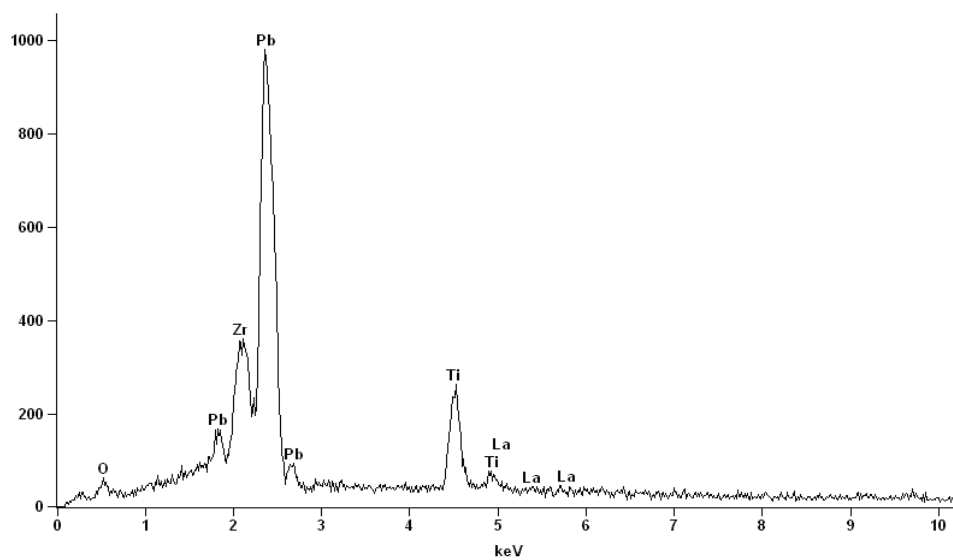


Fig. 4.14. EDS analysis of the film shown in Fig. 4.13.

EDS analysis of powders obtained from precursors was also examined and it was investigated that the ratio of elements in the chemical composition formula was approximately same with the ratio of atomic values obtained from EDS. Figure 4.15-16-17 shows the EDS analysis of PLZT powders having different compositions.

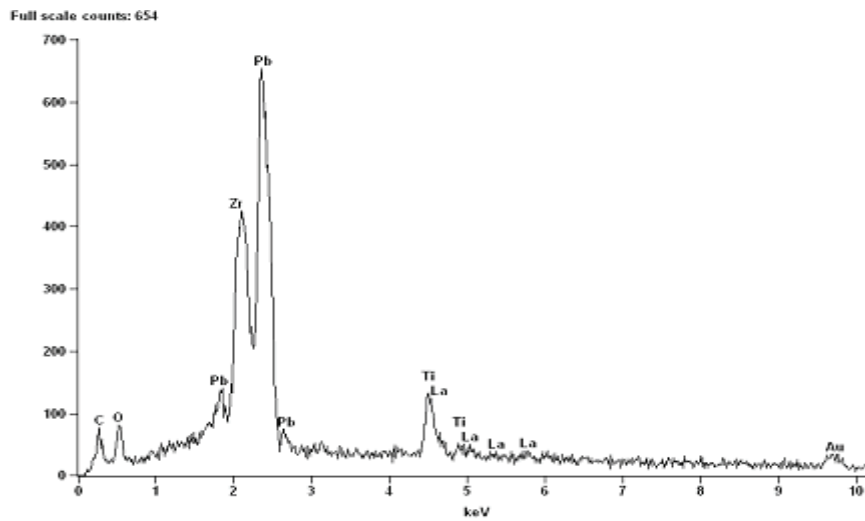


Fig. 4.15. EDS spectra of $\text{Pb}_{0.91}\text{La}_{0.09}(\text{Zr}_{0.65}\text{Ti}_{0.35})_{0.9975}\text{O}_3$ powder dried at 100°C .

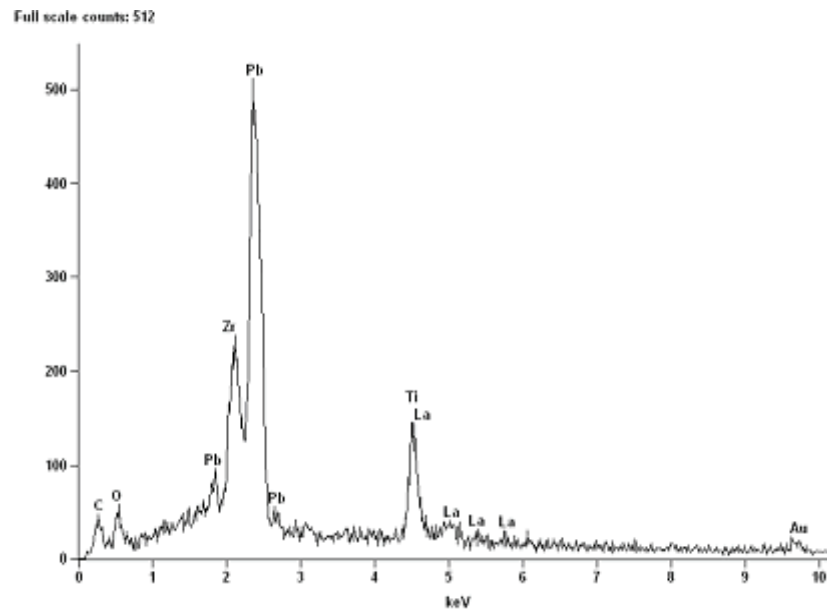


Fig. 4.16. EDS spectra of $\text{Pb}_{0.9}\text{La}_{0.1}(\text{Zr}_{0.4}\text{Ti}_{0.6})_{0.975}\text{O}_3$ powder dried at 100°C .

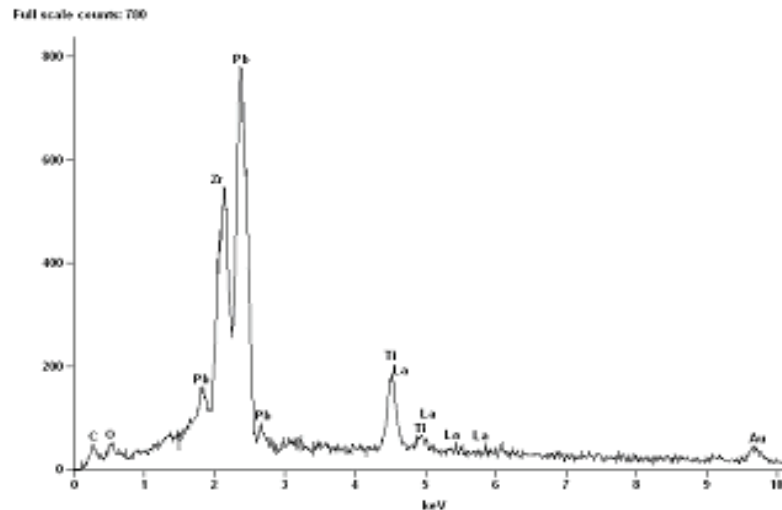


Fig. 4.17. EDS spectra of $\text{Pb}_{0.95}\text{La}_{0.05}(\text{Zr}_{0.52}\text{Ti}_{0.48})_{0.9875}\text{O}_3$ powder dried at $100\text{ }^\circ\text{C}$.

SEM photographs of PLZT thin films show that they are well-adhered, smooth and crack-free films on Pt/Ti/SiO₂/Si substrates whose cross-section and surface views are shown in Fig 4.18 and Fig 4.19a-b. They are 700 nm thick achieved by repeating 6 coating cycles followed by drying and annealing processes. Fig 4.19a-b shows the surface image of the films that are very smooth and free from cracks.

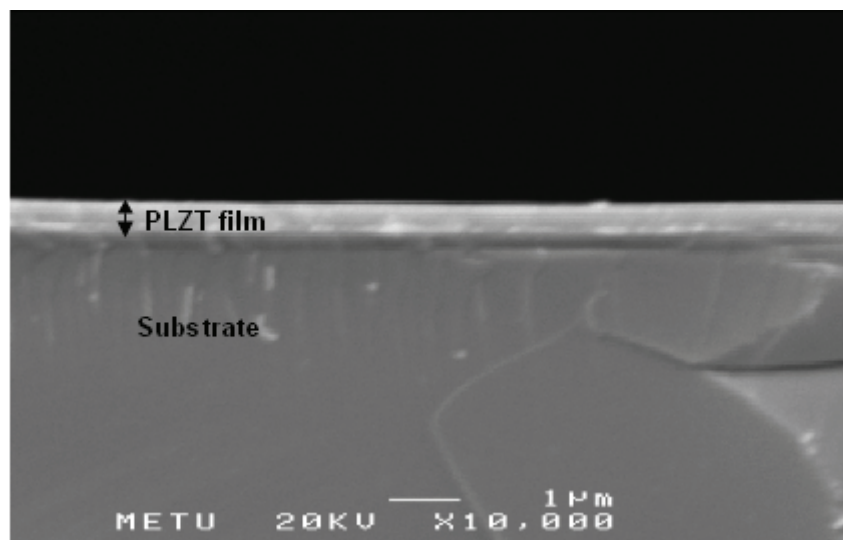
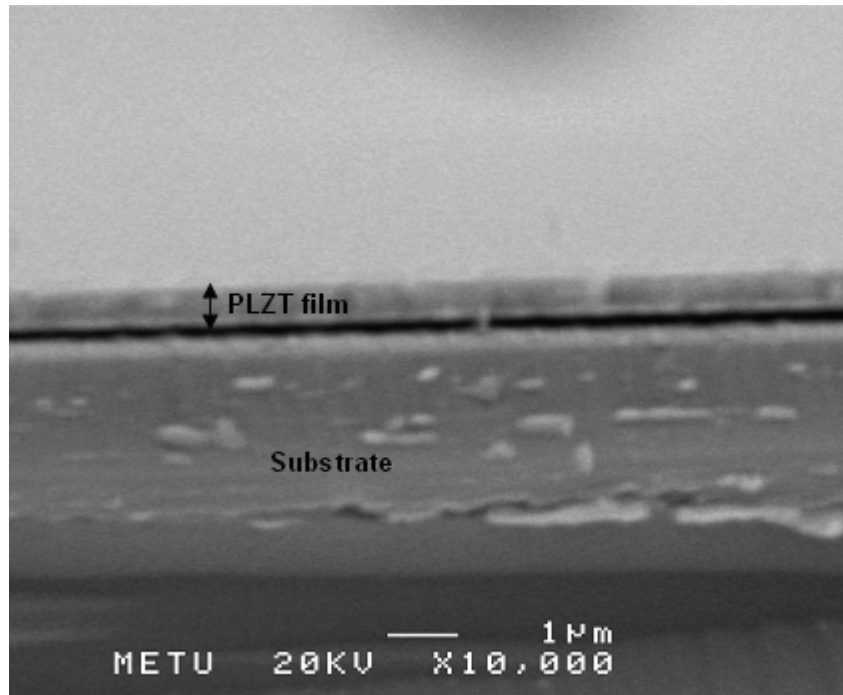
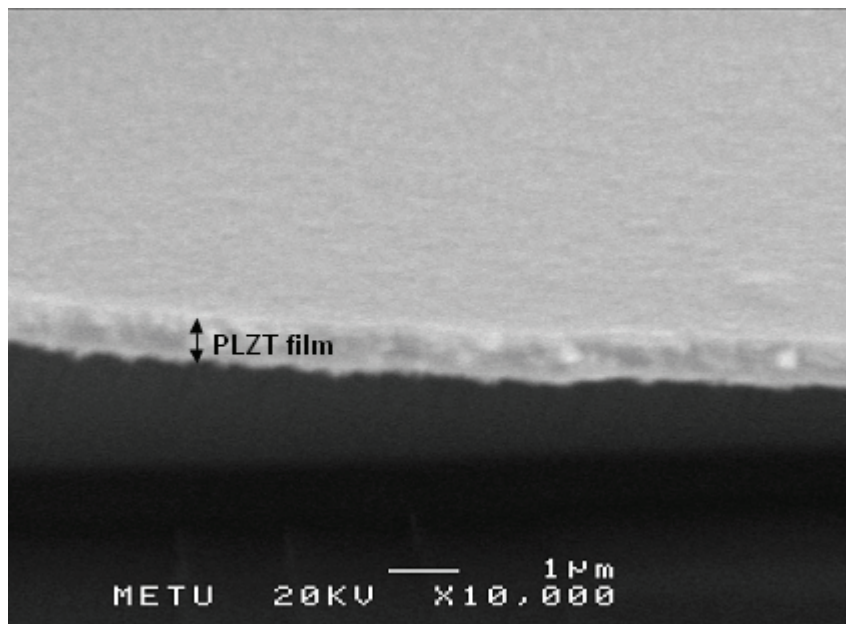


Fig. 4.18. Cross sectional view of $\text{Pb}_{0.94}\text{La}_{0.06}(\text{Zr}_{0.65}\text{Ti}_{0.35})_{0.985}\text{O}_3$ -700 nm thick PLZT film annealed at $750\text{ }^\circ\text{C}$ for 3 hours.



(a)



(b)

Fig. 4.19a-b. Surface view of $\text{Pb}_{0.96}\text{La}_{0.04}(\text{Zr}_{0.4}\text{Ti}_{0.6})_{0.99}\text{O}_3$ -700 nm thick PLZT film annealed at 750 °C for 3 hours.

The PLZT films having a thickness greater than 1 μm were also produced. The electrical characterization was not performed on these films but surface characterization was carried out. Also, no cracks were observed on the surfaces on these films. Figure 4.20 shows the PLZT film with a thickness of 1.14 μm , annealed at 750 $^{\circ}\text{C}$ for 1 hour.

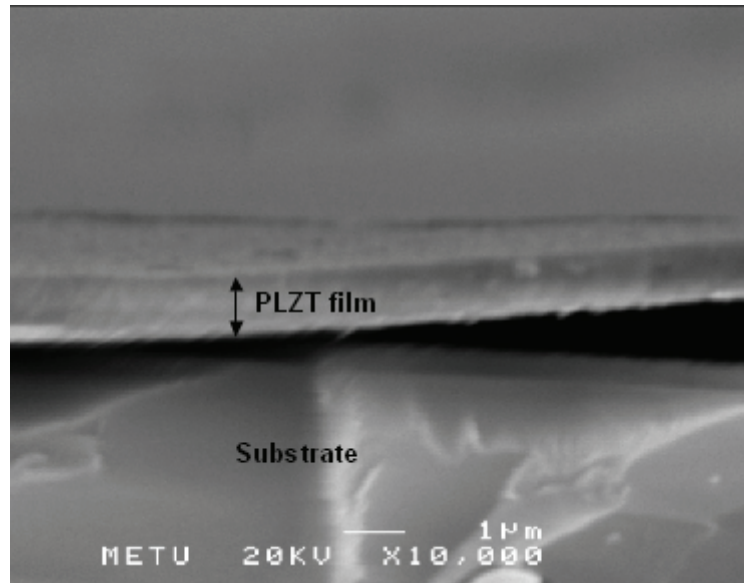


Fig. 4.20. Cross sectional image of 1.14 μm thick PLZT film on Pt/Ti/SiO₂/Si substrate with composition of $\text{Pb}_{0.96}\text{La}_{0.04}(\text{Zr}_{0.4}\text{Ti}_{0.6})_{0.99}\text{O}_3$, annealed at 700 $^{\circ}\text{C}$ for 1 hr.

In this study, average grain size could not be determined by SEM because they are too small to be observed by maximum magnification of the SEM used. Instead of SEM, grain size could be estimated by Scherrer's Formula, which is a technique based on measuring the full width of x-ray diffraction peaks at the half maximum height of the peak.

Scherrer's Formula

$$t = \frac{0.94 * \lambda}{B * \cos \theta} \quad \text{Eq. [4.1]}$$

where, t is the average grain size, λ is the wavelength of radiation of the x-ray beam used, B is the width of the peak at the half of the maximum intensity (in radians) and θ is the half of the diffraction angle 2θ [24]. Maximum intensity peak in the X-ray spectra of PLZT thin films is the perovskite (111) peak.

Temperature and La content were considered as the two effective parameters in the development of grain size. In order to investigate the temperature effect, four different heat treatments applied to these films. PLZT thin films were annealed at 600 °C, 650 °C, 700 °C and 750 °C. Table 4.3 shows the grain size of the films annealed at these temperatures.

Table 4.3. The grain sizes of PLZT thin films sintered at different temperatures for 3 hours sintering time for all samples.

Composition	Sintering temperature	Grain Size (nm)
$\text{Pb}_{0.96}\text{La}_{0.04}(\text{Zr}_{0.4}\text{Ti}_{0.6})_{0.99}\text{O}_3$	600 °C	6.6
$\text{Pb}_{0.96}\text{La}_{0.04}(\text{Zr}_{0.4}\text{Ti}_{0.6})_{0.99}\text{O}_3$	650 °C	8.3
$\text{Pb}_{0.96}\text{La}_{0.04}(\text{Zr}_{0.4}\text{Ti}_{0.6})_{0.99}\text{O}_3$	700 °C	9.5
$\text{Pb}_{0.96}\text{La}_{0.04}(\text{Zr}_{0.4}\text{Ti}_{0.6})_{0.99}\text{O}_3$	750 °C	16.6

The grain sizes of PLZT thin films were also calculated as a function of La content. In order to perform this, sintering temperature was fixed to 750 °C and La content was increased. Table 4.4 displays the grain sizes of PLZT thin films with different compositions, annealed at 750 °C for 3 hours.

Table 4.4. The grain sizes of PLZT thin films having different compositions sintered at the same temperature.

Composition	Sintering temperature	Grain Size (nm)
$\text{Pb}(\text{Zr}_{0.65}\text{Ti}_{0.35})\text{O}_3$	750 °C	3.3
$\text{Pb}_{0.94}\text{La}_{0.06}(\text{Zr}_{0.65}\text{Ti}_{0.35})_{0.985}\text{O}_3$	750 °C	4.4
$\text{Pb}_{0.91}\text{La}_{0.09}(\text{Zr}_{0.65}\text{Ti}_{0.35})_{0.9775}\text{O}_3$	750 °C	5.1
$\text{Pb}(\text{Zr}_{0.52}\text{Ti}_{0.48})\text{O}_3$	750 °C	5.5
$\text{Pb}_{0.95}\text{La}_{0.05}(\text{Zr}_{0.52}\text{Ti}_{0.48})_{0.9875}\text{O}_3$	750 °C	7.4

4.5. Dielectric Properties of PLZT Thin Films

The dielectric properties of PLZT thin films such as dielectric constant and tangent loss ($\tan\delta$) were measured by HP 4194A impedance-gain phase analyser. These measurements were performed with the change of temperature and composition.

The variation of capacitance and dielectric constants of the PLZT thin films with the change of AC frequencies were investigated as a function of temperature shown in Figure 4.21 and Figure 4.22.

Dielectric constants and tangent losses of the films were measured in the frequency range of 1kHz-1MHz with an oscillation voltage of 0.5V. Table 4.5 shows the dielectric constant values and tangent loss values of PLZT thin films at 1kHz and 1MHz.

Dielectric constants (K) of the films were calculated by using the following formula :

$$C = K * \epsilon_0 * \frac{A}{d}$$

where C = capacitance of the film,
 ϵ_0 = permittivity of vacuum,
 A = electrode area,
 d = film thickness.

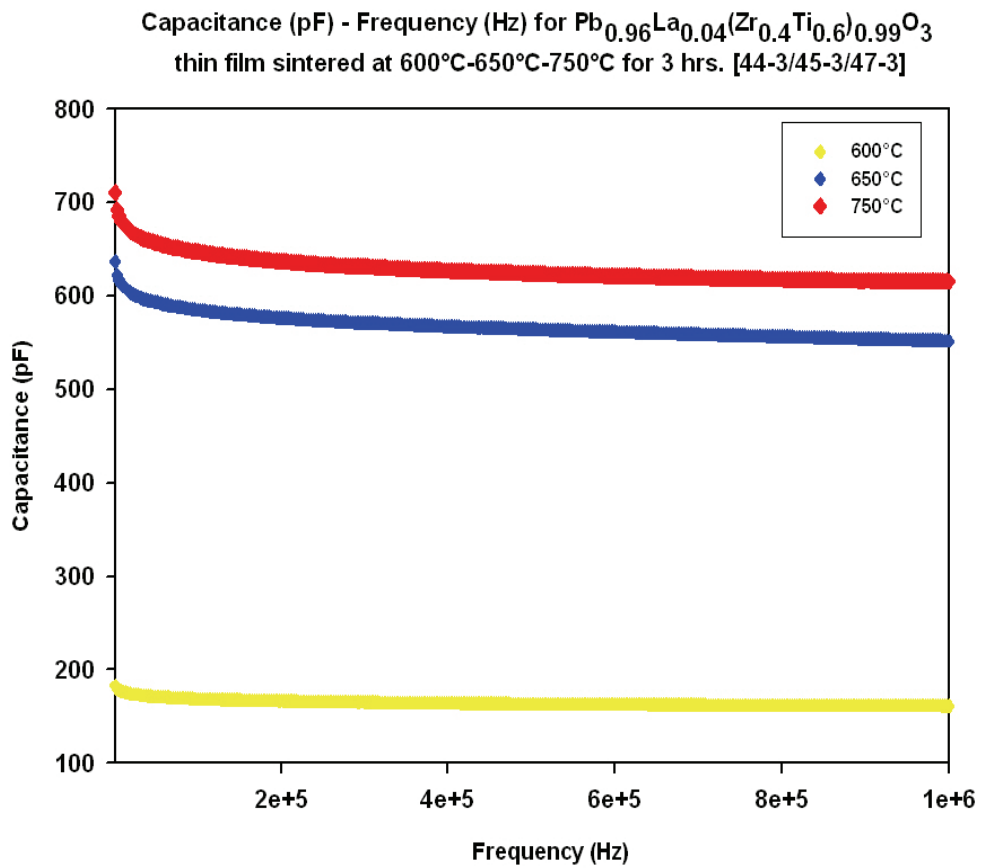


Fig 4.21. Change of capacitance values of thin films with changing frequencies with respect to different sintering temperatures.

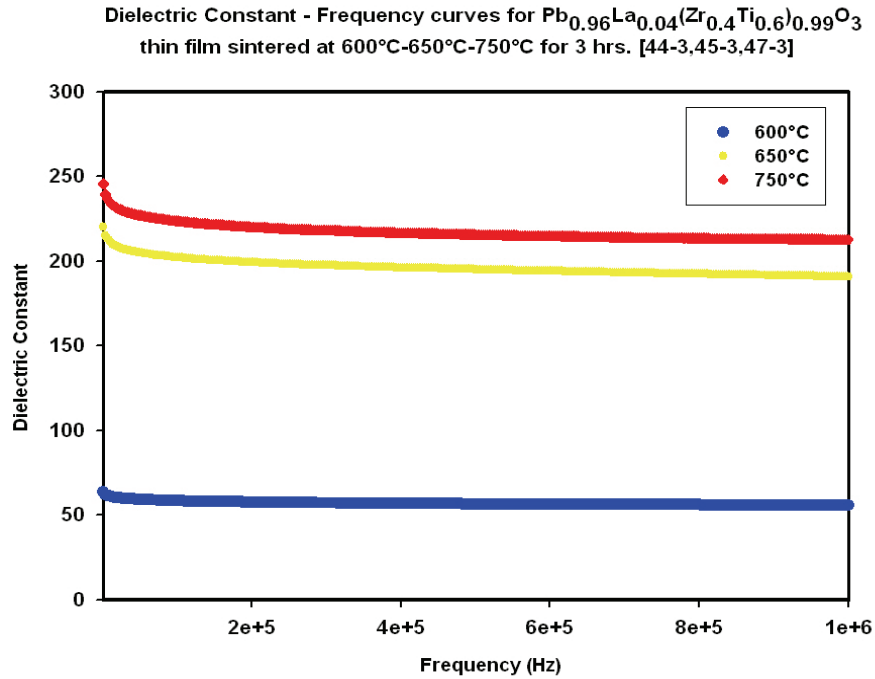


Fig. 4.22. Change of dielectric constant values of thin films with changing frequencies with respect to different sintering temperatures.

In order to investigate the effect of crystallization on dielectric properties of PLZT thin films, 600 nm (4 layers) thin PLZT film $[\text{Pb}_{0.96}\text{La}_{0.04}(\text{Zr}_{0.4}\text{Ti}_{0.6})_{0.99}\text{O}_3$ was sintered at 600 °C, 650 °C and 750 °C. As it can be seen from graphs in the Figure 4.22 above that as the sintering temperature increases, capacitance and dielectric constants of the films also increase. The reason for this is better crystallinity of the films and bigger grain size at higher temperatures. It is stated in the previous chapters that X-ray spectra at higher temperatures have very high perovskite intensities which causes better dielectric properties.

Loss tangent values of these thin films were also obtained between same frequency range 1kHz-1MHz shown as shown Figure 4.23. It was expected to be almost constant between 1kHz-1MHz frequency and sharp increase after 1MHz. However, tangent loss values starts increasing from 1kHz until the end of 1MHz. Several explanations exist for that dispersion, including finite resistance of the electrodes, the presence of a barrier layer between the insulating film and the electrode surface, or leaky grain boundaries.

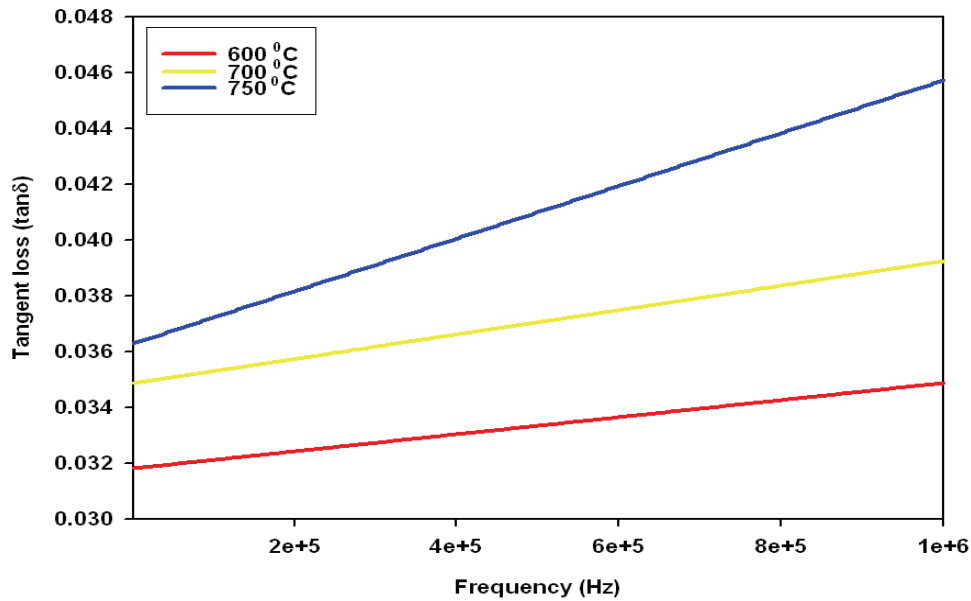


Fig. 4.23. Change of loss tangent values of $\text{Pb}_{0.96}\text{La}_{0.04}(\text{Zr}_{0.4}\text{Ti}_{0.6})_{0.99}\text{O}_3$ thin films (600 nm) with changing frequencies with respect to different sintering temperatures.

Dielectric loss originates from two mechanisms: resistive loss and relaxation loss. Resistive loss mechanism involves energy consumption by the mobile charges in the film; whereas, in the case of relaxation loss mechanism, it is the relaxation of dipole which dissipates the energy. If there are very few charges in the film then the latter mechanism is dominating. The resistive loss mechanism is directly connected to the leakage current of the film: if the leakage current is higher the loss is also higher. Alternatively, if the dielectric constant of the film is large, then an increase in dielectric loss is obvious due to the contribution from the relaxation mechanism. Enhanced polarization increases the dissipation during the relaxation [24].

In order to investigate the mechanism explaining the dielectric loss, leakage current measurements should be performed. Since resistive loss strongly depends on leakage current, it could be a possible explanation for the increase of dielectric loss.

Table 4.5. Dielectric properties of $\text{Pb}_{1-x}\text{La}_x(\text{Zr}_y\text{Ti}_{1-y})_{1-x/4}\text{O}_3$ thin films.

Composition	Film Thickness	Heat Treatment	1 kHz		1 MHz	
			Dielectric Constant	Dielectric Loss(%)	Dielectric Constant	Dielectric Loss(%)
$\text{Pb}(\text{Zr}_{0.65}\text{Ti}_{0.35})\text{O}_3$	700 nm	730 °C	268	2.9	240	10
$\text{Pb}_{0.94}\text{La}_{0.06}(\text{Zr}_{0.65}\text{Ti}_{0.35})_{0.985}\text{O}_3$	700 nm	730 °C	244	2.8	221	3.2
$\text{Pb}_{0.91}\text{La}_{0.09}(\text{Zr}_{0.65}\text{Ti}_{0.35})_{0.975}\text{O}_3$	700 nm	730 °C	146	2.7	132	5.3
$\text{Pb}(\text{Zr}_{0.52}\text{Ti}_{0.48})\text{O}_3$	600 nm	730 °C	431	21.3	241	8.6
$\text{Pb}_{0.95}\text{La}_{0.05}(\text{Zr}_{0.52}\text{Ti}_{0.48})_{0.9875}\text{O}_3$	600 nm	730 °C	230	6.1	197	4.5
$\text{Pb}(\text{Zr}_{0.4}\text{Ti}_{0.6})\text{O}_3$	600 nm	730 °C	141	2.7	128	4.8
$\text{Pb}_{0.98}\text{La}_{0.02}(\text{Zr}_{0.4}\text{Ti}_{0.6})_{0.99}\text{O}_3$	600 nm	730 °C	214	3.2	193	8.4
$\text{Pb}_{0.94}\text{La}_{0.06}(\text{Zr}_{0.4}\text{Ti}_{0.6})_{0.985}\text{O}_3$	600 nm	730 °C	228	2.7	207	5.8
$\text{Pb}_{0.9}\text{La}_{0.1}(\text{Zr}_{0.4}\text{Ti}_{0.6})_{0.975}\text{O}_3$	600 nm	730 °C	287	3.2	257	10.3
$\text{Pb}_{0.88}\text{La}_{0.12}(\text{Zr}_{0.4}\text{Ti}_{0.6})_{0.965}\text{O}_3$	600 nm	730 °C	158	3.1	142	4
$\text{Pb}_{0.78}\text{La}_{0.22}(\text{Zr}_{0.4}\text{Ti}_{0.6})_{0.94}\text{O}_3$	600 nm	730 °C	92.5	3.3	83.5	6.5

The dielectric properties of $\text{Pb}_{1-x}\text{La}_x(\text{Zr}_y\text{Ti}_{1-y})_{1-x}\text{O}_3$ thin films were also studied as a function of composition. These properties depend on both Zr/Ti ratio and La content of the films. To investigate the effect of these parameters, 3 different Zr/Ti ratios were selected by considering 3 regions of PLZT phase diagram. These ratios are 65/35 from the rhombohedral, 52/48 from the morphotropic phase boundary (MPB) and 40/60 from tetragonal regions. At first, the effect of these compositions without any La content on dielectric properties were studied. Then, La% was raised to see the effects of La. During these investigations, the other parameters such as film thickness (600 nm-700 nm) were almost kept constant and same heat treatment was applied to all of the samples.

For the measurements on the morphotropic phase boundary (MPB), compositions $\text{Pb}(\text{Zr}_{0.52}\text{Ti}_{0.48})\text{O}_3$ and $\text{Pb}_{0.95}\text{La}_{0.05}(\text{Zr}_{0.52}\text{Ti}_{0.48})_{0.9875}\text{O}_3$ were studied. Highest dielectric constant was obtained for $\text{Pb}(\text{Zr}_{0.52}\text{Ti}_{0.48})\text{O}_3$ thin film with thickness 600 nm as 431 at 1kHz. The dielectric constant of $\text{Pb}_{0.95}\text{La}_{0.05}(\text{Zr}_{0.52}\text{Ti}_{0.48})_{0.9875}\text{O}_3$ thin film was 230 at 1kHz. As the La content of the films on MPB increased, their dielectric constants decreased. Moreover, tangent loss values decreased also while La content was increased as shown in Table 4.5. Figures 4.24 and 4.25 show the change of dielectric constant of the $\text{Pb}(\text{Zr}_{0.52}\text{Ti}_{0.48})\text{O}_3$ and $\text{Pb}_{0.95}\text{La}_{0.05}(\text{Zr}_{0.52}\text{Ti}_{0.48})_{0.9875}\text{O}_3$ films between 1kHz-1MHz frequency range.

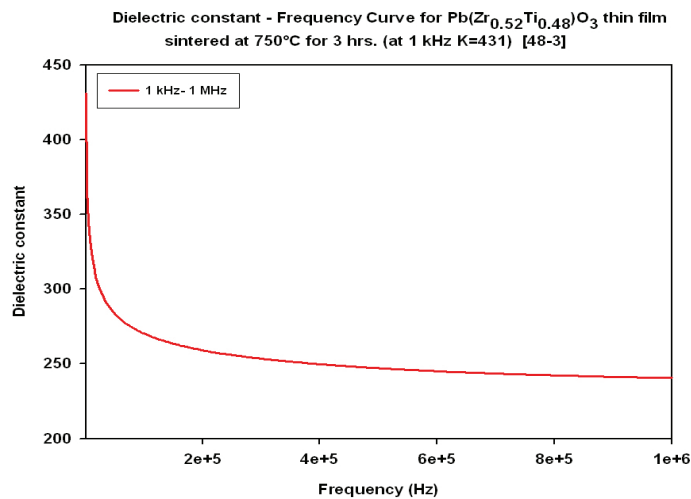


Fig. 4.24. Change of dielectric constant of $\text{Pb}(\text{Zr}_{0.52}\text{Ti}_{0.48})\text{O}_3$ thin film with frequency.

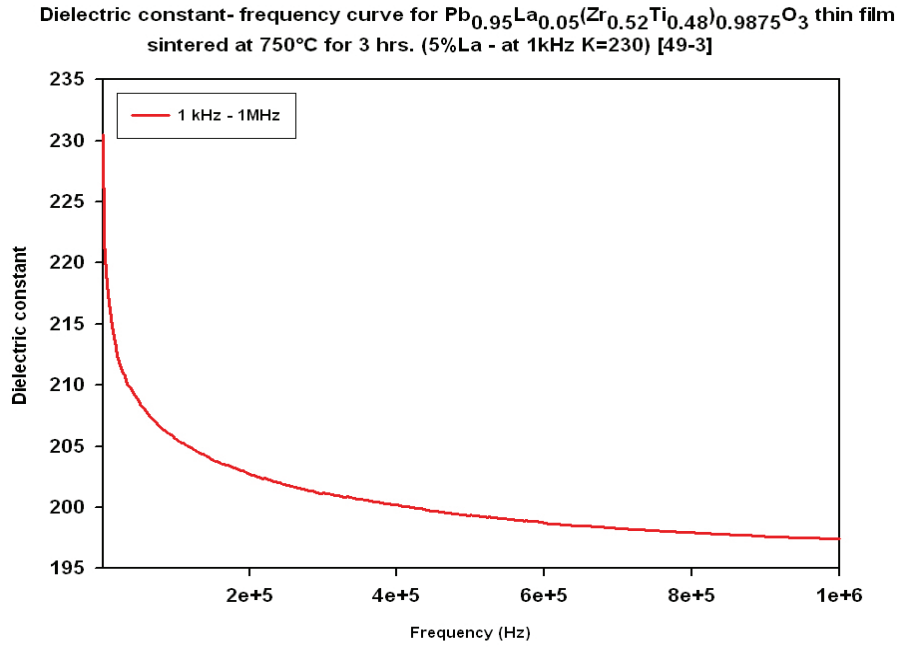


Fig. 4.25. Change of dielectric constant of $\text{Pb}_{0.95}\text{La}_{0.05}(\text{Zr}_{0.52}\text{Ti}_{0.48})_{0.9875}\text{O}_3$ thin film with frequency.

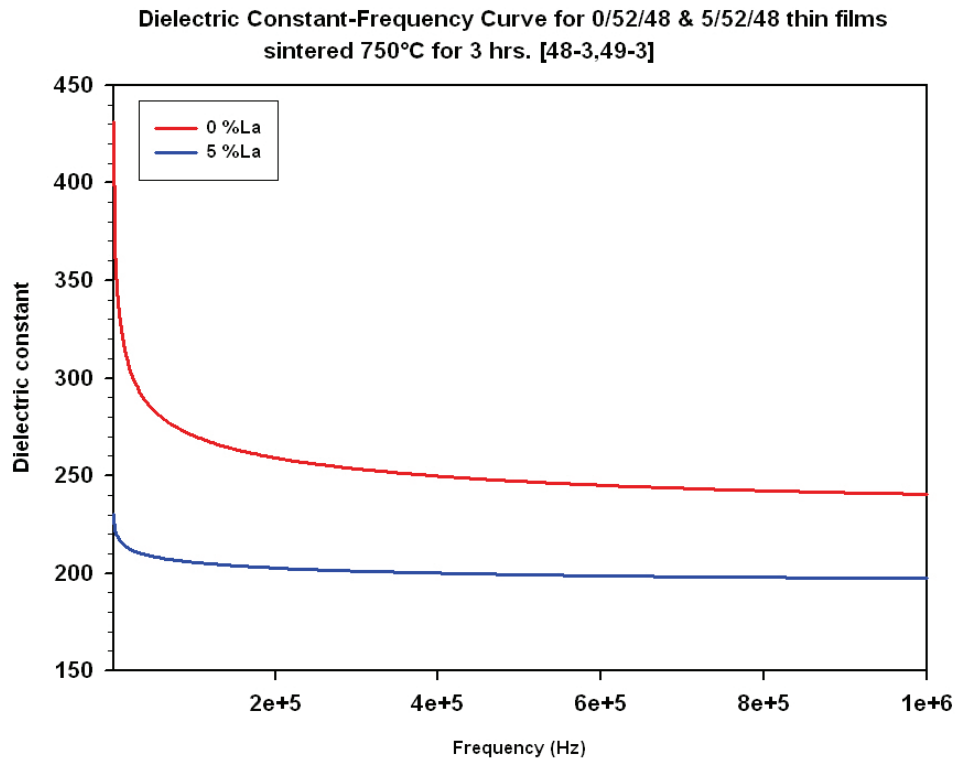


Fig. 4.26. Dielectric constants of $\text{Pb}(\text{Zr}_{0.52}\text{Ti}_{0.48})\text{O}_3$ - $\text{Pb}_{0.95}\text{La}_{0.05}(\text{Zr}_{0.52}\text{Ti}_{0.48})_{0.9875}\text{O}_3$ thin films changing frequency.

The same tendency was obtained for the rhombohedral region compositions $\text{Pb}(\text{Zr}_{0.65}\text{Ti}_{0.35})\text{O}_3$, $\text{Pb}_{0.94}\text{La}_{0.06}(\text{Zr}_{0.65}\text{Ti}_{0.35})_{0.985}\text{O}_3$ and $\text{Pb}_{0.91}\text{La}_{0.09}(\text{Zr}_{0.65}\text{Ti}_{0.35})_{0.9775}\text{O}_3$. Other researchers also observed the same tendency in the change of dielectric constant with these compositions. For example, Reji Thomas [19] obtained dielectric constants of $\text{Pb}(\text{Zr}_{0.65}\text{Ti}_{0.35})\text{O}_3$ and $(\text{Pb},\text{La}_{0.08})(\text{Zr}_{0.65},\text{Ti}_{0.35})\text{O}_3$ films as 720 and 440 at 10kHz, respectively and the loss tangent values as 0.045 and 0.038, respectively. In this study, the films with those compositions have thickness 700 nm. PZT [$\text{Pb}(\text{Zr}_{0.65}\text{Ti}_{0.35})\text{O}_3$] thin film had a dielectric constant 268 at 1kHz and decreases to 146 at which La content was 9%. Figures 4.27-28-29 display the dielectric constant change as a function of frequency in the range of 1kHz-1MHz.

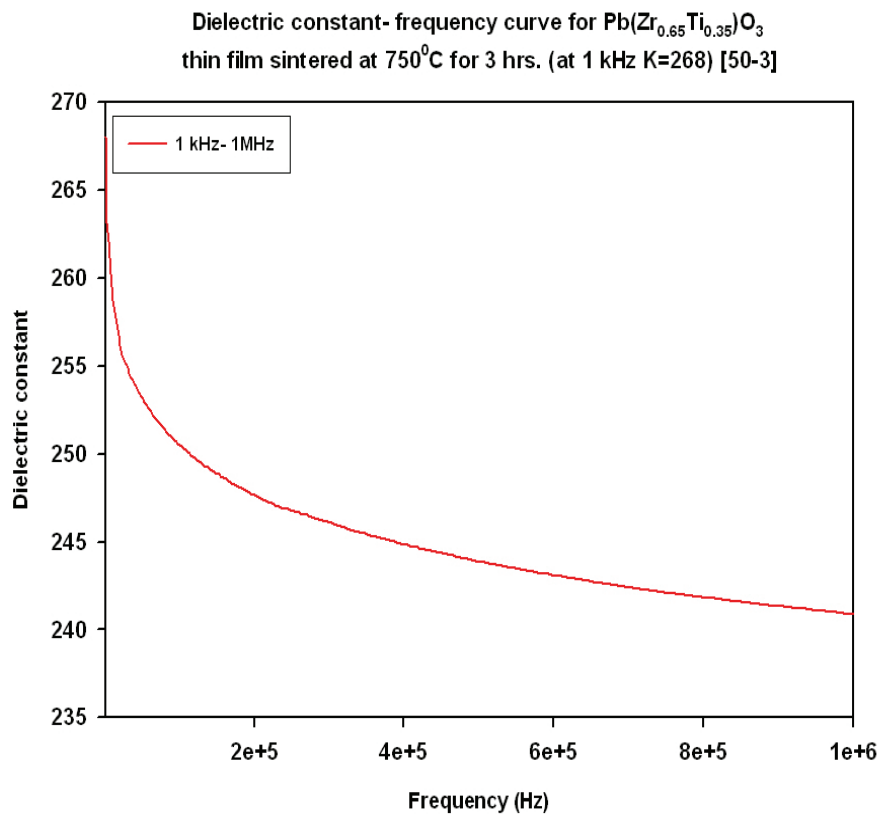


Fig. 4.27. Change of dielectric constant of $\text{Pb}(\text{Zr}_{0.65}\text{Ti}_{0.35})\text{O}_3$ thin film with frequency.

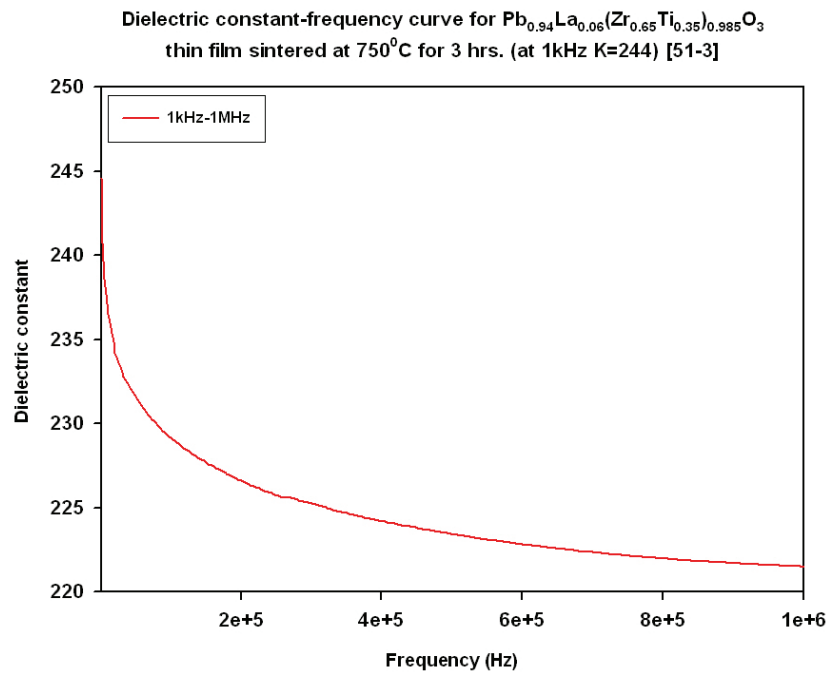


Fig. 4.28. Dielectric constant-frequency curve of $\text{Pb}_{0.94}\text{La}_{0.06}(\text{Zr}_{0.65}\text{Ti}_{0.35})_{0.985}\text{O}_3$ thin film.

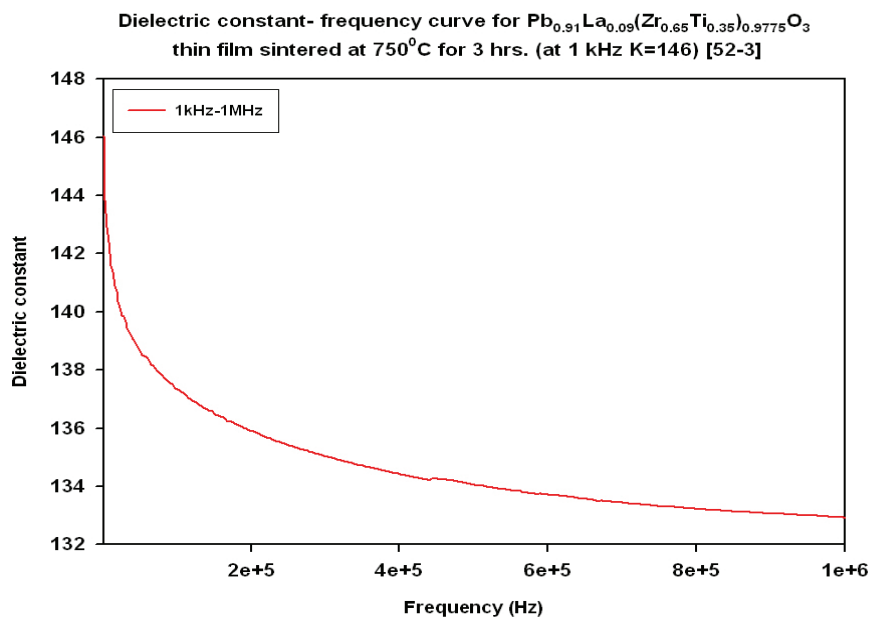


Fig. 4.29. Dielectric constant –frequency curve of $\text{Pb}_{0.91}\text{La}_{0.09}(\text{Zr}_{0.65}\text{Ti}_{0.35})_{0.9775}\text{O}_3$ thin film.

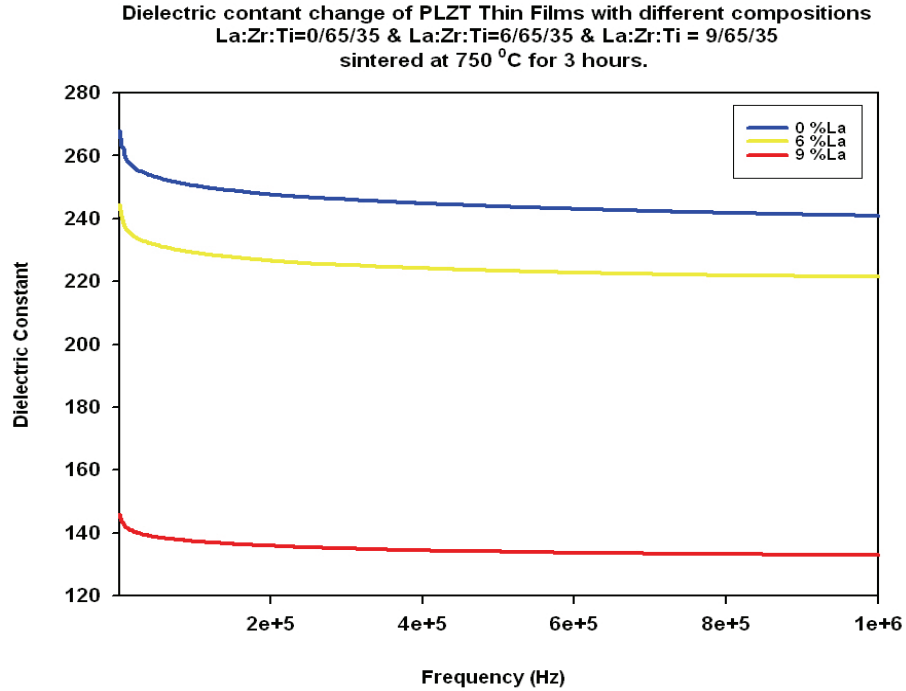


Fig. 4.30. Dielectric constant –frequency curves of $\text{Pb}_{0.94}\text{La}_{0.09}(\text{Zr}_{0.65}\text{Ti}_{0.35})_{0.9775}\text{O}_3$, $\text{Pb}_{0.94}\text{La}_{0.06}(\text{Zr}_{0.65}\text{Ti}_{0.35})_{0.985}\text{O}_3$, $\text{Pb}(\text{Zr}_{0.65}\text{Ti}_{0.35})\text{O}_3$ films sintered at 750 °C for 3 hrs.

The dielectric characterization associated with crystal structure changes as a function of La content for $\text{Pb}_{1-x}\text{La}_x(\text{Zr}_{0.4}\text{Ti}_{0.6})_{1-x/4}\text{O}_3$ thin films were also investigated. For these investigations, 6 compositions starting from tetragonal region with increasing La content were prepared, coated and annealed at 750 °C. Thin films with thicknesses 600 nm and composition of $\text{Pb}(\text{Zr}_{0.4}\text{Ti}_{0.6})\text{O}_3$, $\text{Pb}_{0.96}\text{La}_{0.04}(\text{Zr}_{0.4}\text{Ti}_{0.6})_{0.99}\text{O}_3$, $\text{Pb}_{0.94}\text{La}_{0.06}(\text{Zr}_{0.4}\text{Ti}_{0.6})_{0.985}\text{O}_3$, $\text{Pb}_{0.9}\text{La}_{0.1}(\text{Zr}_{0.4}\text{Ti}_{0.6})_{0.975}\text{O}_3$, $\text{Pb}_{0.86}\text{La}_{0.14}(\text{Zr}_{0.4}\text{Ti}_{0.6})_{0.965}\text{O}_3$ and $\text{Pb}_{0.76}\text{La}_{0.24}(\text{Zr}_{0.4}\text{Ti}_{0.6})_{0.94}\text{O}_3$ were produced. Tetragonality (c/a ratio) of PLZT thin films in this region was decreased as La content increased. PLZT thin films with 0-4-6-10% La content are found to be tetragonal crystallographically. When La content increases to 14%, it is pseudocubic at the phase boundary between tetragonal to cubic and it is cubic when La content reaches to 24%.

Figures 4.31-32-33-34-35-36 show the dielectric constant-frequency curves of PLZT thin films having 0-4-6-10-14-24% La content. Tetragonal PLZT film with 10% La had a dielectric constant maximum of 287 at 1kHz at room temperature. The PLZT thin film with that composition shows broader dielectric

peaks, compared with those of bulk ceramics, and behaves as relaxor ferroelectrics [26]. The dielectric constant decreased dramatically after 10 at%La. When La content reaches to 24 at%, the dielectric constant shows a minimum value because of being in cubic region in which thin films show paraelectric behavior.

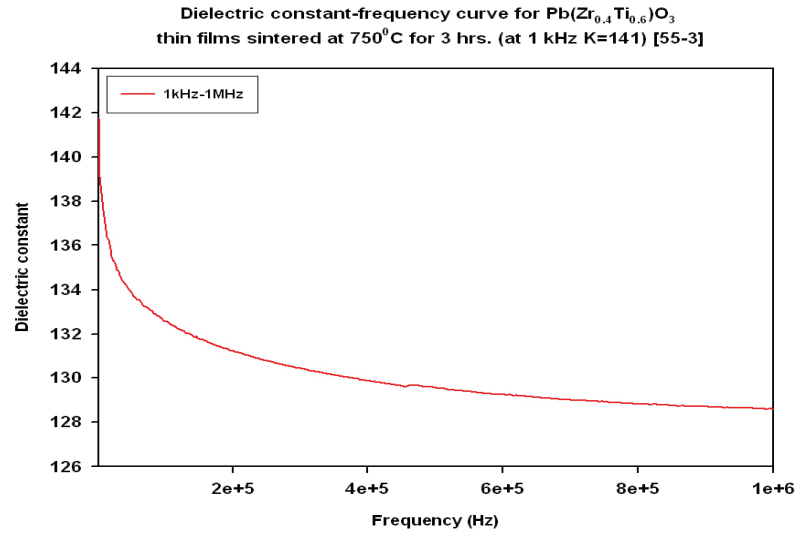


Fig. 4.31. Change of dielectric constant of $\text{Pb}(\text{Zr}_{0.4}\text{Ti}_{0.6})\text{O}_3$ thin film with frequency.

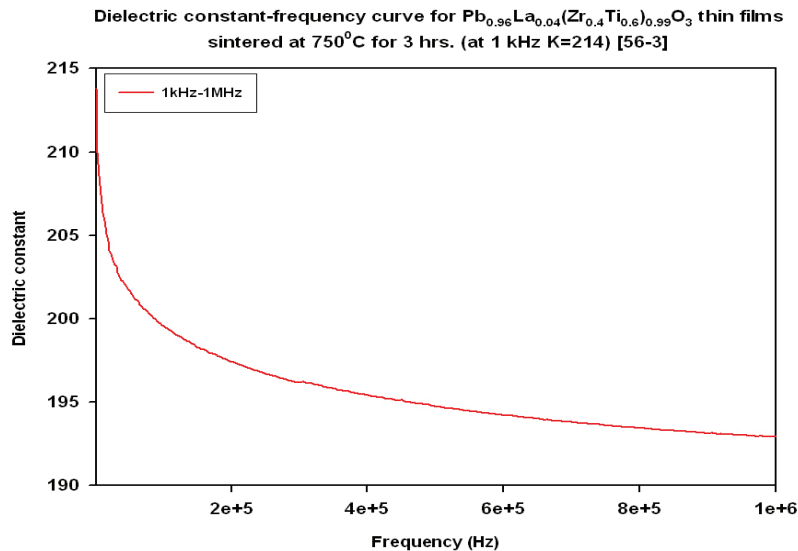


Fig. 4.32. Dielectric constant–frequency curve of $\text{Pb}_{0.96}\text{La}_{0.04}(\text{Zr}_{0.4}\text{Ti}_{0.6})_{0.99}\text{O}_3$ thin film.

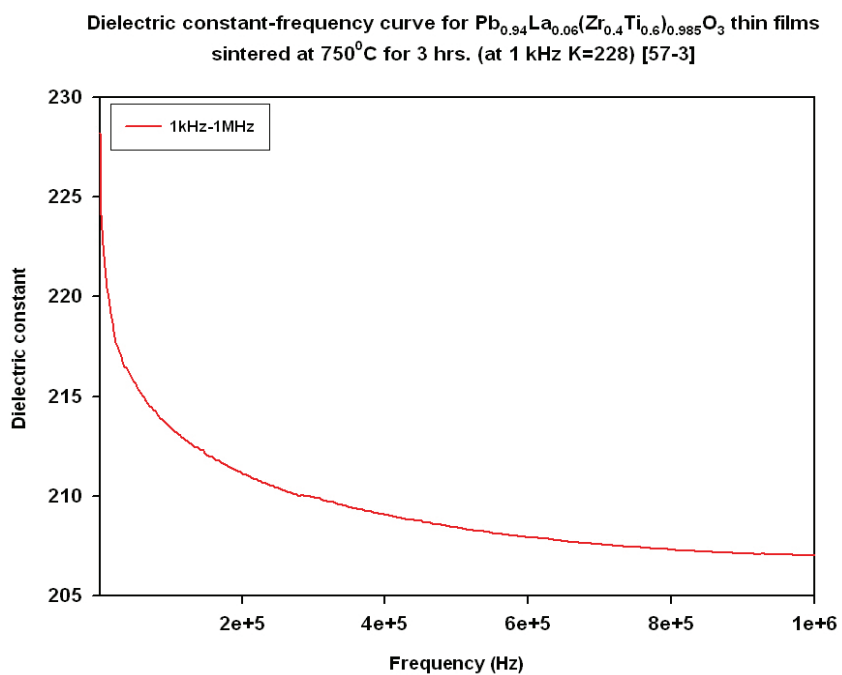


Fig. 4.33. Dielectric constant- frequency curve of $\text{Pb}_{0.94}\text{La}_{0.06}(\text{Zr}_{0.4}\text{Ti}_{0.6})_{0.985}\text{O}_3$ thin film.

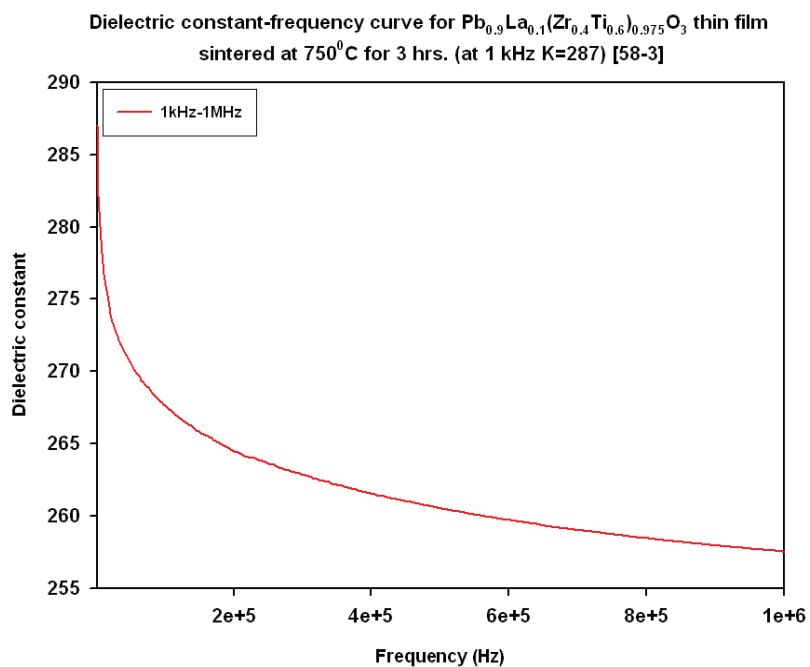


Fig. 4.34. Dielectric constant- frequency curve of $\text{Pb}_{0.9}\text{La}_{0.1}(\text{Zr}_{0.4}\text{Ti}_{0.6})_{0.975}\text{O}_3$ thin film.

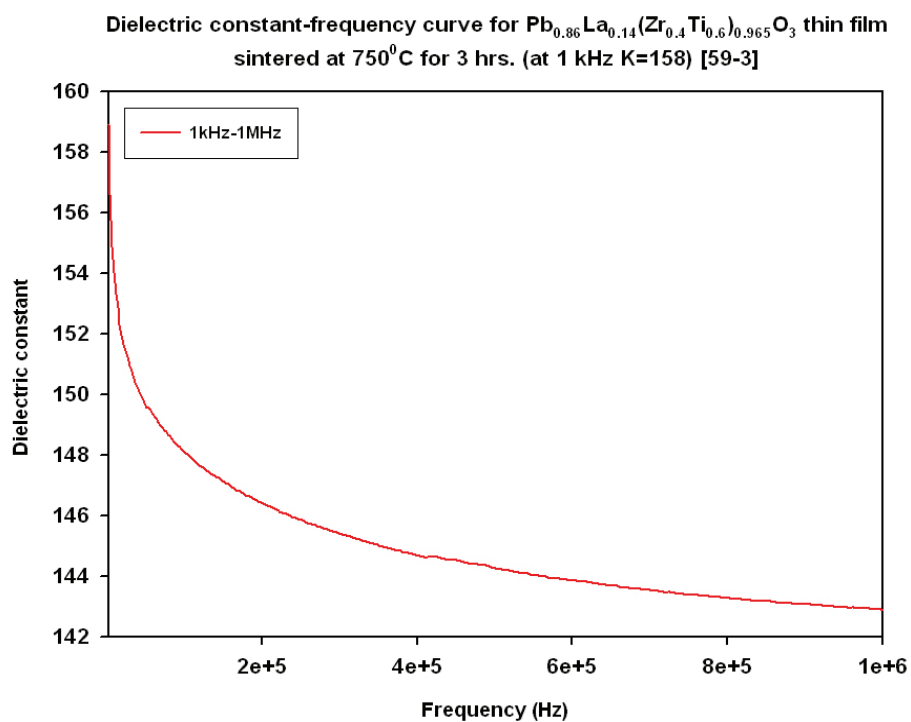


Fig. 4.35. Dielectric constant – frequency of $\text{Pb}_{0.86}\text{La}_{0.14}(\text{Zr}_{0.4}\text{Ti}_{0.6})_{0.965}\text{O}_3$ thin film.

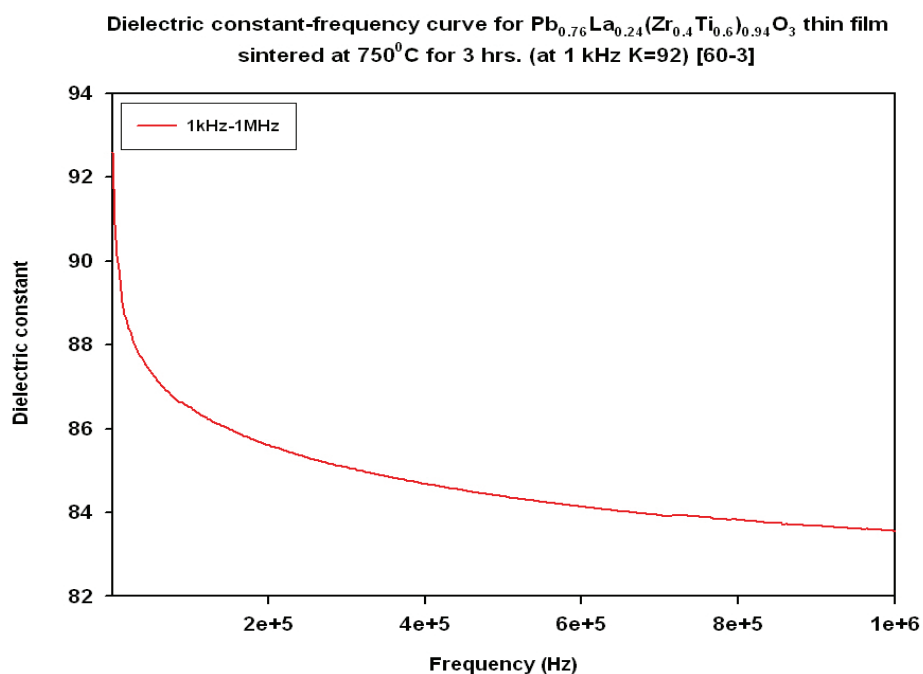


Fig. 4.36. Change of dielectric constant of $\text{Pb}_{0.76}\text{La}_{0.24}(\text{Zr}_{0.4}\text{Ti}_{0.6})_{0.94}\text{O}_3$ thin film with frequency.

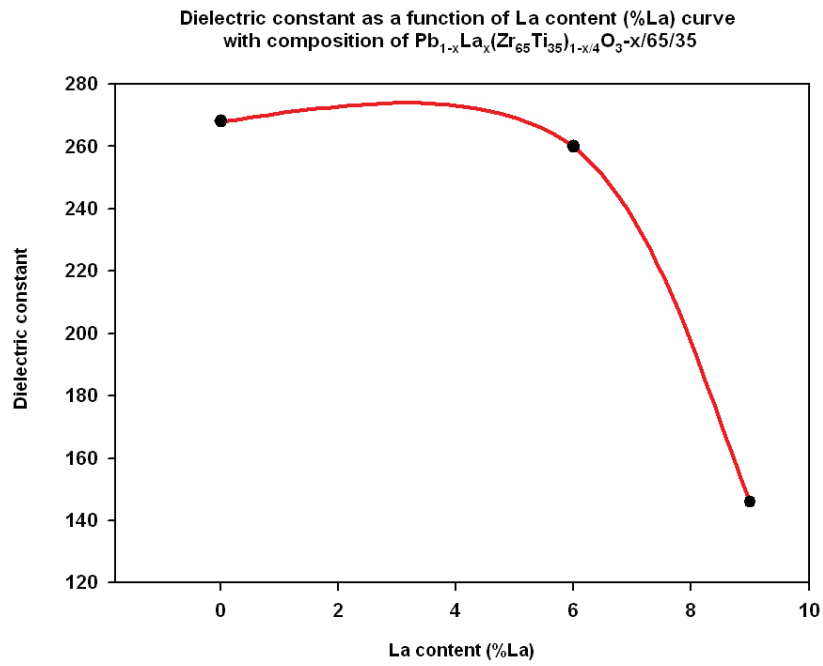


Fig. 4.37. Change of dielectric constant as a function of La content of x/65/35 thin film.

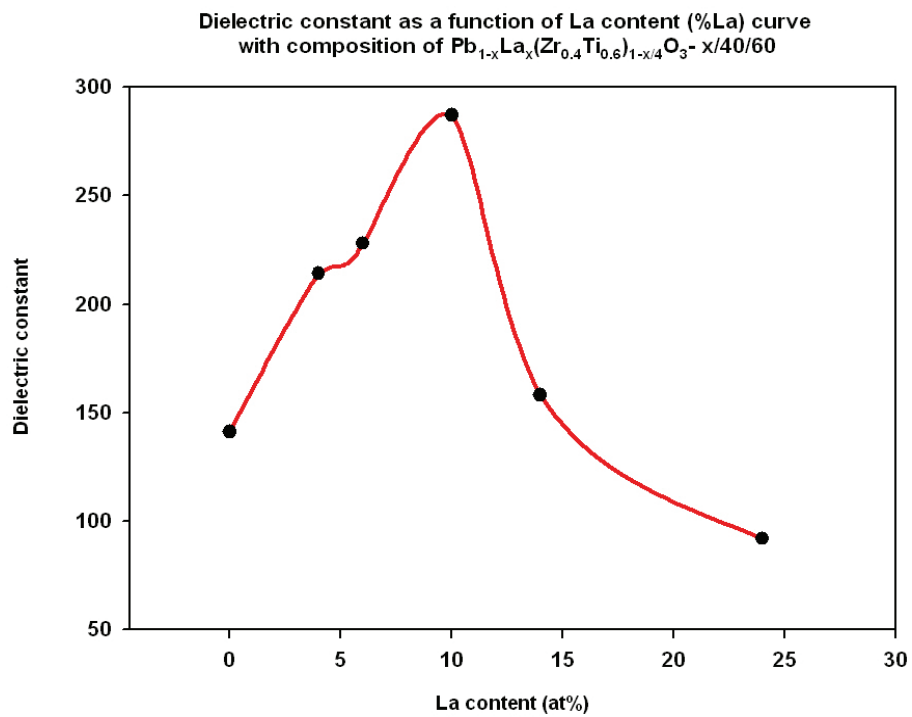


Fig. 4.38. Change of dielectric constant as a function of La content of x/40/60 thin film.

Figures 4.37-38 show the change of dielectric constant with increasing La content in the rhombohedral and tetragonal compositions of thin films. As it can be seen from the Fig. 4.37 that as the lanthanum content increases, dielectric constant of the film decreases. In Fig. 4.38, there is a peak point at which dielectric constant reaches maximum value. For thin film with x/40/60 composition, $\text{Pb}_{0.9}\text{La}_{0.1}(\text{Zr}_{0.4}\text{Ti}_{0.6})_{0.975}\text{O}_3$ thin film has maximum dielectric constant. After that point, it starts decreasing and becomes minimum at 24% La content.

The dielectric constants of PLZT thin films found in this study is generally lower than the values in the literature. One of the reasons about that is the grain size of the films. As grain size increases, dielectric constant of films increases in this study. The grain size of thin films in the literature is in the range of 20-30 nm. In this study, grain sizes were found between 3 nm (min) and 16 nm (max). That can be a reason of decrease in dielectric constant. Dielectric properties also depend on the substrate – film interface. RTA (Rapid Thermal Annealing) is a new method that is said to improve this interface. The great advantages of this method are a short annealing time and its relative process simplicity as compared with the conventional furnace annealing. The objective of the short processing time is to basically reduce the time and temperature product such that the desired physical or chemical processes are completed while the unwanted processes such as dopant diffusion, interface reactions, decomposition, or evaporation, etc., are suppressed or minimized. The short rise time to the desired annealing temperature minimizes the interface reactions and results in a dense microstructure [24].

4.6. Ferroelectric Properties of PLZT Thin Films

The ferroelectric properties of PLZT thin films such as hysteresis loops (polarization-electric field) and capacitance-voltage (C-V) curves were also observed as a function of heat treatment and composition. In order to investigate the effect of heat treatment on ferroelectric properties such as remanent polarization and coercive field, four sintering temperatures were applied to PLZT thin films. Moreover, different sintering times were performed with these sintering temperatures. Table 4.6 shows the results of heat treatments conditions on ferroelectric properties remanent polarization and coercive field with various applied voltages.

In addition to ferroelectric hysteresis loops, capacitance change with with applied bias voltage (C-V) behavior was studied. These observations are in a relationship with ferroelectricity and that is why they are included in this section. These C-V curves were obtained by applying a DC voltage with oscillation voltage of 0.5V. C-V curves are actually measure of hysteresis curves. C-V profile is obtained by dP/dE , so the peak in the C-V characteristic corresponds to a large polarization change, or the switching of ferroelectric domains from one orientation to another which is done by coercive field.

The C-V curves were drawn by applying DC bias voltage in the range of 10V to -10V. It was first increased to 10V in 0.5V intervals, and then decreased to 0V followed by increased in the reverse polarity to -10V. Finally, it was raised up to 10V again.

Table 4.6. Ferroelectric properties of PLZT film of composition $\text{Pb}_{0.96}\text{La}_{0.04}(\text{Zr}_{0.4}\text{Ti}_{0.6})_{0.99}\text{O}_3$ annealed at different temperatures and time.

Sample no	Thickness(nm)	Heat Treat.Temp.	Heat Treat.Time	Remanent Polar.(Pr)	Coersive Field (kV/cm)	Applied voltage (V)
44-1	600 nm	600°C	1 hr	0.22	26.6	5 V
44-1	600 nm	600°C	1 hr	1.96	85.8	10 V
44-1	600 nm	600°C	1 hr	4.67	128	15 V
44-2	600 nm	600°C	2 hrs	0.16	26.7	5 V
44-2	600 nm	600°C	2 hrs	1.31	79.2	10 V
44-2	600 nm	600°C	2 hrs	4.28	109.3	15 V
44-3	600 nm	600°C	3 hrs	0.027	10	5 V
44-3	600 nm	600°C	3 hrs	0.16	52	10 V
44-3	600 nm	600°C	3 hrs	0.56	108	15 V
45-1	600 nm	650°C	1 hr	0.288	33.3	5 V
45-1	600 nm	650°C	1 hr	1.4	72.3	10 V
45-1	600 nm	650°C	1 hr	3.13	109	15 V
45-2	600 nm	650°C	2 hrs	0.53	36.6	5 V
45-2	600 nm	650°C	2 hrs	2.95	79.1	10 V
45-2	600 nm	650°C	2 hrs	7.58	109.2	15 V
45-3	600 nm	650°C	3 hrs	0.55	36.6	5 V
45-3	600 nm	650°C	3 hrs	2.54	85.6	10 V
45-3	600 nm	650°C	3 hrs	6.194	128.2	15 V
46-1	600 nm	700°C	1 hr	0.44	36.6	5 V
46-1	600 nm	700°C	1 hr	2.53	79.2	10 V
46-1	600 nm	700°C	1 hr	5.17	119.2	15 V
46-2	600 nm	700°C	2 hrs	0.057	20	5 V
46-2	600 nm	700°C	2 hrs	0.46	72.4	10 V
46-2	600 nm	700°C	2 hrs	1.53	128.7	15 V
46-3	600 nm	700°C	3 hrs	0.7	40	5 V
46-3	600 nm	700°C	3 hrs	3.5	92.1	10 V
46-3	600 nm	700°C	3 hrs	6.94	129	15 V
47-1	600 nm	750°C	1 hr	0.55	36.6	5 V
47-1	600 nm	750°C	1 hr	3	92.6	10 V
47-1	600 nm	750°C	1 hr	6.72	128.7	15 V
47-2	600 nm	750°C	2 hrs	0.3	36.6	5 V
47-2	600 nm	750°C	2 hrs	2.24	98.8	10 V
47-2	600 nm	750°C	2 hrs	4	128.5	15 V
47-3	600 nm	750°C	3 hrs	0.76	43.3	5 V
47-3	600 nm	750°C	3 hrs	4.96	92.2	10 V
47-3	600 nm	750°C	3 hrs	10.49	131	15 V

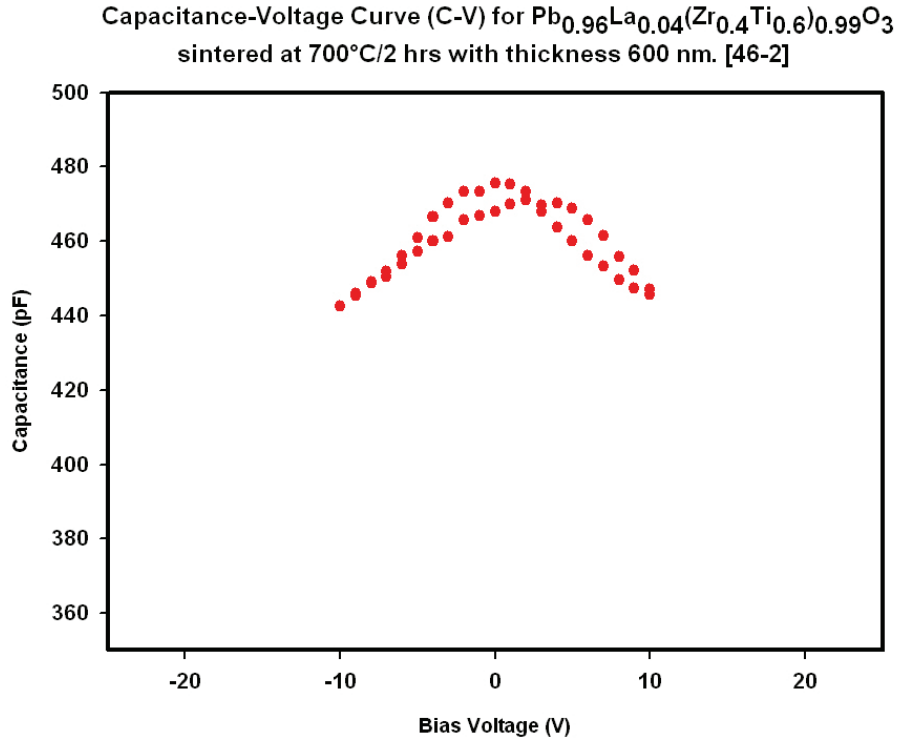


Fig. 4.39. The C-V curve for 600 nm thick PLZT film. (butterfly shaped curve indicating ferroelectric nature of the film).

It is seen from the Figure 4.39 that the curve is symmetric and the peak positions, which represent the coercive voltage for polarization reversal, were slightly shifted to the negative direction on the axis of applied voltage and the values of the peaks are different at the processes of sweep-up and sweep-down by applying bias voltage. The shift of the peak indicated that the internal field existed in the PLZT thin films. The difference of the peak values due to the difference of a potential barrier between the top electrode (Ag) and bottom electrode (Pt) [25].

Figure 4.40 shows the change of remanent polarization of PLZT thin film as a function of sintering temperature. As it can be seen clearly that as the sintering temperature increases, the remanent polarization of the film increases. There can be two reasons for this increase one of which is being better crystallinity at high temperatures and the other one is increase in grain size. When the grain size increases, this would cause an increase in density of dipoles which can result in raise of polarization density.

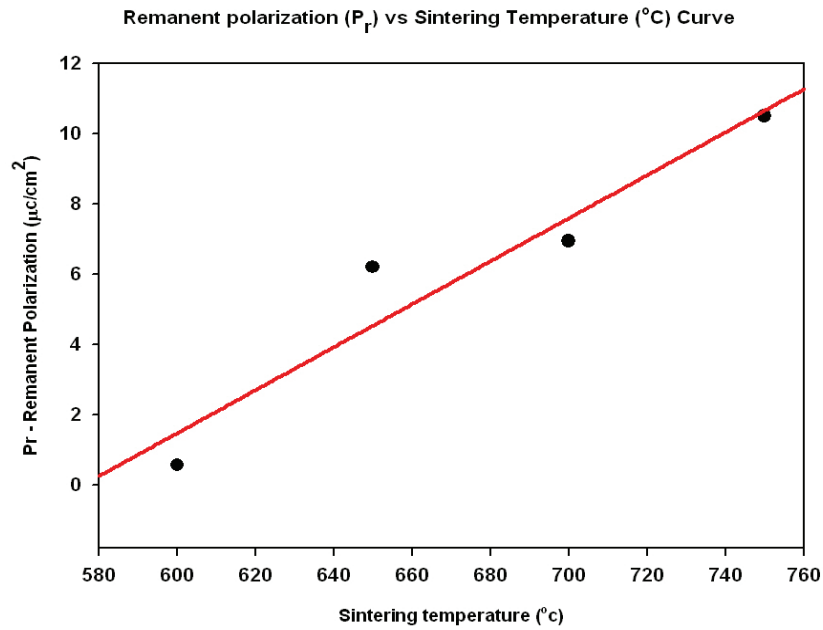


Fig. 4.40. Change of remanent polarization of 600 nm $\text{Pb}_{0.96}\text{La}_{0.04}(\text{Zr}_{0.4}\text{Ti}_{0.6})_{0.99}\text{O}_3$ thin film as a function of sintering temperature. ($t_{\text{sintering}} = 3 \text{ hrs}$)

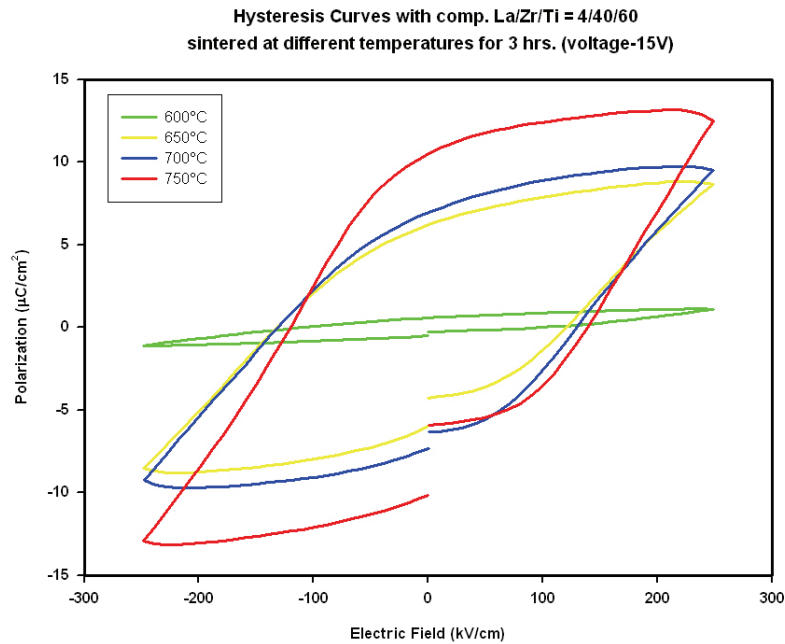


Fig. 4.41. Change of hysteresis behavior of 600 nm $\text{Pb}_{0.96}\text{La}_{0.04}(\text{Zr}_{0.4}\text{Ti}_{0.6})_{0.99}\text{O}_3$ thin film as a function of sintering temperature.

Figure 4.41 shows the hysteresis behaviour of the films sintered at 600 °C, 650 °C, 700 °C and 750 °C. As the temperature was increased, the hysteresis curves lost their slim appearance. Both the remanent polarization (P_r) and coercive field (E_c) increased with increasing the sintering temperature rise. P_r value showed a rise from 0.56 $\mu\text{C}/\text{cm}^2$ to 10.49 $\mu\text{C}/\text{cm}^2$ as the sintering temperature was increased from 600 °C to 750 °C while E_c values increased from 108 kV/cm to 131 kV/cm measured at 15V.

The ferroelectric properties of PLZT thin films are affected also by the composition. These properties were investigated by the change of Zr/Ti ratio and La content like observations in the dielectric properties. Table 4.7 shows the ferroelectric measurements of PLZT thin films for the different eleven compositions and sintered at 750 °C for 3 hours.

The effect of the compositions on the ferroelectric properties of thin films are nearly the same for $\text{Pb}_{1-x}\text{La}_x(\text{Zr}_{0.52}\text{Ti}_{0.48})_{1-x/4}\text{O}_3$ and $\text{Pb}_{1-x}\text{La}_x(\text{Zr}_{0.65}\text{Ti}_{0.35})_{1-x/4}\text{O}_3$. As La content increased, slim hysteresis loops were obtained. La was increased up to 9 at% for the PLZT thin film $\text{Pb}_{1-x}\text{La}_x(\text{Zr}_{0.65}\text{Ti}_{0.35})_{1-x/4}\text{O}_3$ and the values of remanent polarization and coercive field was measured as 3.6 $\mu\text{C}/\text{cm}^2$ and 128.6 kV/cm, respectively, for the 0 %La. When La content was increased to 9%, these values decreased to 1.68 $\mu\text{C}/\text{cm}^2$ and 125 kV/cm, respectively. For the $\text{Pb}_{1-x}\text{La}_x(\text{Zr}_{0.52}\text{Ti}_{0.48})_{1-x/4}\text{O}_3$ thin films, same tendency was observed. For that composition with 0% La content, $P_r = 1.14 \mu\text{C}/\text{cm}^2$ and $E_c = 40 \text{ kV}/\text{cm}$ measured at 5V. When the La content became 5% La, these values decreased to 0.64 $\mu\text{C}/\text{cm}^2$ and 38.2 kV/cm. Figures 4.41-42-43 show the $\text{Pb}_{1-x}\text{La}_x(\text{Zr}_{0.65}\text{Ti}_{0.35})_{1-x/4}\text{O}_3$ film hysteresis curves with respect to La content and at different voltages. Figure 4.44 displays hysteresis loops of the La:Zr:Ti=0/65/35 and La:Zr:Ti=9/65/35 thin films indicating slimmer curve. Similar behavior for the La:Zr:Ti=0/52/48 and La:Zr:Ti=5/52/48 thin films given in Figure 4.46.

Increasing the La^{3+} content is expected to lead to excess positive charges which are compensated by V_{pb}'' vacancies. As a consequence domain mobility is

greatly enhanced and lower coercive fields as well as a higher squareness of the hysteresis loops are expected. The present results show, however, that increasing the La^{3+} content leads to lower maximum and remanent polarization as well as a little bit coercive field. It appears that the positive effects of lanthanum found in bulk ceramics do not fully apply to thin films probably due to residual stresses associated with the mismatch of thermal expansion coefficients between the substrate and the deposited film. Furthermore, it has been shown that interfacial reactions between the thin film and the Pt electrode lead to an interfacial, low permittivity layer of approximately 80 nm which is expected to be detrimental to the dielectric properties [21].

Table 4.7. Ferroelectric properties of $\text{Pb}_{1-x}\text{La}_x(\text{Zr}_y\text{Ti}_{1-y})_{1-x/4}\text{O}_3$ PLZT thin films.

Composition	Film Thickness	Heat Treatment	Coercive Field, E_c (kV/cm)	Remanent Polarization, P_r ($\mu\text{C}/\text{cm}^2$)	Applied Voltage (V)
$\text{Pb}(\text{Zr}_{0.65}\text{Ti}_{0.35})\text{O}_3$	700 nm	750 °C	29.9	0.317	5
			79.6	1.53	10
			128.1	3.6	15
$\text{Pb}_{0.94}\text{La}_{0.06}(\text{Zr}_{0.65}\text{Ti}_{0.35})_{0.985}\text{O}_3$	700 nm	750 °C	33.3	0.24	5
			98.4	1.73	10
			148	4.21	15
$\text{Pb}_{0.91}\text{La}_{0.09}(\text{Zr}_{0.65}\text{Ti}_{0.35})_{0.9775}\text{O}_3$	700 nm	750 °C	23.2	0.08	5
			79.2	0.53	10
			125	1.68	15
$\text{Pb}(\text{Zr}_{0.52}\text{Ti}_{0.48})\text{O}_3$	600 nm	750 °C	24	0.63	3
			40	1.14	5
			80	3	8
$\text{Pb}_{0.95}\text{La}_{0.05}(\text{Zr}_{0.52}\text{Ti}_{0.48})_{0.9875}\text{O}_3$	600 nm	750 °C	38.2	0.64	5
			64	1.16	8
			79	2.56	10
$\text{Pb}(\text{Zr}_{0.4}\text{Ti}_{0.6})\text{O}_3$	600 nm	750 °C	43.3	0.38	5
			106	3.3	10
			158	8	15
$\text{Pb}_{0.96}\text{La}_{0.04}(\text{Zr}_{0.4}\text{Ti}_{0.6})_{0.99}\text{O}_3$	600 nm	750 °C	36.6	0.56	5
			85.1	2.8	10
			118	6.4	15
$\text{Pb}_{0.94}\text{La}_{0.06}(\text{Zr}_{0.4}\text{Ti}_{0.6})_{0.985}\text{O}_3$	600 nm	750 °C	50	0.9	5
			100.2	5.2	10
			135	11	15
$\text{Pb}_{0.9}\text{La}_{0.1}(\text{Zr}_{0.4}\text{Ti}_{0.6})_{0.975}\text{O}_3$	600 nm	750 °C	40	0.8	5
			92	4	10
			128	8	15
$\text{Pb}_{0.86}\text{La}_{0.14}(\text{Zr}_{0.4}\text{Ti}_{0.6})_{0.965}\text{O}_3$	600 nm	750 °C	33.3	0.24	5
			74	0.96	10
			109	2	15
$\text{Pb}_{0.76}\text{La}_{0.24}(\text{Zr}_{0.4}\text{Ti}_{0.6})_{0.94}\text{O}_3$	600 nm	750 °C	36.6	0.12	5
			75	1.36	10
			98	2.28	15

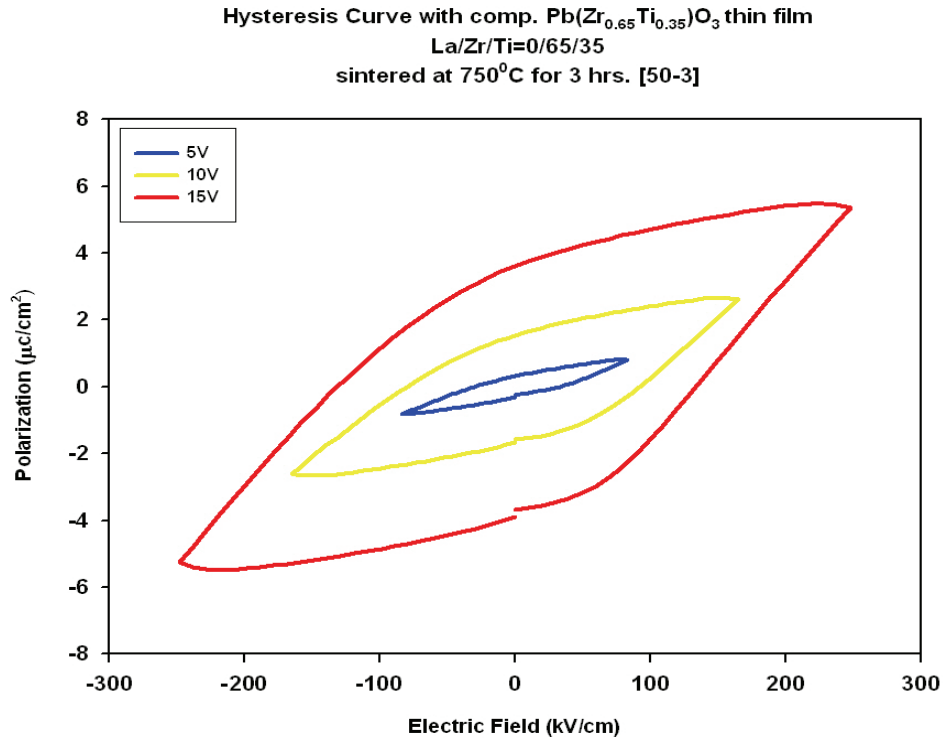


Fig. 4.42. Ferroelectric hysteresis loop of $\text{Pb}(\text{Zr}_{0.65}\text{Ti}_{0.35})\text{O}_3$ thin film.

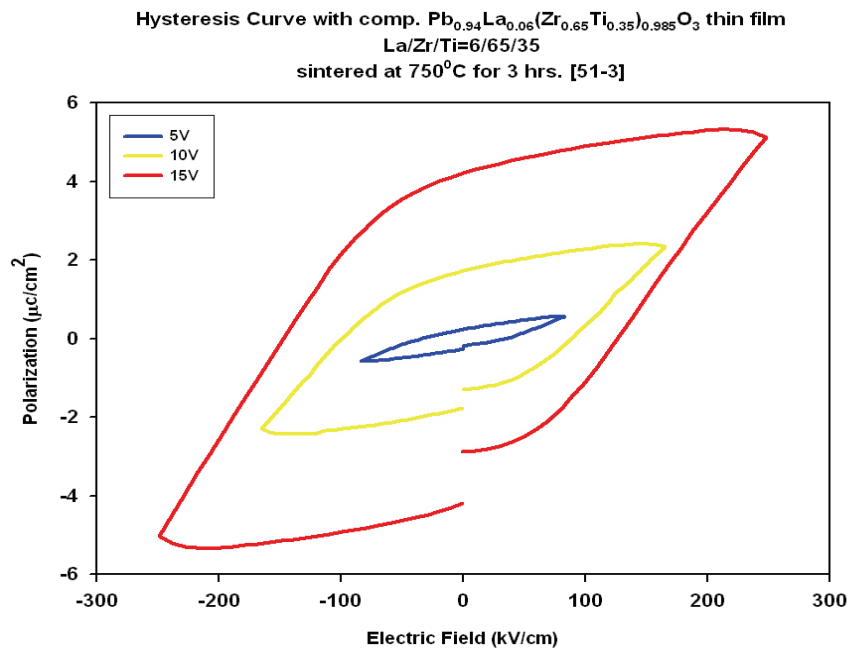


Fig. 4.43. Ferroelectric hysteresis loop of $\text{Pb}_{0.94}\text{La}_{0.06}(\text{Zr}_{0.65}\text{Ti}_{0.35})_{0.985}\text{O}_3$ thin film.

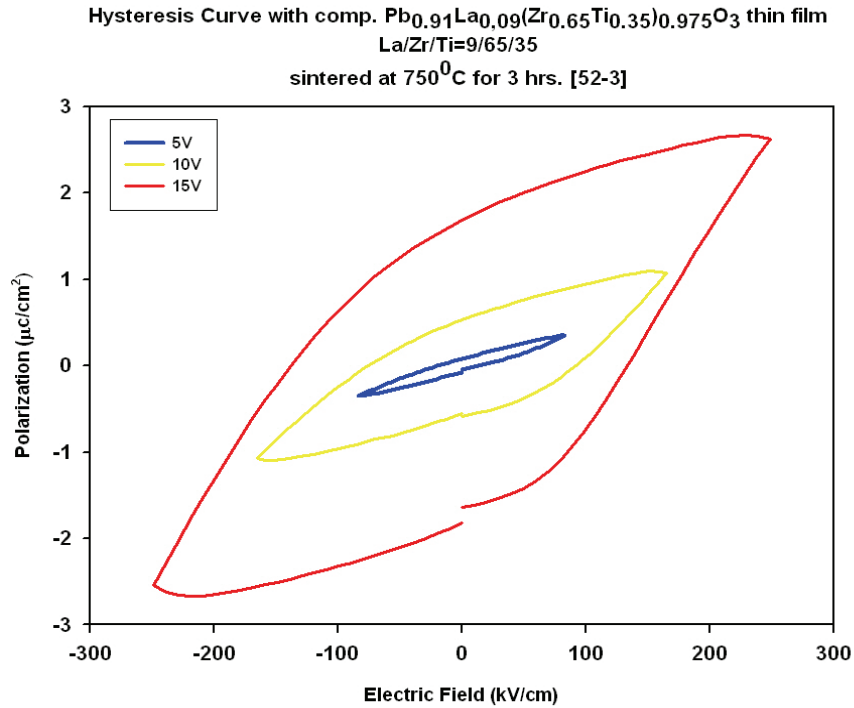


Fig. 4.44. Ferroelectric hysteresis loop of $\text{Pb}_{0.91}\text{La}_{0.09}(\text{Zr}_{0.65}\text{Ti}_{0.35})_{0.9775}\text{O}_3$ thin film.

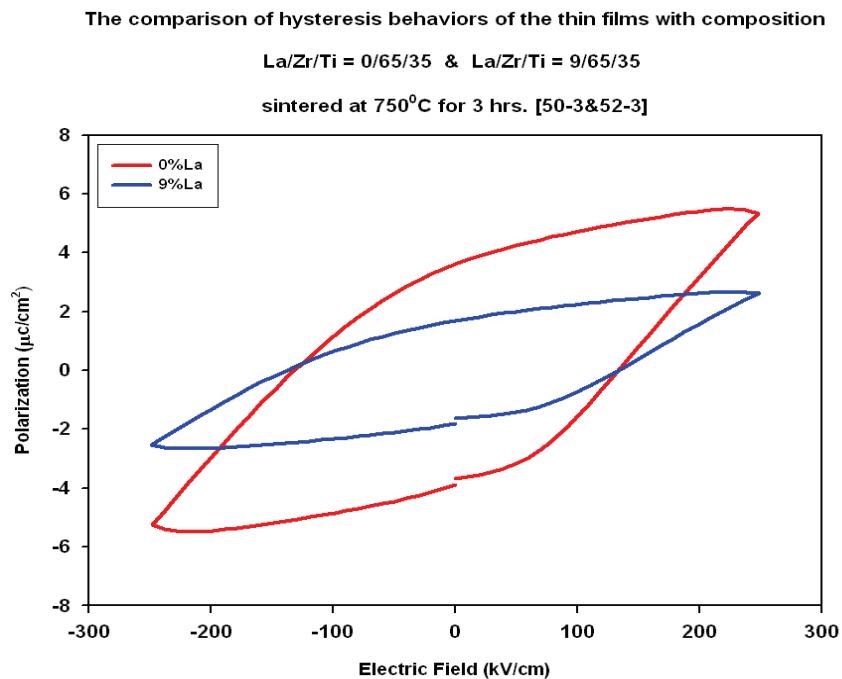


Fig. 4.45. Ferroelectric hysteresis loops of $(x/65/35)$ PLZT thin films with 0%La and 9%La obtained 15V.

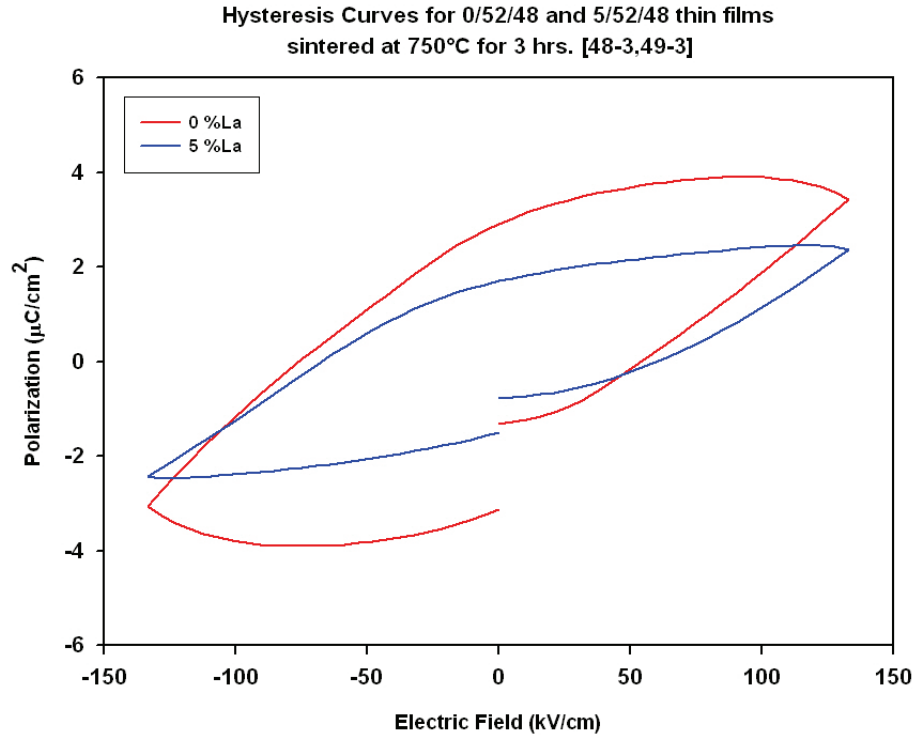


Fig. 4.46. Ferroelectric hysteresis loops of (x/52/48) PLZT thin films with 0%La and 5%La obtained 15V.

The ferroelectric hysteresis behavior of $\text{Pb}_{1-x}\text{La}_x(\text{Zr}_{0.4}\text{Ti}_{0.6})_{1-x/4}\text{O}_3$ thin films were different from those of $\text{Pb}_{1-x}\text{La}_x(\text{Zr}_{0.52}\text{Ti}_{0.48})_{1-x/4}\text{O}_3$ and $\text{Pb}_{1-x}\text{La}_x(\text{Zr}_{0.65}\text{Ti}_{0.35})_{1-x/4}\text{O}_3$ thin films. Unlike in the dielectric constant measurements, remanent polarization and coercive field values showed maximum values at 6 %La. Values of remanent polarization (P_r) and coercive field (E_c) are $11.0 \mu\text{C}/\text{cm}^2$ and $135 \text{ kV}/\text{cm}$ for the $\text{Pb}_{0.94}\text{La}_{0.06}(\text{Zr}_{0.4}\text{Ti}_{0.6})_{0.985}\text{O}_3$ thin film, respectively. After that point, polarization and coercive field starts decreasing with increase of La content till 24 at%La.

Figures 4.47-48-49-50-51-52 show the hysteresis loops of PLZT thin films having compositions from the tetragonal region to cubic region of PLZT phase diagram.

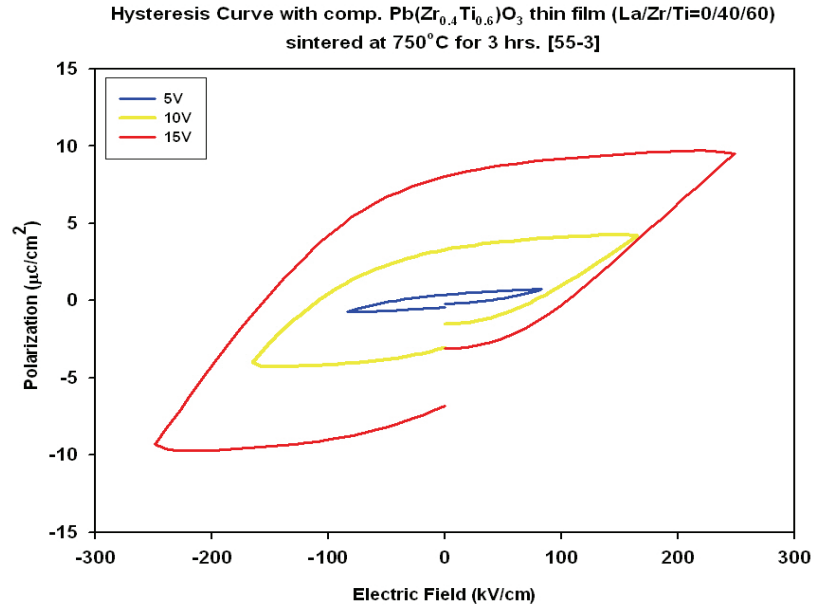


Fig. 4.47. Ferroelectric hysteresis loop of $\text{Pb}(\text{Zr}_{0.4}\text{Ti}_{0.6})\text{O}_3$ thin film.

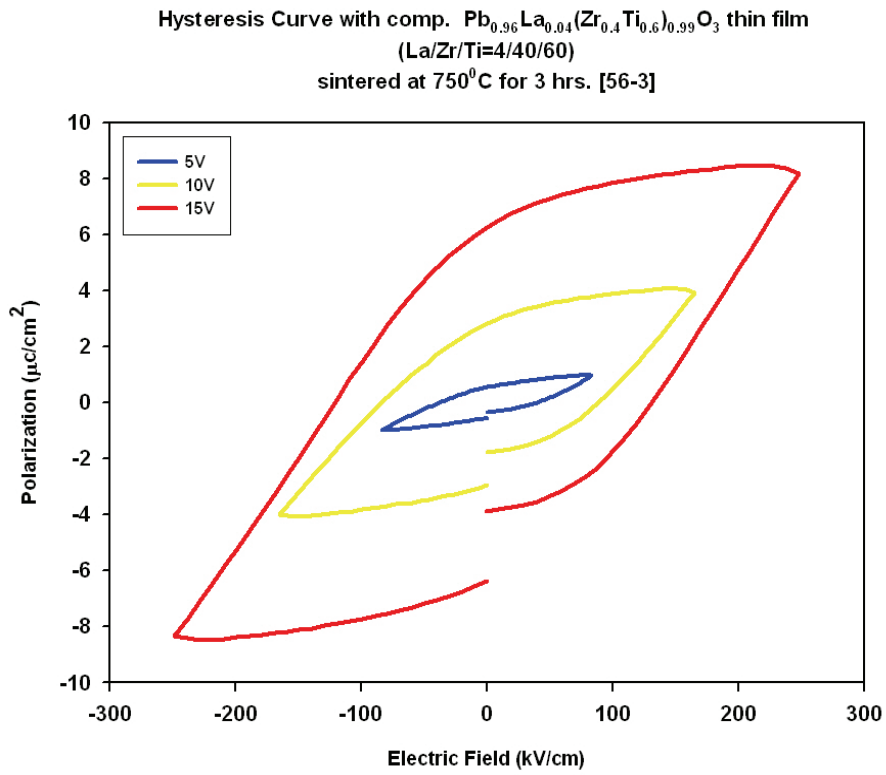


Fig. 4.48. Ferroelectric hysteresis loop of $\text{Pb}_{0.96}\text{La}_{0.04}(\text{Zr}_{0.4}\text{Ti}_{0.6})_{0.99}\text{O}_3$ thin film.

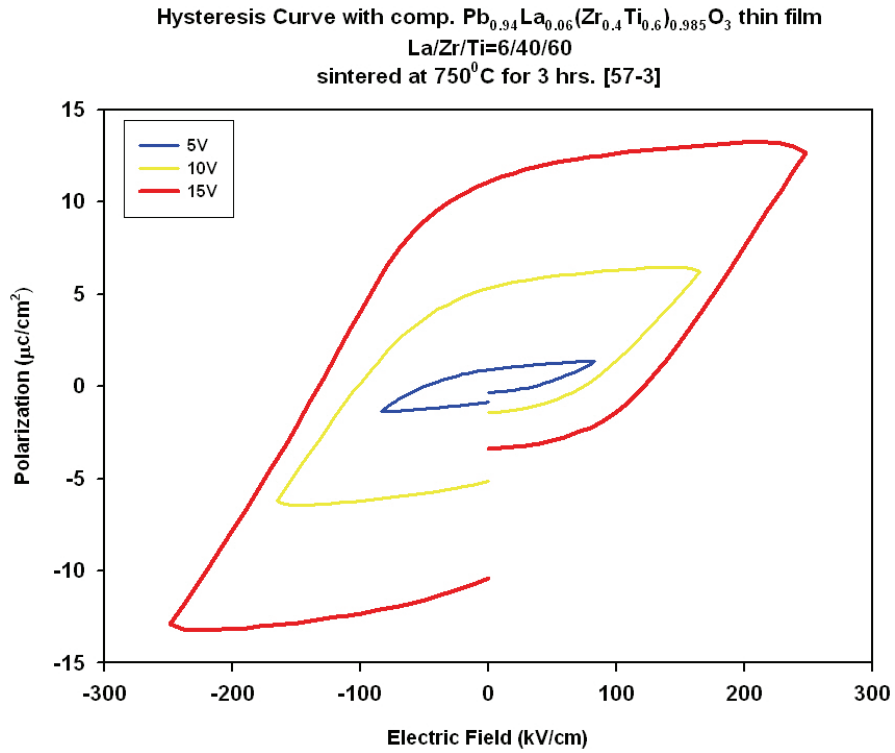


Fig. 4.49. Ferroelectric hysteresis loop of $\text{Pb}_{0.94}\text{La}_{0.06}(\text{Zr}_{0.4}\text{Ti}_{0.6})_{0.985}\text{O}_3$ thin film.

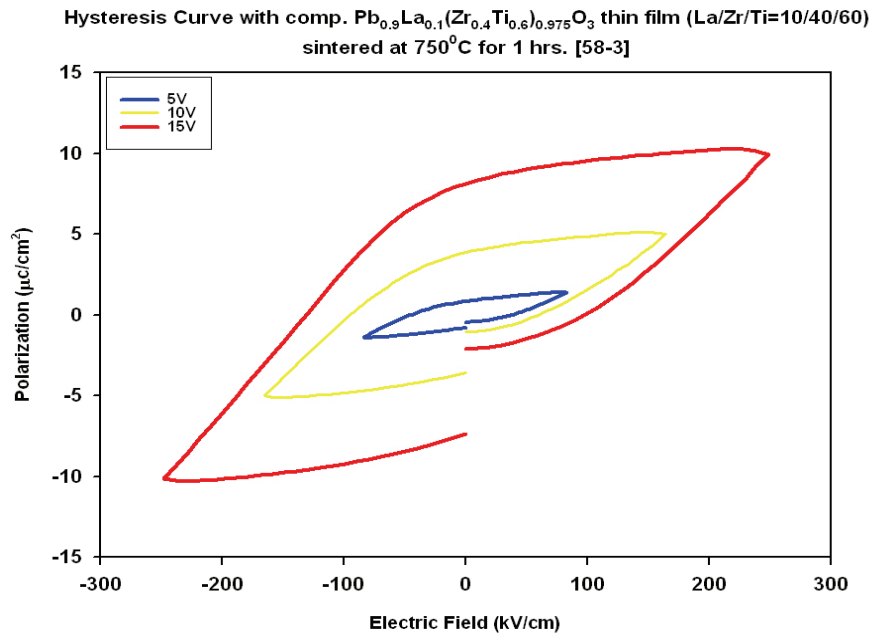


Fig. 4.50. Ferroelectric hysteresis loop of $\text{Pb}_{0.9}\text{La}_{0.1}(\text{Zr}_{0.4}\text{Ti}_{0.6})_{0.975}\text{O}_3$ thin film.

Hysteresis Curve with comp. $\text{Pb}_{0.96}\text{La}_{0.14}(\text{Zr}_{0.4}\text{Ti}_{0.6})_{0.965}\text{O}_3$ thin film (Pb/Zr/Ti=14/40/60) sintered at 750°C for 3 hrs. [59-3]

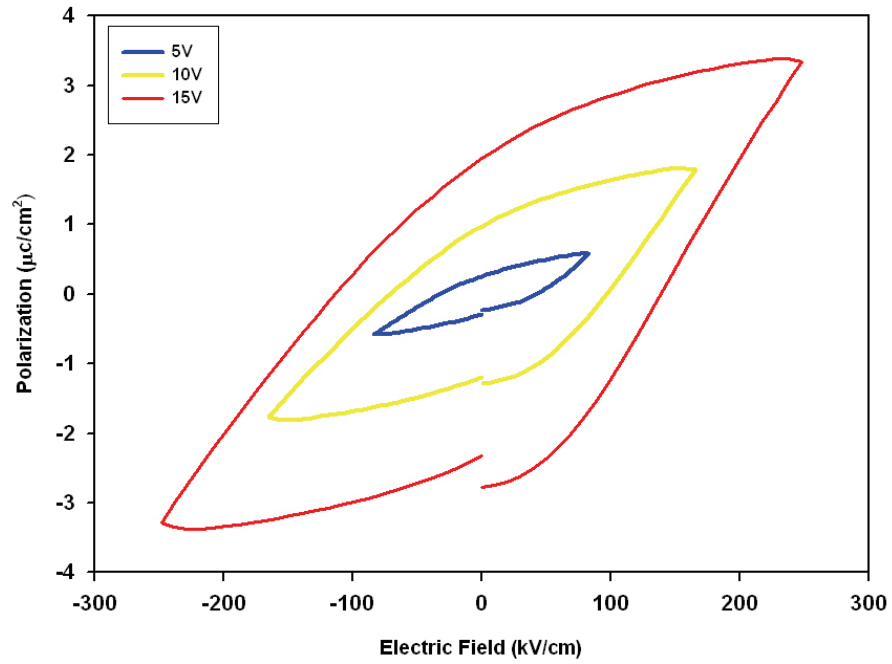


Fig. 4.51. Ferroelectric hysteresis loop of $\text{Pb}_{0.86}\text{La}_{0.14}(\text{Zr}_{0.4}\text{Ti}_{0.6})_{0.965}\text{O}_3$ thin film.

Hysteresis Curve with comp. $\text{Pb}_{0.76}\text{La}_{0.24}(\text{Zr}_{0.4}\text{Ti}_{0.6})_{0.94}\text{O}_3$ thin film (La/Zr/Ti=24/40/60) sintered at 750°C for 3 hrs. [60-3]

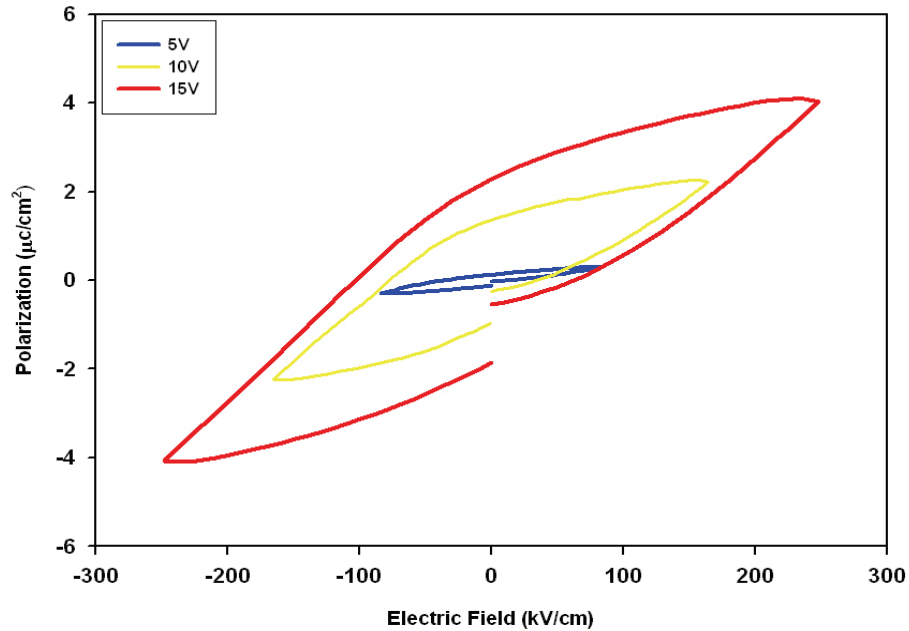


Fig. 4.52. Ferroelectric hysteresis loop of $\text{Pb}_{0.76}\text{La}_{0.24}(\text{Zr}_{0.4}\text{Ti}_{0.6})_{0.94}\text{O}_3$ thin film.

4.7. Optical Properties of PLZT Thin Films

PLZTs have been most widely known for their high optical transparency, broad range of compositions and various electro-optic coefficients. PLZTs are desirable candidates for electro-optic applications such as light shutters, modulators, color filters, memories and image storage devices [26].

In this study, optical transmission spectra of $\text{Pb}_{0.91}\text{La}_{0.09}(\text{Zr}_{0.65}\text{Ti}_{0.35})_{0.9775}\text{O}_3$ thin film was investigated by UV-VIS Spectrophotometer in the wavelength range of 200nm-800nm. From the transmittance (%) – wavelength (λ) curve, other optical parameters were found such as the refractive index (n), absorption coefficient (α) and extinction coefficient (k) by modified envelope method.

The modified envelope method, which includes the consideration of the light intensity loss from the back surface of the substrate, was developed and shown to be a simple and convenient tool for obtaining the optical properties and the thickness of the film by using the transmission spectra alone in the medium and weak absorption regions. In the near-optical band gap region, both the transmission and reflection spectra were used to calculate the optical constants of the films.

In a multi layer thin-film system, if the complex refractive index and thickness of each film layer are known, the reflectance (R) and transmittance (T) can be calculated exactly no matter how many layers are in the system or what the incident angle of the light is. All these quantities except the film thickness are wavelength-dependent. However, in practice, a reverse calculation is needed, i.e., the optical constants and thickness of the film (d) need to be calculated from the measured reflection and transmission spectra. There are only two measurable reflection and transmission spectra. There are only two measurable quantities, T and R, but $3m+2$ unknowns (three unknowns, n,k, and d, for each layer of m layer films and two unknowns, n and k, for the substrate) at a given wavelength and an incident angle. For a simple thin film system consisting of a single film on a substrate, there are still three unknowns for the film but two measured, T and R,

for a given wavelength and an incident angle, assuming the optical constants of the substrate are known. The difficulty of calculating the optical constants and the thickness of the film from T and R is not only that the number of unknowns is larger than the number of quantities one can measure, but also that the optical constants cannot be explicitly expressed in terms of T and R.

Fortunately, for a single layer weakly absorbing film on a transparent substrate, the refractive index and extinction coefficient as a function of wavelength and film thickness can be obtained from the transmission spectra alone. This method, which is referred to hereafter as the envelope method, was first presented by Manifacier et al. This is a very useful approach to study the optical properties of insulating films, since most of them are weakly absorbing materials [27].

Figure 4.53 shows the schematic diagram of a weakly absorbing thin film on a completely transparent substrate. Note that, for the original envelope method, the substrate is considered as semiinfinite. The refractive index of the ambient is n_0 ; n_s is the refractive index of the substrate; n , k , and d denote the refractive index, extinction coefficient, and the thickness of the film, respectively.

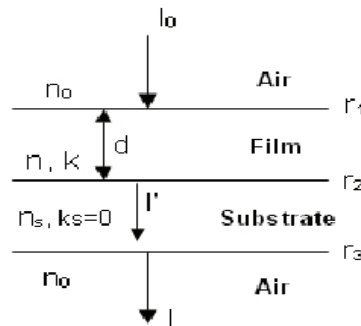


Fig. 4.53. Schematic diagram of the modified envelope method: a weakly absorbing thin film on a completely transparent finite substrate.

$$T = I / I_0 = (1 - r_3) I' / I_0 \quad \text{Eq. [4.2]}$$

The transmittance (T') of a single film on a transparent semi-infinite substrate can be expressed as:

$$T' = \frac{Ax}{B - Cx - Dx^2} \quad \text{Eq. [4.3]}$$

where $x = \exp(-\alpha d)$, Eq. [4.4]

$$A = 16n_0n_s(n^2 + k^2),$$

$$B = [(n_0 + n)^2 + k^2][(n + n_s)^2 + k^2],$$

$$C = 2[(n^2 - n_0^2 + k^2)(n^2 - n_s^2 + k^2) - 4k^2n_s] \cos(\psi) - 2[2kn_s(n^2 - n_0^2 + k^2) + 2k(n^2 - n_s^2 + k^2)] \sin(\psi),$$

$$D = [(n - n_0)^2 + k^2][(n - n_s)^2 + k^2],$$

α is the absorption coefficient of the film which is equal to $4\pi k / \lambda$, ψ is equal to $4\pi nd / \lambda$, d is the film thickness, k is the extinction coefficient of the film, and n_0 , n , and n_s are the refractive indices of the ambient (air), film, and substrate, respectively. Equation 4.3 is valid only if the film is homogeneous, the thickness of the film is uniform, and the substrate is semiinfinite and completely transparent, i.e. $k_s = 0$.

The equations describing the envelope method can be derived from Eq. [4.3] with further assumptions where the square of the refractive index of the film is much greater than that of extinction of the film, i.e., $n^2 \gg k^2$, and the square of the refractive index difference between the film and air and the film and the substrate is much greater than that of the extinction coefficient of the film, i.e., $(n - 1)^2 \gg k^2$ and $(n - n_s)^2 \gg k^2$. The first assumption leads to $A = 16n_0n^2n_s$, and $B = (n_0 + n)^2(n + n_s)^2$.

The second assumption leads to $C = [(n^2 - n_0^2)(n^2 - n_s^2)] \cos(\psi)$ and $D = (n - n_0)^2(n - n_s)^2$. With the above assumptions, Eq. [4.3] becomes

$$T' = \frac{16n_s n^2 x}{(1 + n)^2(n + n_s)^2 - 2x[(n^2 - 1)(n^2 - n_s^2)] \cos(\psi) + (n - 1)^2(n - n_s)^2 x^2} \quad \text{Eq. [4.5]}$$

Here 1 is used to replace n_0 , which is refractive index of air, and $\gamma = 4\pi nd / \lambda$. The cosine function in the denominator oscillates between +1 and -1, which results in the well-known equation for the interference fringes in the transmission spectrum:

$$2nd = m\lambda \quad \text{Eq. [4.6]}$$

where the order number m is an integer for maxima and a half-integer for minima. Equation [4.5] gives the top envelope equation for $\cos(\gamma)=1$ as

$$T'_{\max} = \frac{16n_s n^2 x}{[(1+n)(n+n_s) - (n-1)(n-n_s)x]^2} \quad \text{Eq. [4.7]}$$

Whereas, for $\cos(\gamma) = -1$, the bottom envelope equation becomes

$$T'_{\min} = \frac{16n_s n^2 x}{[(1+n)(n+n_s) + (n-1)(n-n_s)x]^2} \quad \text{Eq. [4.8]}$$

Equations [4.7] and [4.8] can be solved for n and x , giving

$$x = \frac{(n+1)(n+n_s)[(T'_{\max}/T'_{\min})^{0.5} - 1]}{(n-1)(n-n_s)[(T'_{\max}/T'_{\min})^{0.5} + 1]} \quad \text{Eq. [4.9]}$$

$$n = [N' + (N'^2 - n_s^2)^{0.5}]^{0.5} \quad \text{Eq. [4.10]}$$

where
$$N' = \frac{1}{2}(1+n_s^2) + 2n_s(T'_{\max} - T'_{\min})/(T'_{\max}T'_{\min}) \quad \text{Eq. [4.11]}$$

Once T'_{\max} and T'_{\min} are obtained from the measured transmission spectrum and the refractive index of the substrate is known, the refractive index of the film can be calculated as a function of wavelength using Eq. [4.10].

Moreover, the extinction coefficient (k) and absorption coefficient (α) of the film can be calculated by Eq. [4.9], Eq. [4.4] and the relation $\alpha = 4\pi k / \lambda$.

Figure 4.54 shows the transmission spectra of PLZT- $\text{Pb}_{0.91}\text{La}_{0.09}(\text{Zr}_{0.65}\text{Ti}_{0.35})_{0.9775}\text{O}_3$ thin film sintered at 750°C for 3 hours.

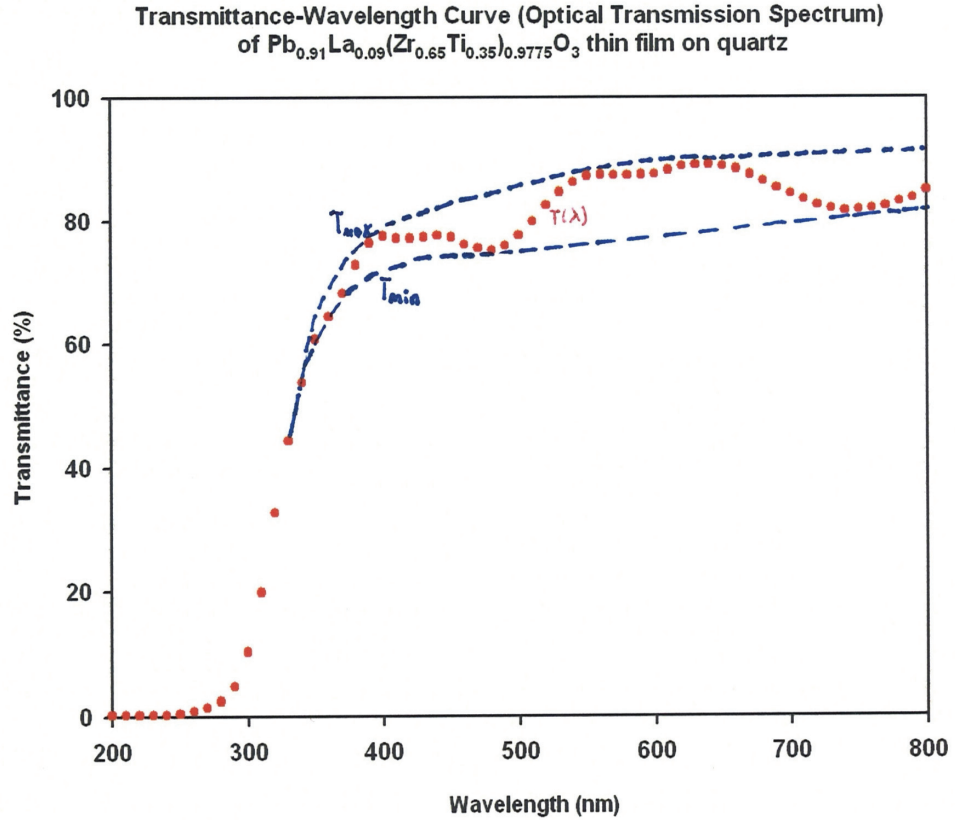


Fig. 4.54. Optical transmission spectra of PLZT thin film on quartz.

It can be seen from the curves above that the red one is the transmission spectra of the film and the other blue ones are the T_{\max} and T_{\min} curves drawn from the maxima and minima of the interference fringes, respectively.

From the optical parameters of T_{\max} , T_{\min} and n_s which are known for the 630 nm wavelength which is the wavelength of a He-Ne laser, the other parameter the refractive index of the film was found as 1.96.

For this calculation, Fig. 4.55 was used to obtain the value of refractive index of the quartz substrate at 630 nm wavelength value. Fig. 4.55 was obtained by using the formula [28]:

$$n^2 = 3.4629 + 0.010654/(\lambda^2 - 0.010627) + 111.47/(\lambda^2 - 100.8) \quad \text{Eq. [4.12]}$$

where n is the refractive index of quartz and λ is the wavelength in μm .

If $n(\lambda_1)$ and $n(\lambda_2)$ are the refractive indices at two adjacent maxima (or minima), at λ_1 and λ_2 , it follows that the film thickness is given by the expression:

$$d = \frac{\lambda_1 \lambda_2}{2[n(\lambda_1)\lambda_2 - n(\lambda_2)\lambda_1]} \quad \text{Eq. [4.13]}$$

From that formula, the thickness of the PLZT film was found about 335 nm which was nearly the same thickness for single layer investigated by cross-section analysis obtained by SEM.

Other optical constants of the films were found by using the equations above where absorption coefficient was found by using Eq. [4.4] and Eq. [4.9] as $1.85 \cdot 10^{-4}$ 1/nm. The extinction coefficient was calculated as 0.0093.

Table 4.8. Optical properties of 9/65/35 PLZT thin film sintered at 750 °C for 3 hours.

Composition	Thickness (nm)	Refractive index (n)	Absorption coefficient (α) (1/nm)	Extinction coefficient (k)
$\text{Pb}_{0.91}\text{La}_{0.09}(\text{Zr}_{0.65}\text{Ti}_{0.35})_{0.9775}\text{O}_3$	335	1.96	$1.85 \cdot 10^{-4}$	0.0093

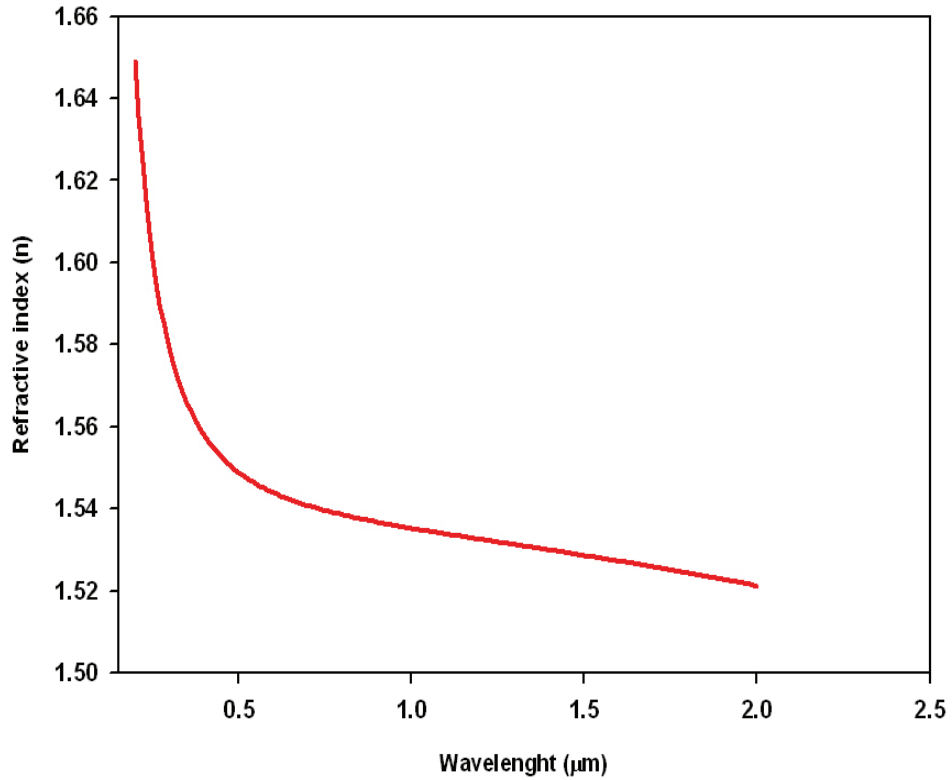


Fig. 4.55. Refractive index-wavelength curve of the quartz substrate.

The band gaps energy (E_g) can be estimated by assuming a direct transition between valance and conduction bands. The absorption coefficient α as a function of photon energy can be expressed as :

$$(\alpha h\nu)^2 = C(h\nu - E_g) \quad \text{Eq. [4.14]}$$

where $h\nu$ is the incident photon energy and C is a constant, which does not depend on photon energy.

The dependence of $(\alpha h\nu)^2$ as a function of the photon energy ($h\nu$), indicates the direct nature of fundamental band-to-band transitions. Figure 4.56 shows the $(\alpha h\nu)^2$ vs. $(h\nu)$ plotted for PLZT-Pb_{0.91}La_{0.09}(Zr_{0.65}Ti_{0.35})_{0.9775}O₃ thin film sintered at 750 °C for 3 hours.

A linear behavior exist in a certain range, thus supporting the assumption of a direct transition. The band gaps E_g of the films can be obtained by extrapolating the linear portion of plot relation $(\alpha h\nu)^2$ vs. $(h\nu)$ to $(\alpha h\nu)^2 = 0$. The value of the band gap energy was found to be 3.1 eV.

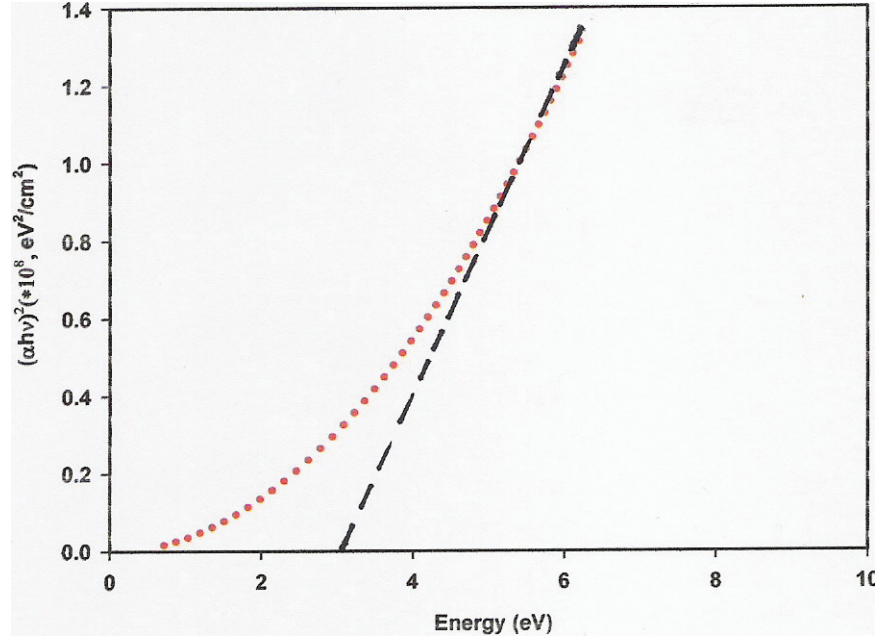


Fig. 4.56. Plot of $(\alpha h\nu)^2$ versus photon energy.

4.8. Ferroelectric Fatigue Analysis of PLZT Thin Films

Ferroelectric fatigue curves of the PLZT thin films were drawn at 50 kHz and ± 15 V bias voltage. The films were fatigued up to 3.5×10^9 cycles by bipolar switching pulses. Figure 4.56 shows the fatigue curve of PLZT thin film. During the fatigue process, positively charged oxygen vacancies move only in one direction -to the bottom electrode- because of the internal field formed from the top to the bottom electrode. Therefore, the oxygen vacancies make a layer between the bottom electrode and the films. Because of the oxygen vacancy layer, the total applied voltage is divided into two parts. Since voltage is divided, measured polarization must decrease after long period of cycles [29]. In the film we studied, the remanent polarization started to decrease after 10^9 cycles.

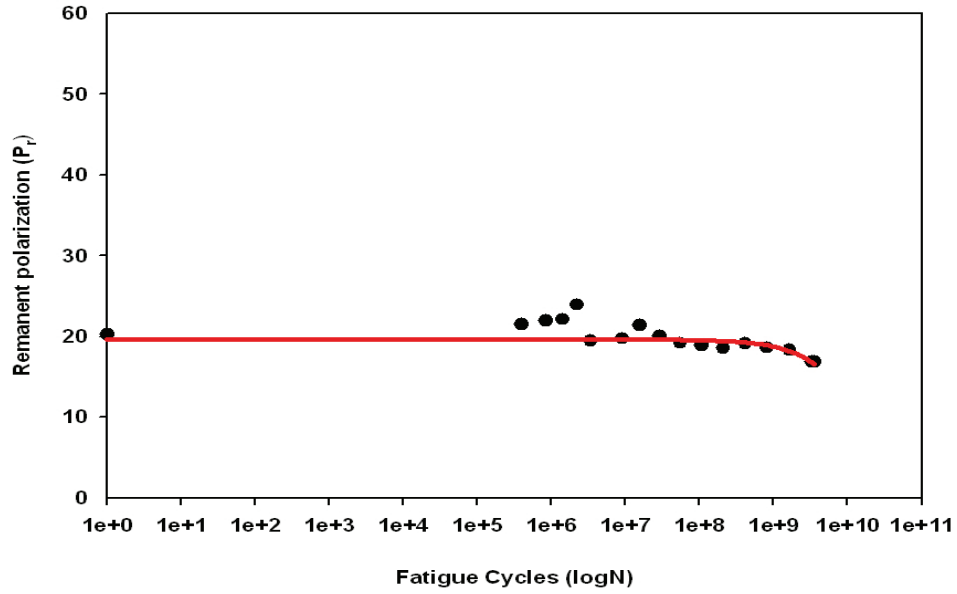


Fig. 4.57. Fatigue Curve of 600 nm thick $\text{Pb}_{0.96}\text{La}_{0.04}(\text{Zr}_{0.4}\text{Ti}_{0.6})_{0.99}\text{O}_3$ thin film sintered at 750°C for 3 hours.

4.9. Leakage Current Analysis of PLZT Thin Films

The influence of La-doping on the current density versus electric field (J-E) characteristics of PLZT is shown in Figures 4.57-58 drawn at $\pm 15\text{V}$. Figure 4.57 shows the PLZT thin films with the composition of $\text{Pb}_{0.94}\text{La}_{0.06}(\text{Zr}_{0.4}\text{Ti}_{0.6})_{0.985}\text{O}_3$ having 6 %La. When the La content was increased from 6 %La to 10 %La shown in Figure 4.58, the leakage current of the films reduced.

It was mentioned in the literature that the leakage current occurs in the thin films because of thermionic emissions from Pt contacts to the films.

At high electric field, the Schottky equation can be used to analyse the leakage current data. The current density J is then expressed as:

$$J = A * T^2 \exp\left(\frac{-q(\Phi_B - \sqrt{qE / 4\pi\epsilon_0\epsilon})}{kT}\right) \quad \text{Eq. [4.14]}$$

where A^* is the Richardson constant, T the absolute temperature, E the applied electric field, Φ_B is the Schottky barrier height at the Pt electrode, q the electronic charge, ϵ_0 the permittivity of free space, ϵ the optical dielectric constant, and k the Boltzmann constant. If the conduction current at high electric field is governed by Schottky emission, the $\log J$ versus $E^{1/2}$ plot, should therefore, be a straight line and the slope will give the optical dielectric constant.

PLZT thin films generally contain oxygen vacancies and free electrons in the film itself. Excess oxygen vacancies created by La^{3+} addition can combine the free electron. In this way, La doping results in the decrease of electron concentration of PZT thin films. The decrease of electron concentration can result in an increase of barrier height to thermionic emissions of electrons from the Pt contacts. The increased barrier height makes it difficult for electrons to transfer from the Pt electrode into the PLZT film [30].

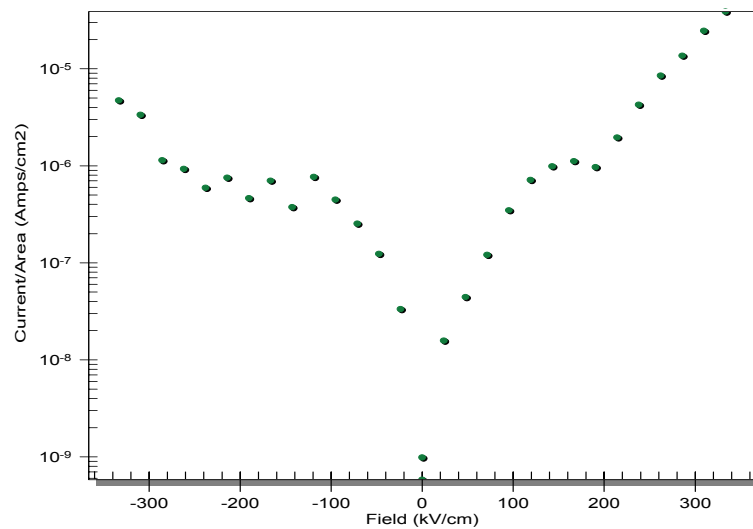


Fig. 4.58. Leakage Current Curve (J-E) for 600 nm thick La:Zr:Ti=6/40/60 thin film sintered at 750 °C for 3 hours.

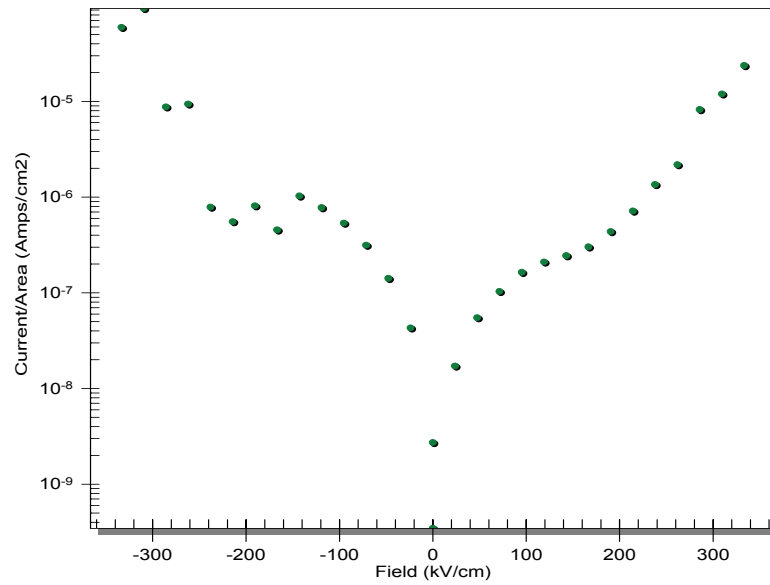


Fig. 4.59. Leakage Current Curve (J-E) for 600 nm thick La:Zr:Ti=10/40/60 thin film sintered at 750 °C for 3 hours

For the PLZT thin film with composition of $\text{Pb}_{0.94}\text{La}_{0.06}(\text{Zr}_{0.4}\text{Ti}_{0.6})_{0.985}\text{O}_3$ the leakage current is 10^{-6} A/cm^2 at 200 kV/cm. When the composition became $\text{Pb}_{0.94}\text{La}_{0.06}(\text{Zr}_{0.4}\text{Ti}_{0.6})_{0.985}\text{O}_3$ having 10 %La, the leakage current decreased to $5 \times 10^{-7} \text{ A/cm}^2$.

CHAPTER 5

CONCLUSIONS AND FURTHER SUGGESTIONS

In this study, lanthanum substituted PZT (PLZT) thin films were produced by chemical solution deposition (CSD) on Pt/Ti/SiO₂/Si substrate. For the optimization of the microstructural and electrical investigations, different process parameters such as sintering temperature and time, composition, thickness of the film and precursors were considered as important variables.

Homogeneous and crack-free PLZT thin films were produced via sol-gel processing. In the spin coating process, substrates were coated with PLZT solutions by 3000 rpm spinning speed for 30 seconds. By using these values, it was reached 300 nm thickness for one layer coating. For 2 layers it was about 450 nm, 4 layers-600 nm, 6 layers-700 nm and 8 layers 1.14 μm .

The PLZT solutions were prepared 0.4M/40 ml. They were stock for a few months. 2- methoxyethanol was used as solvent for most of compositions. For the compositions having high La content, acetic acid was used for dissolving La in the solutions because 2-methoxyehanol were not strong enough to make a clear solution having high amount of lanthanum. 2-methoxyethanol played an important role in the production of crack-free samples. There was no need to dilute the solution with an alcohol such as 2-propanol or ethylene glycol.

X-Ray diffraction analysis showed that as the sintering temperature was increased, the intensities of perovskite phases increased. At lower temperatures, pyrochlore phases such as TiO and Ti₃O₅ emerged, however, it disappeared when the sintering temperature was increased to 750⁰C. Lanthanum addition resulted in decrease of perovskite intensities because it lowers the crystallization kinetics.

From the X-Ray diffraction results, grain sizes of the films were measured. It was investigated that as the sintering temperature was increased, the grain size also increased. Furthermore, La was very effective on grain coarsening in that as La content was raised, grain size of the PLZT films increased at the same time.

Dielectric constant of the films increased with increasing sintering temperature from 600 °C to 750 °C because of better crystallinity at higher temperatures. The dielectric and tangent loss measurements were done at frequencies between 1kHz-1MHz. Among these values, dielectric properties were almost constant. This indicates that these films are useable between this frequency range.

Dielectric properties of the films were also investigated as a function of composition. $Pb_{1-x}La_x(Zr_{0.4}Ti_{0.6})_{1-x/4}O_3$, $Pb_{1-x}La_x(Zr_{0.65}Ti_{0.35})_{1-x/4}O_3$ and $Pb_{1-x}La_x(Zr_{0.52}Ti_{0.48})_{1-x/4}O_3$ thin films were investigated by electrically with the change of La content. For the x/52/48 and x/65/35 films, the dielectric constant of the films decreased as La content was increased. For the $Pb(Zr_{0.65}Ti_{0.35})O_3$ and $Pb(Zr_{0.52}Ti_{0.48})O_3$ thin films, the dielectric constants were found to be 268 and 431 at 1 kHz, respectively. When the compositions were La:Zr:Ti=9/65/35 and La:Zr:Ti=5/52/48, these dielectric constants were measured as 146 and 230, respectively. For the thin films with $Pb_{1-x}La_x(Zr_{0.4}Ti_{0.6})_{1-x/4}O_3$ compositions, situation was different. Dielectric constant values showed a peak value as the La was grown up. For the film in the region between tetragonal and cubic having a composition of $Pb_{0.9}La_{0.1}(Zr_{0.4}Ti_{0.6})_{0.975}O_3$, dielectric constant was 287 at 1kHz as the maximum point.

C-V curves of PLZT films showed typical behavior, where capacitance decreased with increasing bias voltage. Butterfly shaped C-V curve indicates the ferroelectric behavior of the film.

Ferroelectric properties of PLZT thin films such as remanent polarization (P_r) and coercive field (E_c) were investigated as a function of sintering temperature. Remanent polarization of the thin films were $0.56 \mu\text{C}/\text{cm}^2$,

6.194 $\mu\text{C}/\text{cm}^2$, 6.94 $\mu\text{C}/\text{cm}^2$ and 10.49 $\mu\text{C}/\text{cm}^2$ as the sintering temperatures were 600 $^{\circ}\text{C}$, 650 $^{\circ}\text{C}$, 700 $^{\circ}\text{C}$ and 750 $^{\circ}\text{C}$, respectively. Coercive field values showed the same tendency in that they were measured as 108 kV/cm, 128.2 kV/cm, 129 kV/cm and 131 kV/cm for the sintering temperatures 600 $^{\circ}\text{C}$, 650 $^{\circ}\text{C}$, 700 $^{\circ}\text{C}$ and 750 $^{\circ}\text{C}$, respectively.

The compositional change of ferroelectric properties are similar to dielectric properties. Remanent polarization showed a peak value then decreased while lanthanum content was increased in the tetragonal region of the PLZT phase diagram. For the other two crystal structure rhombohedral and on the morphotropic phase boundary, slim hysteresis loops were obtained.

In order to better ferroelectric and dielectric properties, clean room conditions should be obtained and for the preparation of solutions glove box should be used. Furthermore, rapid thermal annealing (RTA) could be very effective in order to get better results because it reduces the interfacial layer formed between the film and substrate.

Optical properties of PLZT thin films on quartz substrate were obtained by using UV-VIS spectrophotometer. Many optical constants were measured by the modified envelope method. The refractive index of the 9/65/35 PLZT thin film was 1.96, the extinction coefficient was measured as 0.0093 and absorption coefficient was 1.85×10^{-4} (1/nm). The thickness of the film was also calculated as 335 nm which was nearly the same for one layer thin film measured by cross-section view of SEM picture. Band gap energy of the film was found as 3.1 eV.

The leakage current analysis showed a decrease in leakage current upon increase in La content of the film. The leakage current of the PLZT thin films in this study is higher than the values in the literature. That can be a reason of high dielectric loss in the films.

For better dielectric and ferroelectric properties, contact electrode should be coated carefully. It should be coated by sputter technique in vacuum or any

other technique by which very thin contact layer could be obtained. Contact diameter should be as small as possible because as it decreases, better dielectric constant and polarization values are obtained.

For the improvement of fatigue properties, oxide electrodes should be used because they act as sinks for oxygen vacancies.

REFERENCES

- [1] M Daglish, T Kemmitt, "Ferroelectric thin films-research, development and commercialisation", IPENZ Transactions, Vol. 27, No. 1/Gen, (2000).
- [2] A.K. Tripathi, T.C. Goel, Chandra Prakash, "Preparation of 4:55:45 samarium doped PZT films by sol-gel technique and their characterization", Materials Science and Engineering, Vol. B96, pp. 19-23, (2002).
- [3] Chuanbao Cao, Ming Luo, Hesun Zhu, "PLZT films prepared by sol-gel process", Journal of Non-Crystalline Solids, Vol. 254, pp. 146-150, (1999).
- [4] C. Vijayaraghavan, T.C. Goel and R.G. Mendiratta, "Structural and Electrical Properties of Sol-Gel Synthesized PLZT Thin Films", IEEE Transactions on Dielectrics and Electrical Insulation, Vol. 6, No.1, pp. 69-72, (1999).
- [5] Ceramic Materials for Electronics, Edited by R.C. Buchanan, Markel Dekker, Inc., New York, (1991).
- [6] Koon-Kim Jeremy Wong, "Optical Metrology and Application of a PLZT Lens", M.S. Thesis, The University of Alabama, (2001).
- [7] Dragan Damjanovic, "Ferroelectric, Dielectric and Piezoelectric Properties of Ferroelectric Thin Films and Ceramics", Rep. Prog. Phys. 61, pp 1267-1324, (1998).
- [8] Dielectric Materials and Applications, Edited by Arthur R. Von Hippel, pp. 19, (1954).

- [9] D.V. Kulikov, YU. V. Trushin, “Theoretical study of Ferroelectric Properties Degredation in Perovskite Ferroelectrics and Antiferroelectrics under Neutron Irradiation”, Ferroelectrics, Vol. 308, p.p. 5-16, (2004).
- [10] Bahadır Tunaboğlu, “Synthesis, Deposition and Characterization of Ferroelectric Films for Electrooptic Devices”, Ph.D. Thesis, University of California, San Diego, (1997).
- [11] Introduction to Sol-Gel Processing, by Alain C. Pierre, Kluwer Academic Publishers, (2002).
- [12] İ.A. Aksay, W.Y. Shih, M. Sarıkaya, “In Ultrastructure Processing of Advanced Ceramics”, Edited by J.D. Mackenzie and D.R. Ulrich, Wiley, New York, p.p. 393, (1988).
- [13] R.C. Mehrotra, Journal of Non-Crystalline Solids, Vol. 121, pp. 1-6, (1990).
- [14] Sol-Gel Science, C. Jeffrey Brinker, p.p. 547, (1993).
- [15] Brian D. Fabes, Brian J.J. Zelinski, Ronald R. Uhlman, “Sol-Gel Derived Ceramic Coatings”, in Ceramic Films and Coatings, Edited by John B. Wachtman, Richard A. Haber, Noyes Publications, Park Ridge, NJ, USA, (1993).
- [16] Ege İzgi, “Characterization of Superconducting Bi-Sr-Ca-Cu-O System Prepared by Sol-Gel Processing”, M.S. Thesis, Middle East Technical University, Ankara-Turkey, (1996).
- [17] D.E. Bornside, C.W. Macosco, L.E. Scriven, Journal of Imaging Technology, Vol.13, p.p. 122-129, (1987).

- [18] Faruk Altan Yıldırım, “PZT Films on Stainless Steel by Chemical Solution Deposition”, M.S. Thesis, Middle East Technical University, Ankara-Turkey, (2002).
- [19] Reji Thomas, Shoichi Mochizuki, Toshiyuki Mihara, Tadashi Ishida,” PZT (65/35) and PLZT (8/65/35) thin films by sol-gel process: a comparative study on the structural , microstructural and electrical properties”, Thin Solid Films, Vol. 443, p.p.14-22, (2003).
- [20] Kenji Kitaoka, Hiromitsu Kozuka, Toshinobu Yoko, “Preparation of Lead Lanthanum Zirconate Titanate (PLZT, (Pb,La)(Zr,Ti)O₃) Fibers by Sol-Gel Method”, Journal of American Ceramic Society, Vol. 81 [5], 1189-1196, (1998).
- [21] M. Es-Souni, M. Abed, A. Piorra, S. Malinowski, V. Zapporojtchenko, “Microstructure and properties of sol-gel processed Pb_{1-x} La_x (Zr_{0.52}, Ti_{0.48})_{1-x/4}O₃ thin films. The lanthanum content and bottom electrodes”, Thin Solid Films, Vol. 389, p.p. 99-107, (2001).
- [22] X.G. Tang, A.L. Ding, Y. Ye, W.X. Chen , “ Preparation and characterization of highly (111) oriented (Pb,La) (Zr, Ti) O₃”, Thin Solid Films, Vol. 423, p.p. 13-17, (2003).
- [23] M. Es-Souni, M. Abed, C.-H. Solterbeck, A. Piorra, “Crystallization kinetics and dielectric properties of solution deposited, La doped PZT thin films”, Materials Science and Engineering, B94, p.p. 229-236, (2002).
- [24] Umut Adem, “Preparation of Ba_xSr_{1-x}TiO₃ Thin Films by Chemical Solution Deposition and Their Electrical Characterization”, M.S. Thesis, Middle East Technical University, Ankara-Turkey, (2003).

- [25] J. H. Jung, B. G. Chae, H. J. Joo, J. P. Kim, S. H. Lee, Y. D. Kim, M. S. Jang, "Phase Formation and Switching Kinetics of Sol-Gel Derived ($\text{Pb}_{0.97}$, $\text{La}_{0.03}$) (Zr_y , Ti_{1-y}) O_3 Thin Films", Journal of the Korean Physical Society, Vol. 35, p.p. 1163-1167, (1999).
- [26] Hyung-Wook Choi, Yong Seo Park, J. Dougherty, Nak Won Jang, "Electrical and optical properties of PLZT thin films on ITO coated glass by sol-gel processing", Journal of Material Science, Vol. 35, p.p. 1475-1479, (2000).
- [27] Chien H. Peng, Seshu B. Desu, "Modified Envelope Method for Obtaining Optical Properties of Weakly Absorbing Thin Films and Its Application to Thin Films of $\text{Pb}(\text{Zr},\text{Ti})\text{O}_3$ Solid Solutions", Journal of American Ceramic Society, Vol. 77, No. 4, p.p. 929-938, (1994).
- [28] S.A Korff, G. Breit, "Optical Dispersion", Reviews of Modern Physics, Vol. 4, No. 3, p.p. 471-503, (1932).
- [29] Byung Gyu Chae, Su Jae Lee, Yong Suk Yang, Seong Hyun Kim, Min Su Jang, "Fatigue and Refresh Characteristics of $\text{Pb}(\text{Zr}_{0.52}\text{Ti}_{0.48})\text{O}_3$ Thin Films", Journal of the Korean Physical Society, Vol. 31, No. 6, p.p. 874-878, (1997).
- [30] S. Y. Wang, B. L. Cheng, Can Wang, S. A. T. Redfern, S. Y. Dai, K. J. Jin, H. B. Lu, Y. L. Zhou, Z. H. Chen and G. Z. Yang, "Influence of Ce doping on leakage current in $\text{Ba}_{0.5}\text{Sr}_{0.5}\text{TiO}_3$ films", Journal of Physics D: Applied Physics, Vol. 38, p.p. 2253-2257, (2005).
- [31] A. Khodorov, M. Pereira, M. J. M. Gomes, "Structure and dielectric properties of sol-gel 9/65/35 PLZT thin films", Journal of the European Ceramic Society, Vol. 25, p.p. 2285-2288, (2005).

- [32] Woo Sik Kim, Soon-Mok Ha, Hyung-Ho Park, Chang Eun Kim, "The effects of cation substitution on the ferroelectric properties of sol-gel derived PZT thin film for FRAM application", Thin Solid Films, 355-356, p.p. 531-532, (1999).
- [33] R. Kurchania, S. J. Milne, "Synthesis of (Pb,La) (Zr,Ti) O₃ films using a diol based sol-gel route", Journal of Material Science, Vol. 33, p.p. 659-667, (1998).
- [34] S. B. Mah, N. W. Jang, J. H. Park, D. S. Paik, C. Y. Park, "Structural and electrical characteristics of (Pb_{1-x}La_x) (Zr_{0.5} Ti_{0.5}) O₃ thin film capacitors", Materials Research Bulletin, Vol. 35, p.p. 1113-1122, (2000).
- [35] T.J. Boyle, H.N. Al-Shareef, "A new and rapid process for production of solution-derived (Pb,La) (Zr,Ti)O₃ thin films and powders", Journal of Materials Science, Vol. 32, 2263-2266, (1997).

APPENDIX-A

CAPACITANCE-FREQUENCY AND FERROELECTRIC HYSTERESIS CURVES

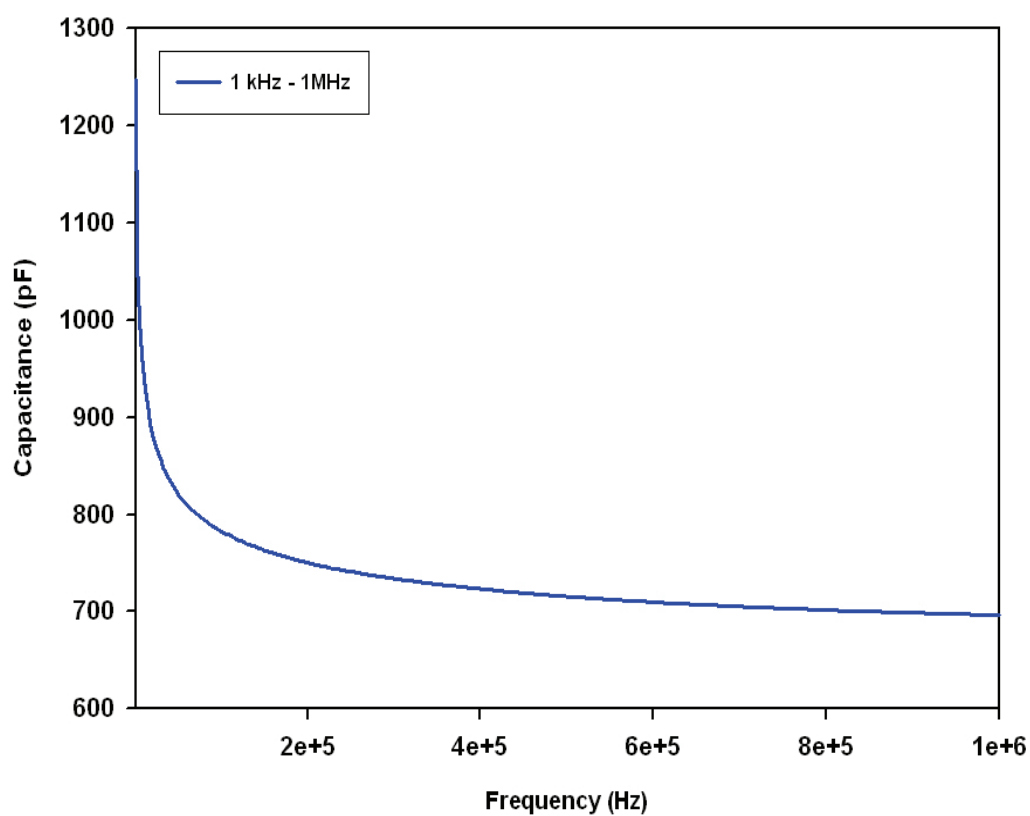


Fig. A-1. Capacitance-Frequency Curve for Pb(Zr_{0.52}Ti_{0.48})O₃ thin film sintered at 750 °C for 3 hours. (at 1 kHz C=1250 pF) [48-3]

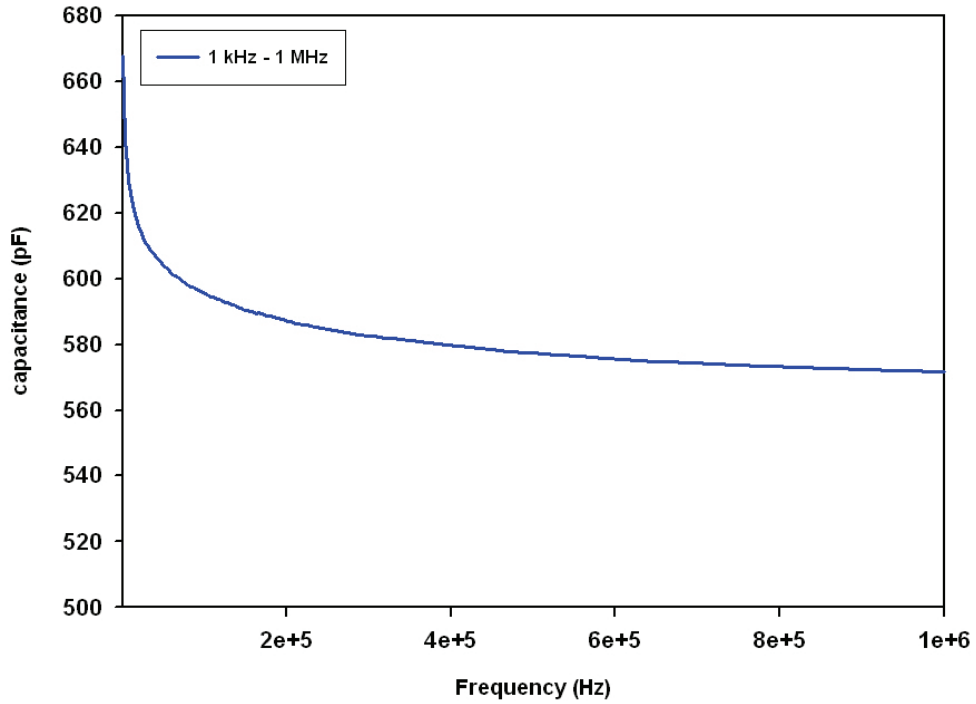


Fig. A-2. Capacitance-Frequency Curve for $\text{Pb}_{0.95}\text{La}_{0.05}(\text{Zr}_{0.52}\text{Ti}_{0.48})_{0.9875}\text{O}_3$ thin film sintered at 750°C for 3 hours. (at 1 kHz $C=668$ pF) [49-3]

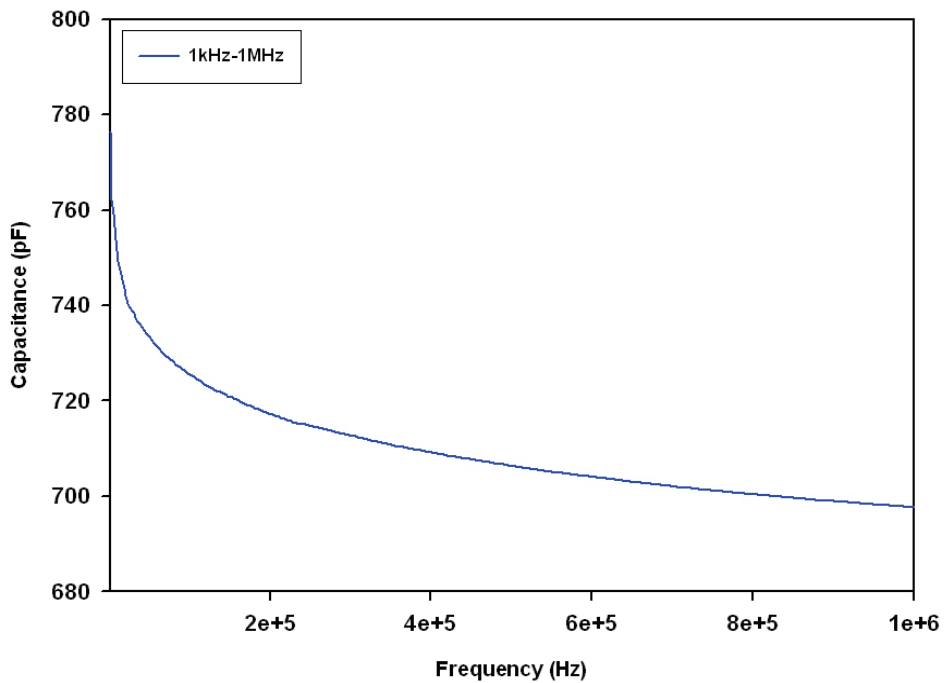


Fig. A-3. Capacitance-Frequency Curve for $\text{Pb}(\text{Zr}_{0.65}\text{Ti}_{0.35})\text{O}_3$ thin film sintered at 750°C for 3 hours. (at 1 kHz $C=776$ pF) [50-3]

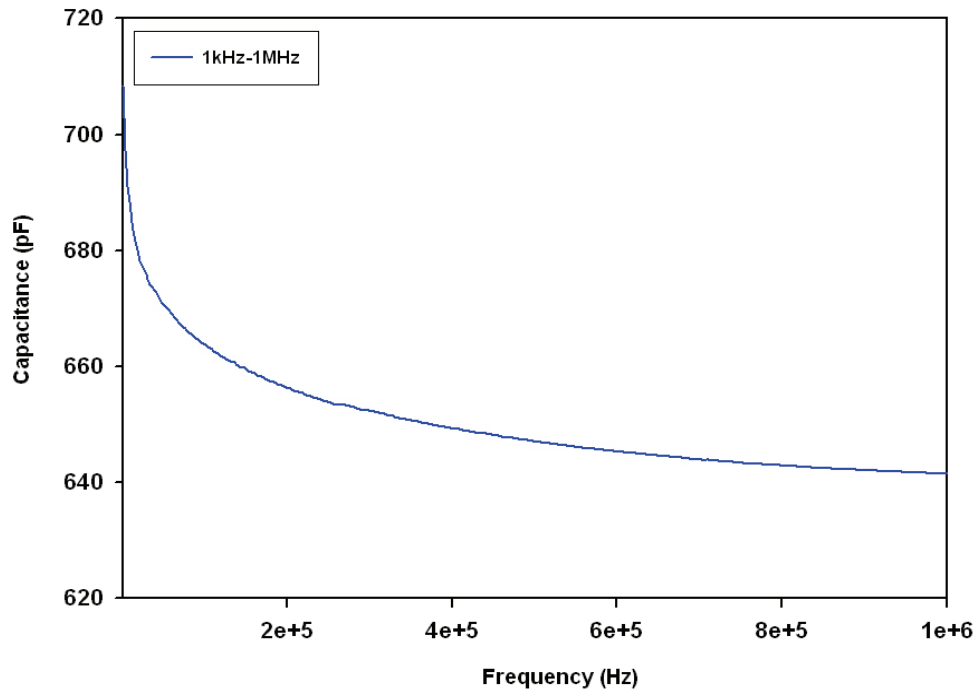


Fig. A-4. Capacitance-Frequency Curve for $\text{Pb}_{0.94}\text{La}_{0.06}(\text{Zr}_{0.65}\text{Ti}_{0.35})_{0.985}\text{O}_3$ thin film sintered at $750\text{ }^\circ\text{C}$ for 3 hours. (at 1 kHz $C=708\text{ pF}$) [51-3]

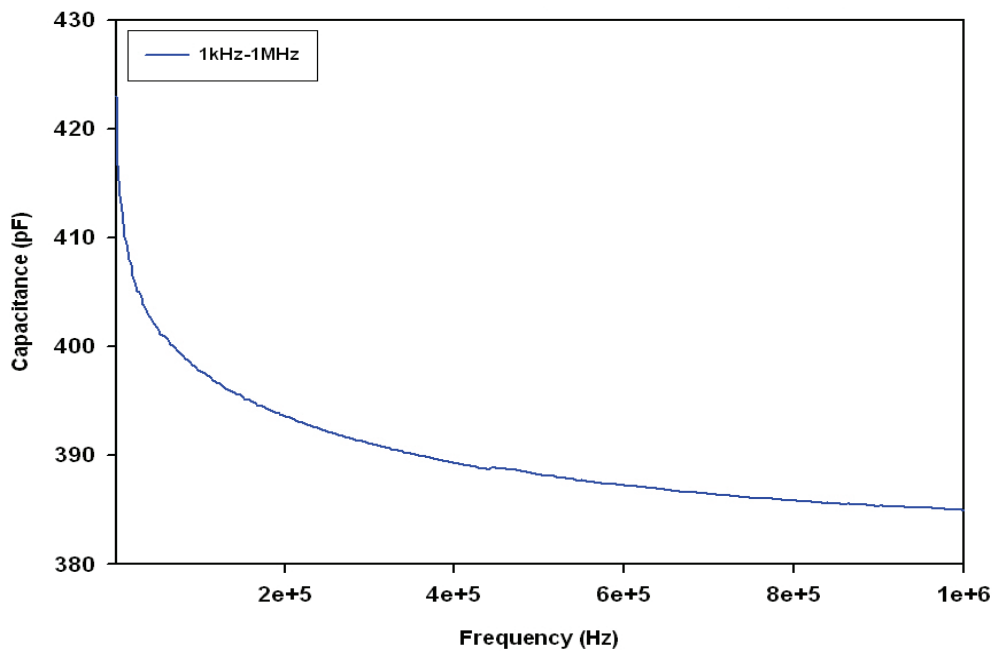


Fig. A-5. Capacitance-Frequency Curve for $\text{Pb}_{0.91}\text{La}_{0.09}(\text{Zr}_{0.65}\text{Ti}_{0.35})_{0.9775}\text{O}_3$ thin film sintered at $750\text{ }^\circ\text{C}$ for 3 hours. (at 1 kHz $C=423\text{ pF}$) [52-3]

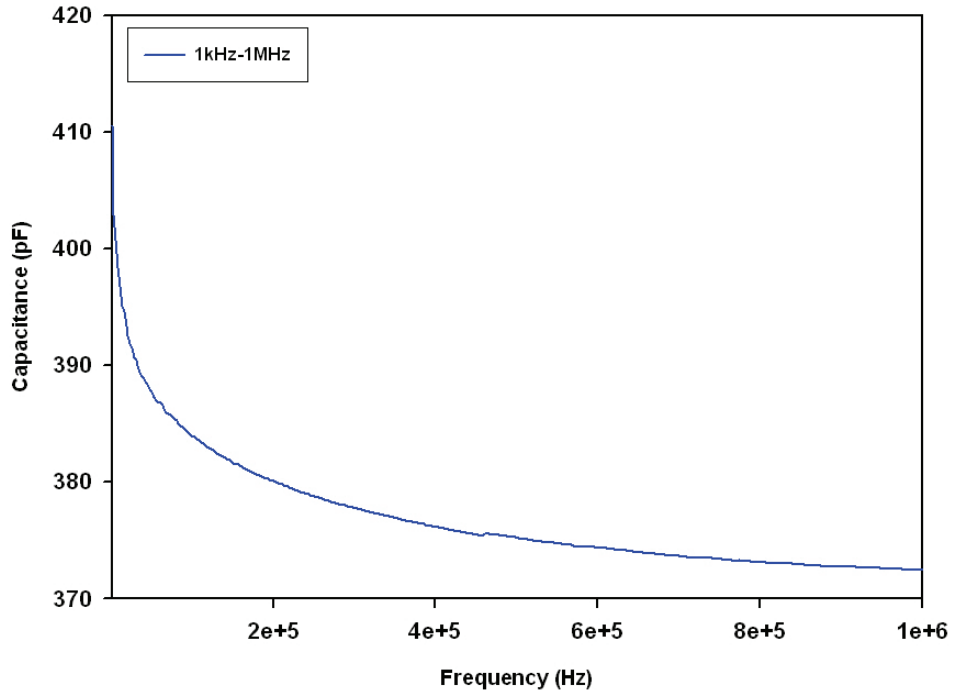


Fig. A-6. Capacitance-Frequency Curve for $\text{Pb}(\text{Zr}_{0.4}\text{Ti}_{0.6})\text{O}_3$ thin film sintered at 750°C for 3 hours. (at 1 kHz $C=411$ pF) [55-3]

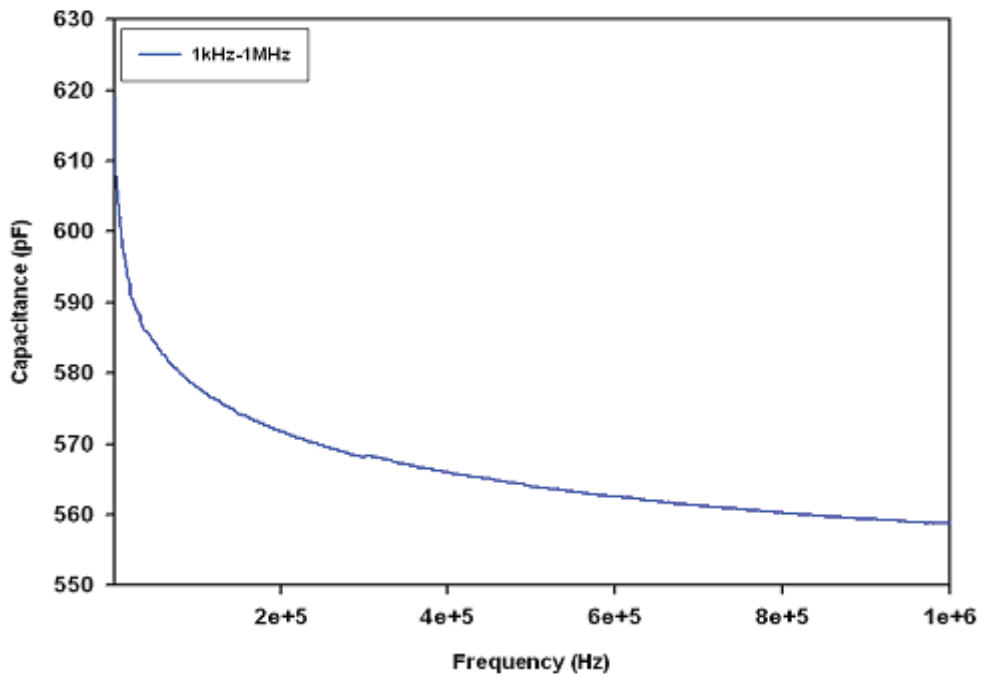


Fig. A-7. Capacitance-Frequency Curve for $\text{Pb}_{0.96}\text{La}_{0.04}(\text{Zr}_{0.4}\text{Ti}_{0.6})_{0.99}\text{O}_3$ thin film sintered at 750°C for 3 hours. (at 1 kHz $C=619$ pF) [56-3]

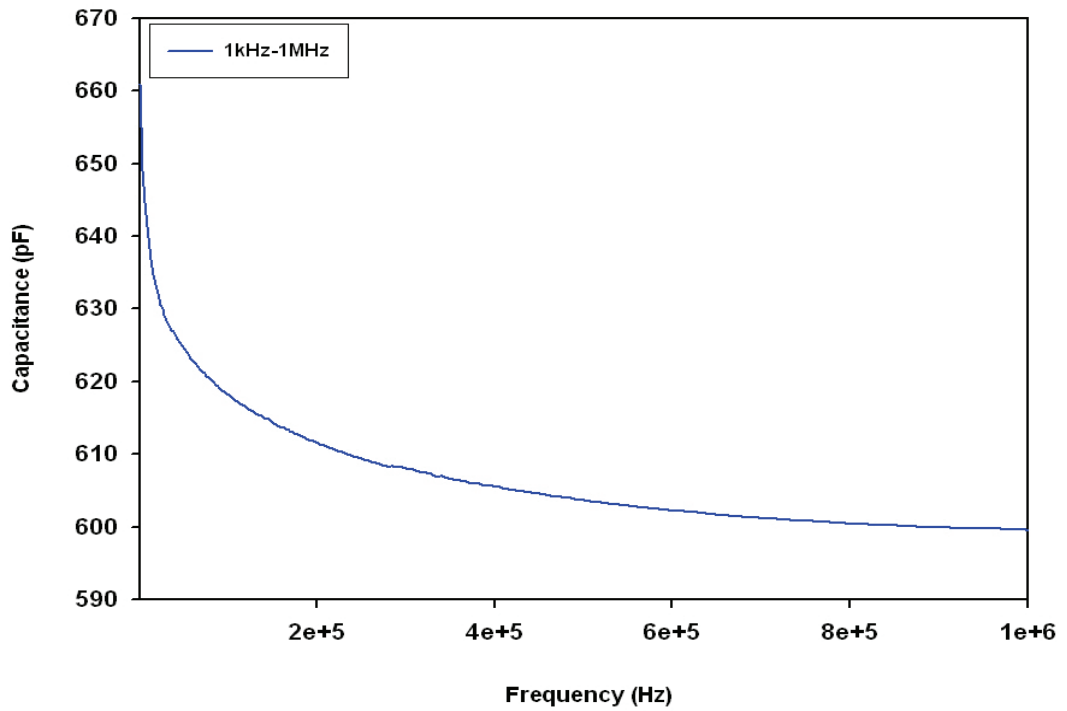


Fig. A-8. Capacitance-Frequency Curve for $\text{Pb}_{0.94}\text{La}_{0.06}(\text{Zr}_{0.4}\text{Ti}_{0.6})_{0.985}\text{O}_3$ thin film sintered at $750\text{ }^\circ\text{C}$ for 3 hours. (at 1 kHz $C=661\text{ pF}$) [57-3]

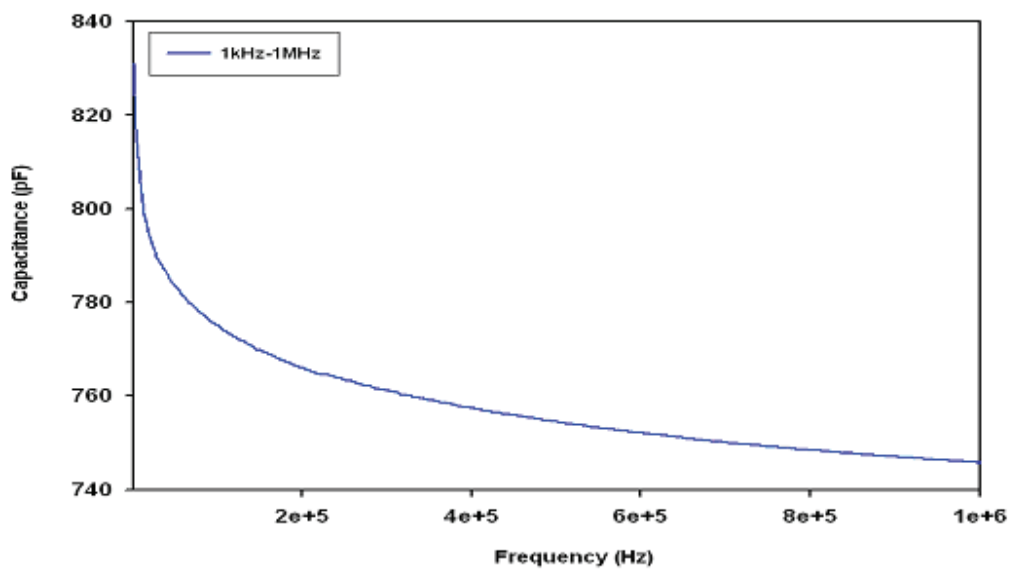


Fig. A-9. Capacitance-Frequency Curve for $\text{Pb}_{0.9}\text{La}_{0.1}(\text{Zr}_{0.4}\text{Ti}_{0.6})_{0.975}\text{O}_3$ thin film sintered at $750\text{ }^\circ\text{C}$ for 3 hours. (at 1 kHz $C=831\text{ pF}$) [58-3]

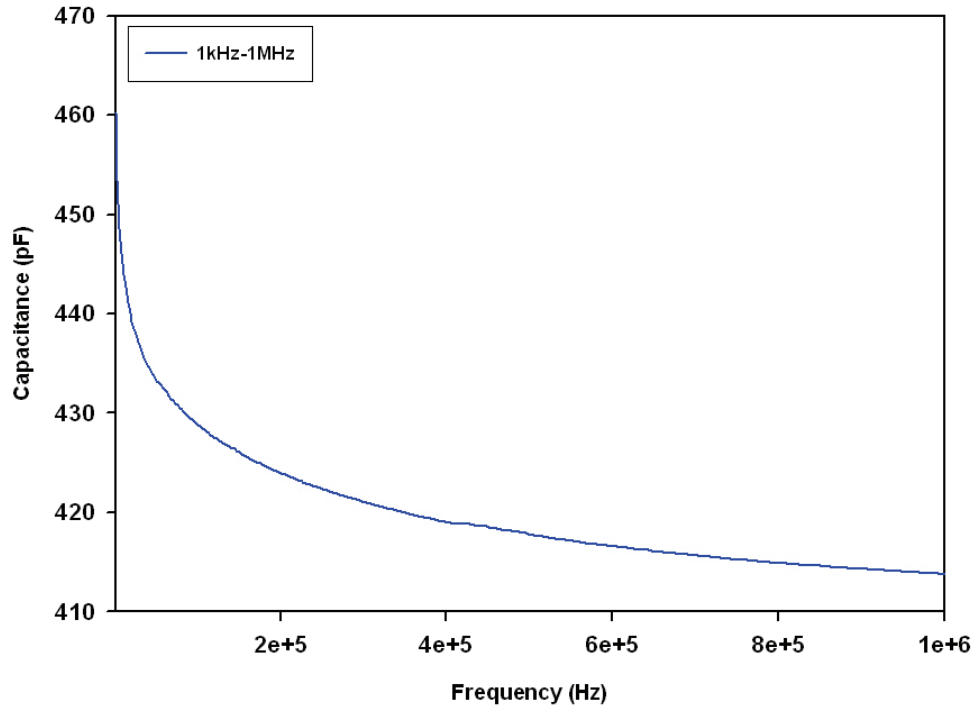


Fig. A-10. Capacitance-Frequency Curve for $\text{Pb}_{0.86}\text{La}_{0.14}(\text{Zr}_{0.4}\text{Ti}_{0.6})_{0.965}\text{O}_3$ thin film sintered at 750°C for 3 hours. (at 1 kHz $C=460$ pF) [59-3]

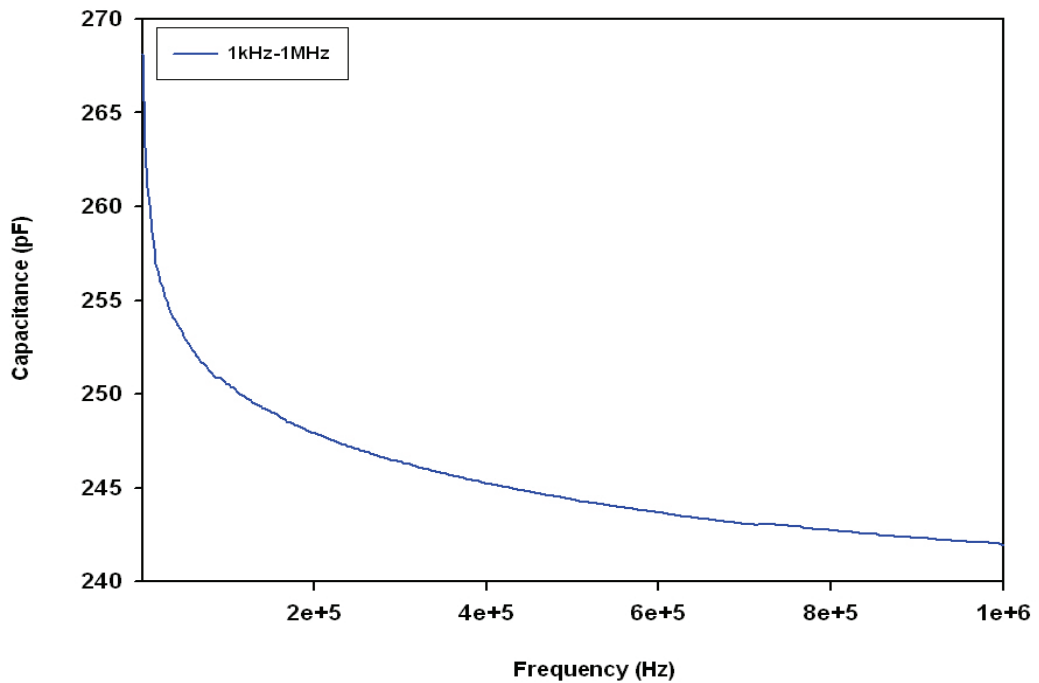


Fig. A-11. Capacitance-Frequency Curve for $\text{Pb}_{0.76}\text{La}_{0.24}(\text{Zr}_{0.4}\text{Ti}_{0.6})_{0.94}\text{O}_3$ thin film sintered at 750°C for 3 hours. (at 1 kHz $C=268$ pF) [60-3]

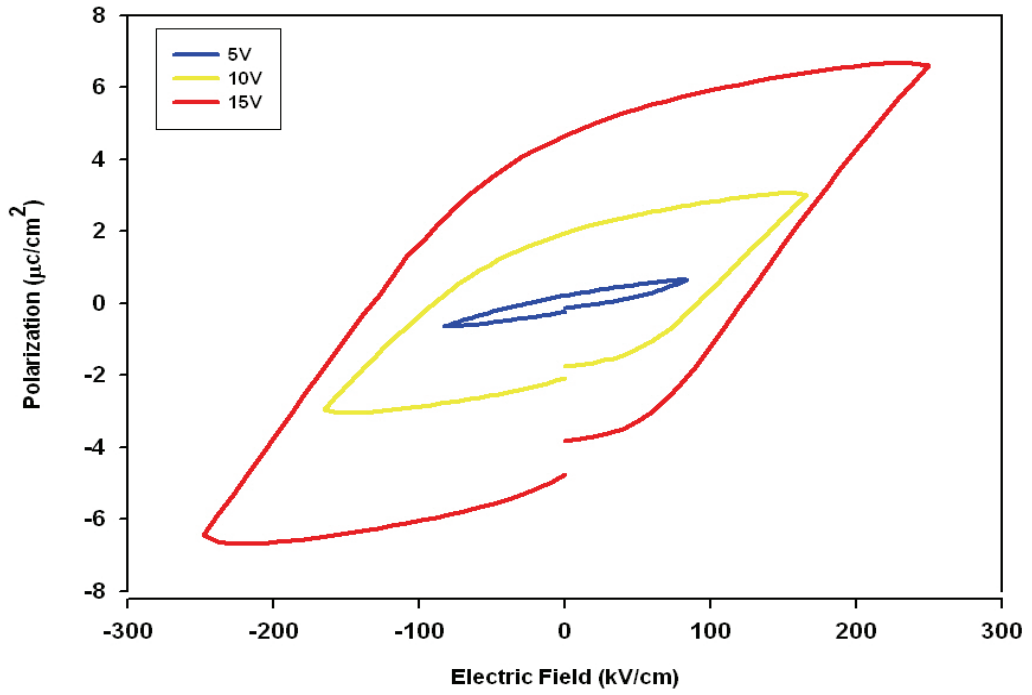


Fig. A-12. Hysteresis Curve with comp. La/Zr/Ti=4/40/60 thin film sintered at 600°C for 1 hr. [44-1]

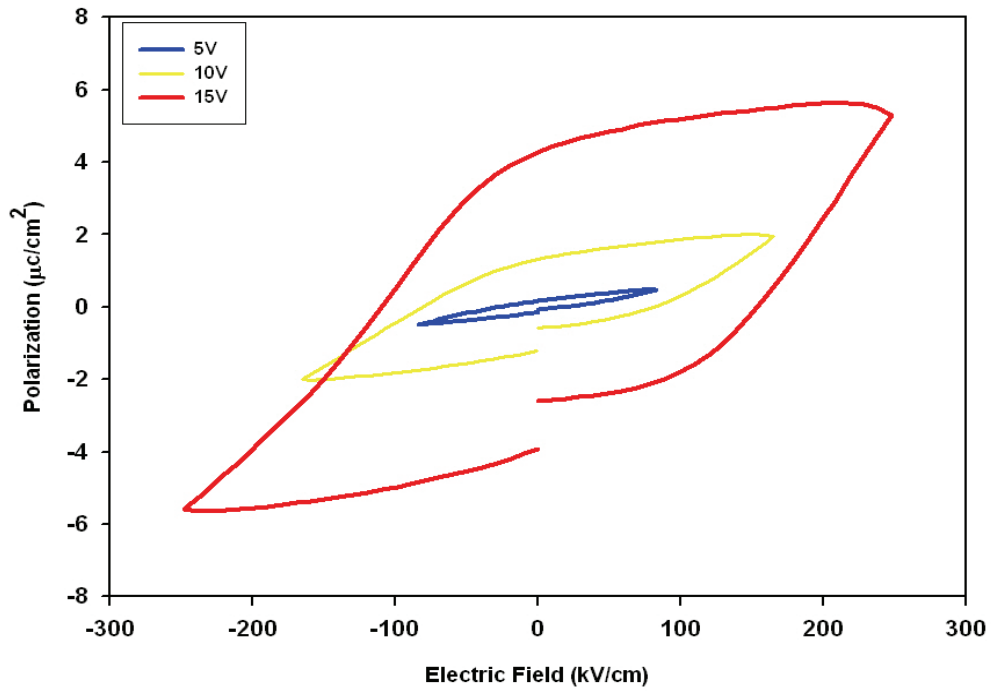


Fig. A-13. Hysteresis Curve with comp. La/Zr/Ti=4/40/60 thin film sintered at 600°C for 2 hrs. [44-2]

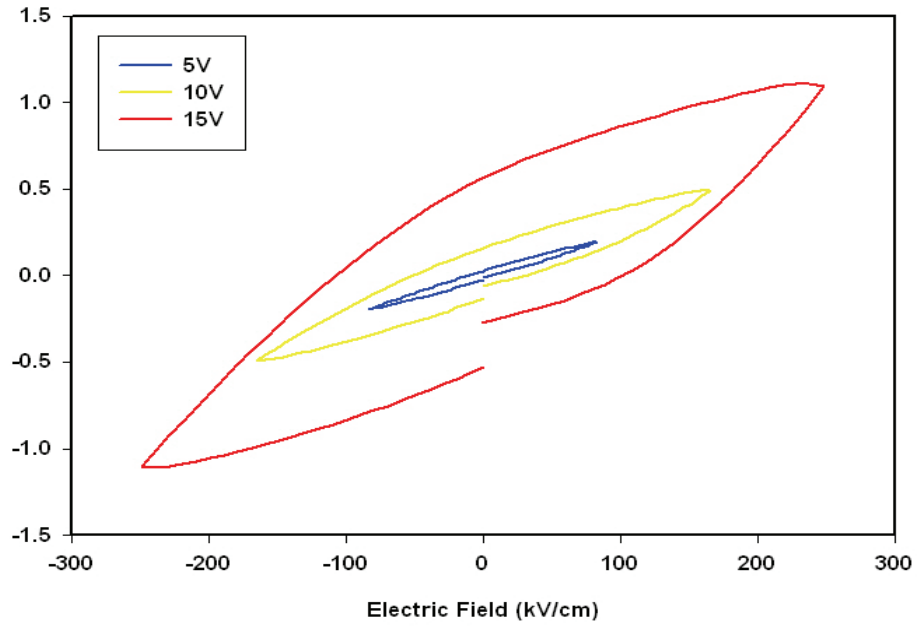


Fig. A-14. Hysteresis Curve with comp. La/Zr/Ti=4/40/60 thin film sintered at 600 °C for 3 hrs. [44-3]

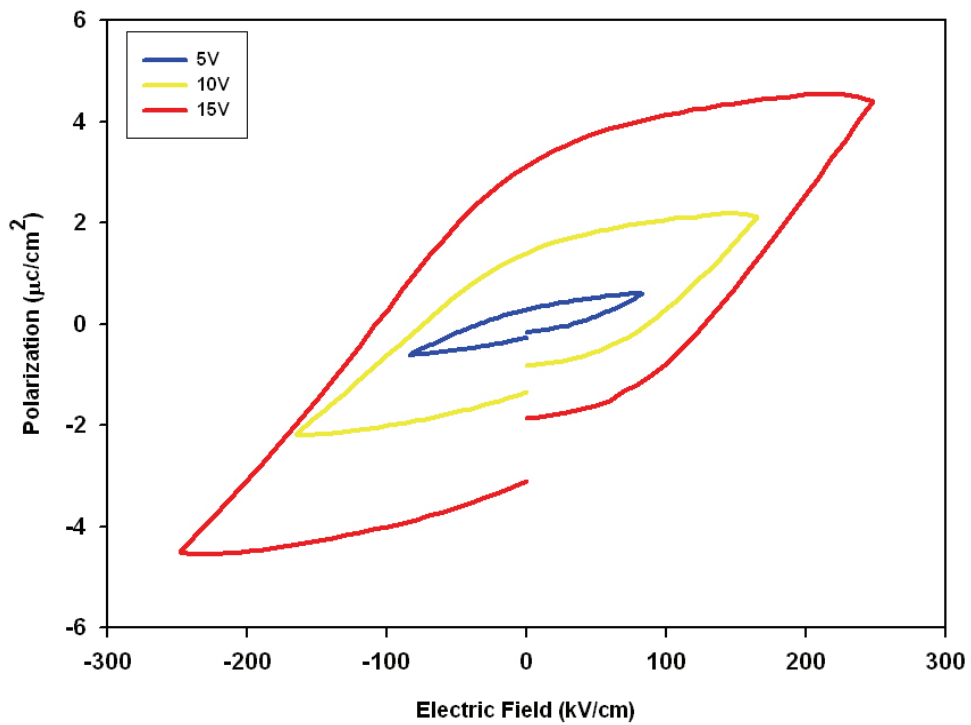


Fig. A-15. Hysteresis Curve with comp. La/Zr/Ti=4/40/60 thin film sintered at 650 °C for 1 hr. [45-1]

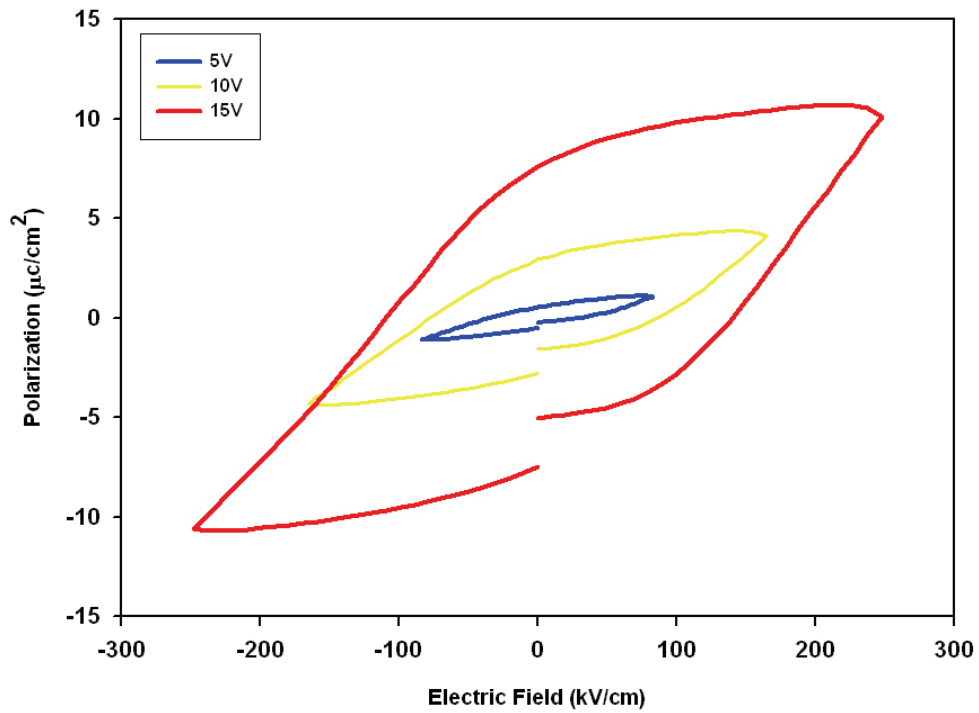


Fig. A-15. Hysteresis Curve with comp. La/Zr/Ti=4/40/60 thin film sintered at 650 °C for 2 hrs. [45-2]

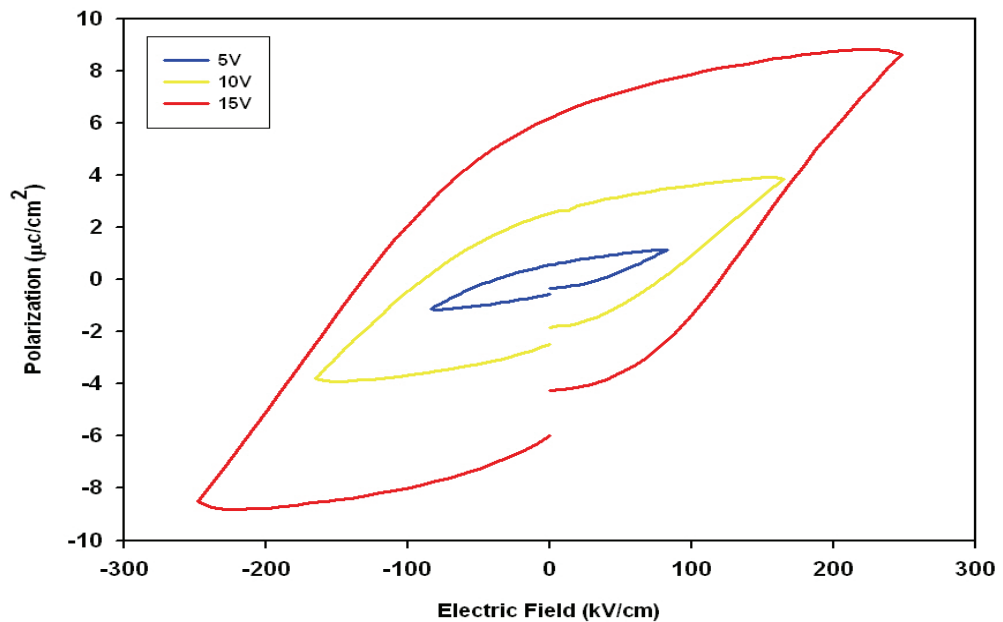


Fig. A-16. Hysteresis Curve with comp. La/Zr/Ti=4/40/60 thin film sintered at 650 °C for 3 hrs. [45-3]

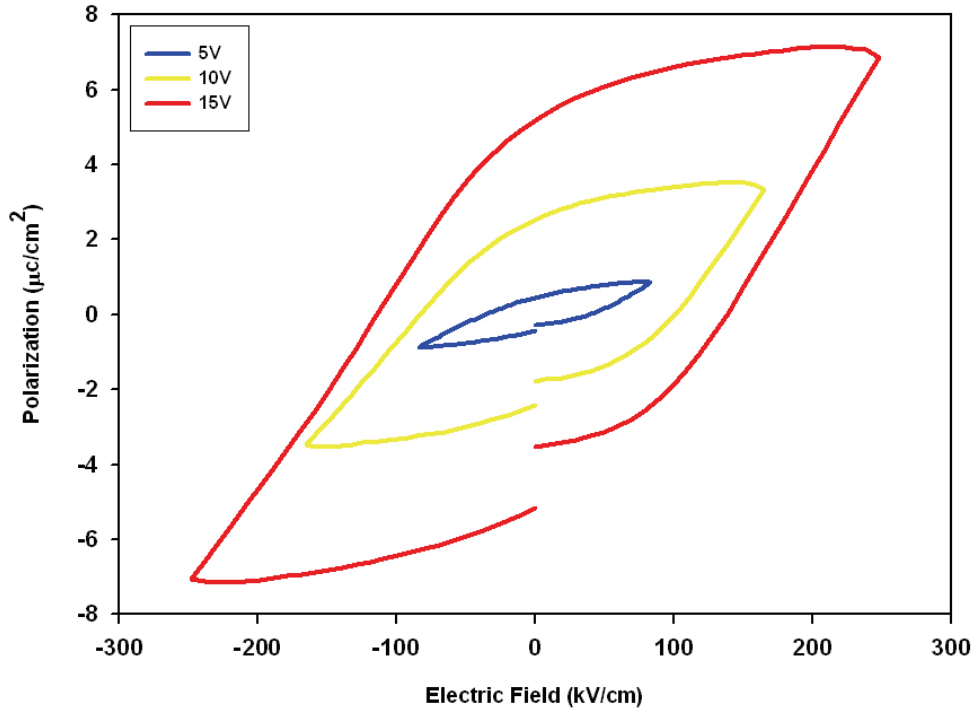


Fig. A-17. Hysteresis Curve with comp. La/Zr/Ti=4/40/60 thin film sintered at 7000 °C for 1 hr. [46-1]

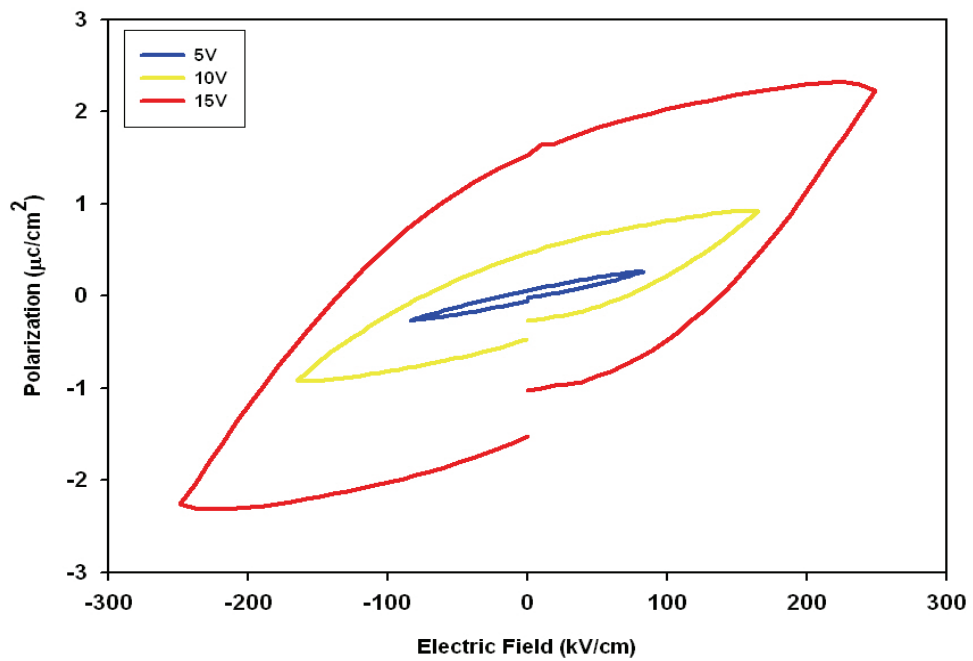


Fig. A-18. Hysteresis Curve with comp. La/Zr/Ti=4/40/60 thin film sintered at 700 °C for 2 hrs. [46-2]

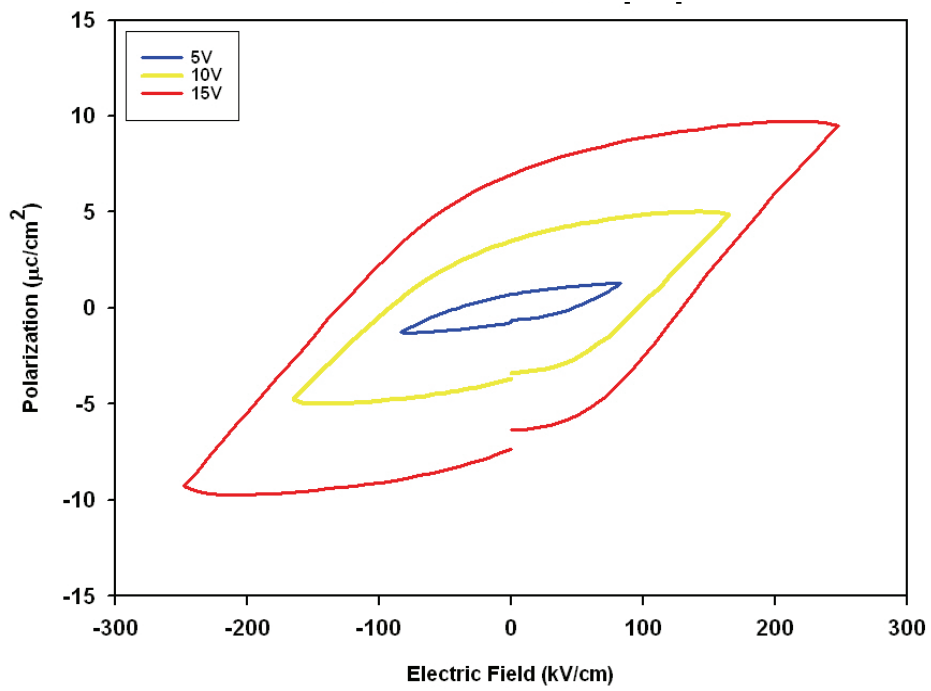


Fig. A-19. Hysteresis Curve with comp. La/Zr/Ti=4/40/60 thin film sintered at 700 °C for 3 hrs. [46-3]

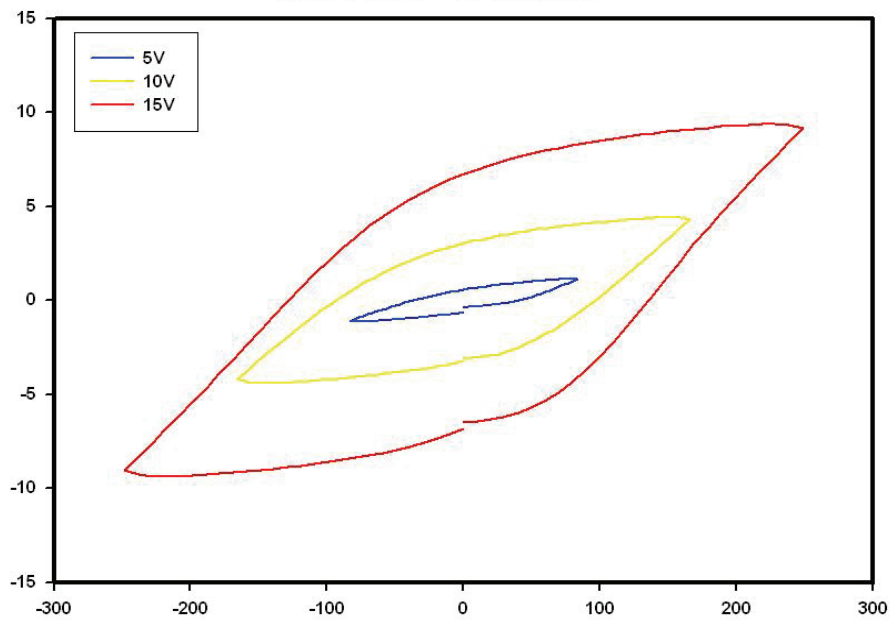


Fig. A-20. Hysteresis Curve with comp. La/Zr/Ti=4/40/60 thin film sintered at 750 °C for 3 hrs. [47-1]

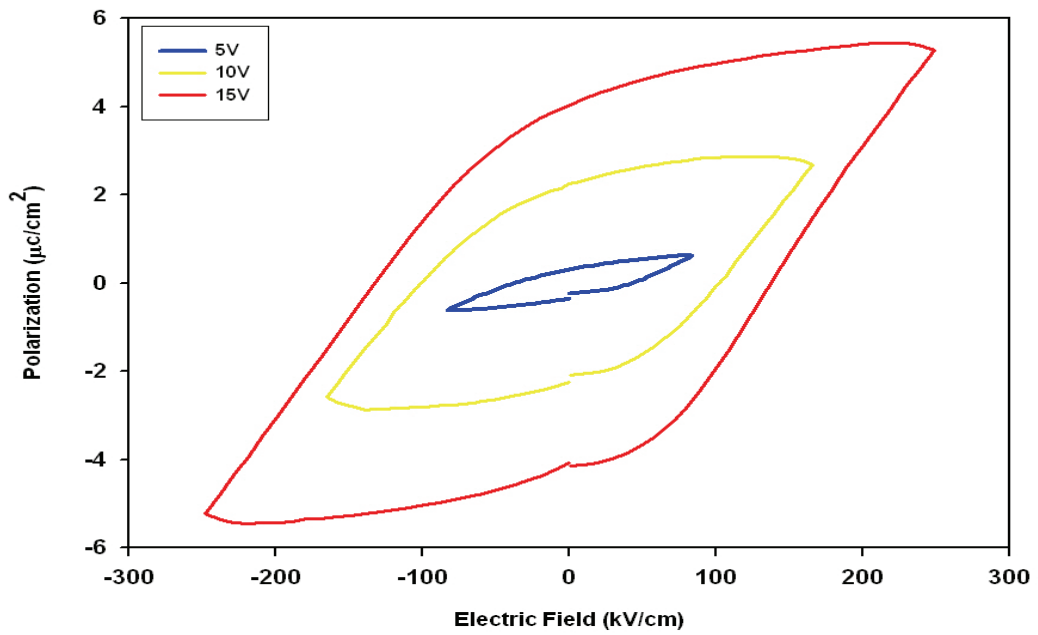


Fig. A-21. Hysteresis Curve with comp. La/Zr/Ti=4/40/60 thin film sintered at 750 °C for 2 hrs. [47-2]

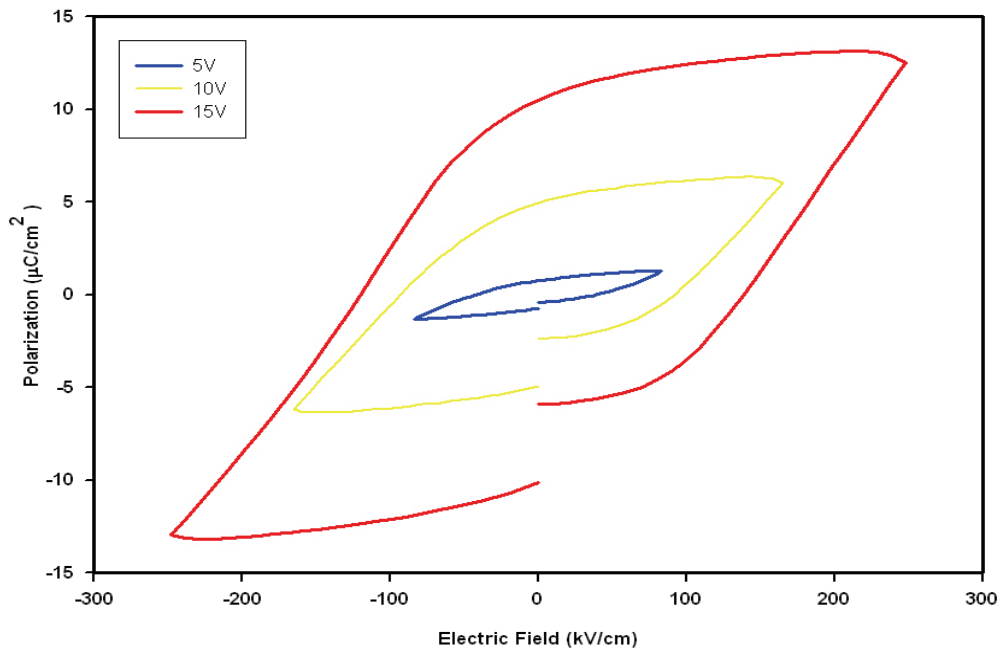


Fig. A-22. Hysteresis Curve with comp. La/Zr/Ti=4/40/60 thin film sintered at 750 °C for 3 hrs. [47-3]

